TRANSPORTATION RESEARCH
RECORD

No. 1411

Soils, Geology, and Foundations

Earthquake-Induced Ground Failure Hazards

A peer-reviewed publication of the Transportation Research Board

TRANSPORTATION RESEARCH BOARD
NATIONAL RESEARCH COUNCIL

NATIONAL ACADEMY PRESS
WASHINGTON, D.C. 1993

Transportation Research Record 1411
ISSN 0361-1981
ISBN 0-309-05558-X
Price: $24.00

Subscriber Category
IIIA soils, geology, and foundations

Printed in the United States of America

Sponsorship of Transportation Research Record 1411

GROUP 2—DESIGN AND CONSTRUCTION OF TRANSPORTATION FACILITIES
Chairman: Charles T. Edson, Greenman Pederson

Soil Mechanics Section
Chairman: Michael G. Katona, Air Force Civil Engineering Laboratory

Committee on Foundations of Bridges and Other Structures
Chairman: Joseph A. Caliendo, Utah State University
Secretary: Richard P. Long, University of Connecticut
Gregg Batchelder Adams, Roy H. Borden, Jean-Louis Briaud, Ronald G. Chassie, Murty S. Devata, Albert F. Dimillio, Victor Elias, Richard L. Engel, Roger Alain Frank, George G. Goble, Robert C. Houghton, Alan P. Kilian, John F. Ledbetter, Jr., Larry Lockett, James H. Long, Randolph W. Losch, William J. Lytle, Thom L. Neff, Gary M. Norris, Michael Wayne O'Neill, John L. Walkinshaw, Gdalyah Wiseman, James L. Withiam

Geology and Properties of Earth Materials Section
Chairman: Robert D. Holtz, University of Washington

Committee on Engineering Geology
Chairman: Jeffrey R. Keaton, Sergent Hauskins & Beckwith
James A. Amenta, Robert K. Barrett, Scott F. Burns, Jerome V. DeGraff, Herbert H. Einstein, Carlton L. Ho, Philip C. Lambe, Steve M. Lowell, Stanley M. Miller, Harry L. Moore, William L. Moore III, Stephen F. Obermeier, A. Keith Turner, Duncan C. Wyllie

G. P. Jayaprakash, Transportation Research Board staff

Sponsorship is indicated by a footnote at the end of each paper. The organizational units, officers, and members are as of December 31, 1992.

Transportation Research Record 1411

Contents

Foreword

The nine papers in this volume, the first seven of which were presented at the 1993 TRB Annual Meeting in the session on earthquake-induced ground failure hazards, focus on the status of knowledge for quantifying earthquake-induced ground failure. The first seven papers were sponsored by the Committee on Engineering Geology and the last two by the Committee on Foundations of Bridges and Other Structures. The primary hazards of strong ground shaking, surface fault rupture, and regional deformation that are created by a damaging earthquake can have significant secondary hazards, such as the collapse of buildings, landsliding, and liquefaction. Transportation systems—including highways, railroads, pipelines, airports, water ports, and bridges—are at risk of being damaged by these earthquake-induced ground failures. Research during the past two decades has resulted in a greatly improved body of knowledge concerning such hazards and how best to plan for them.

Frankel discusses efforts to better understand variations in the intensity of earthquake shaking in valleys—a phenomenon influenced by the shape of the buried bedrock surface. Jibson reports on improvements in predicting the amount of landslide displacement that could be caused by an earthquake. Kramer et al. describe a method for estimating the amount of bending in deep-pile bridge foundations in thick peat deposits caused by earthquake shaking, and Keaton focuses on the factors needed to characterize fault-rupture hazards for the design of safe buried pipelines. Improvements in quantifying damage to bridges caused by liquefaction-induced ground failure are described by Youd. Obermeier details geologic observations that provide evidence of prehistoric liquefaction-induced ground failure in the southeastern and central United States, and Martin and Pond report on the use of geotechnical engineering analyses of prehistoric liquefaction features as a method for estimating the strength of prehistoric earthquake shaking.

In the last two papers, Norris et al. discuss the Cypress Street viaduct, part of the Nimitz Freeway (Interstate 880) that was damaged during the Loma Prieta earthquake of October 17, 1989. In the first paper, subsurface conditions, site ground motions and the associated collapse, foundation types, soil properties, and porewater pressure buildup during the Loma Prieta earthquake are described. The second paper establishes the nonlinear variation in the lateral and vertical-rotational pile foundation stiffness at bents in sand and Bay mud.

Effects of Three-Dimensional Bedrock Topography on Earthquake Motions in Sedimentary Basins

ARTHUR FRANKEL

Work being done at the U.S. Geological Survey on 3-D simulations of earthquake ground motions in sedimentary basins is described. The ultimate goal of this research is to predict strong ground motions in sedimentary basins for expected large earthquakes. Throughout this paper, the inadequacy of using flat-layered models for synthesizing ground motions in sedimentary basins is emphasized. It has been demonstrated with 2-D and 3-D simulations how the slope of the alluvium-bedrock interface can trap S-waves in the basins, producing prolonged trains of surface waves. These surface waves are not generated in flat-layered models, which underestimate the duration and peak amplitude of shaking. It is necessary to account for the increased duration and amplitude of surface waves in sedimentary basins when designing man-made structures with natural periods of 1 sec and greater. Results are presented for 3-D simulations of earthquakes on the San Andreas fault in the San Bernardino and Santa Clara valleys in California. These simulations show the importance of S-wave-to-surface-wave conversions at the edges of the valleys. A contour map of maximum ground velocity in the San Bernardino Valley is produced from the simulation of a magnitude 6.5 earthquake on the San Andreas fault. Areas of especially large ground motions occur where surface waves reflected from the edges of the basin constructively interfere with trapped waves behind the direct S-wave.

The estimation of ground motions in sedimentary basins is crucial for the design of earthquake-resistant structures. It is common practice to assume a horizontal interface between the alluvium and bedrock when ground motions for alluvial sites are calculated. However, many observational and theoretical studies have demonstrated the inadequacy of using flat-layered models to predict ground motions for sites in sedimentary basins (*1–3*). Figure 1 shows schematically the wave types affecting a site in an alluvial basin. The direct S-wave will be amplified by the alluvium and is shown as the ray path that is steeply incident below the basin site. There will also be multiple reflections of the S-wave in the alluvium. In addition, the direct S-wave will convert to a trapped surface wave at the margin of the basin because of the dip of the alluvium-bedrock interface. Theoretical studies using 2-D models have demonstrated the importance of this S-wave-to-surface-wave conversion (*1*). In these theoretical studies, the converted surface wave can be the largest phase in the synthetic seismogram at periods of 1 sec and greater and, because of its slow group velocity, can vastly prolong the duration of shaking. Such converted surface waves have been observed in recordings of the 1971 San Fernando earthquake (*2*) and aftershocks of the 1989 Loma Prieta earthquake (*3*). It has been suggested that the prolonged, damaging ground motions in Mexico City from the 1985 Michoacan earthquake were composed of such surface waves (*4*).

Obviously, the presence of these large surface waves has profound implications on the design of structures with natural periods of 1 sec and longer. Models with horizontal layering do not predict these S-wave-to-surface-wave conversions, which can be much larger than the amplitude of the surface waves generated at the source.

Some observational studies have demonstrated that these surface waves can be reflected along various edges of an alluvial basin, highlighting the need for 3-D simulations to predict ground motions accurately. For example, observations of Loma Prieta aftershocks using a dense array in Sunnyvale showed that much of the longer-period ($f \leq 1$ Hz) energy after the S-wave is composed of surface waves, some of which come from azimuths very different from the source (*3*). Surface waves scattered from specific locations near the edges of alluvial basins were reported by Phillips et al. (*5*) and Spudich and Iida (*6*) for the Kanto Basin in Japan and the Coachella Valley in California, respectively.

This paper documents the results from 3-D numerical simulations of ground motions in the San Bernardino and Santa Clara valleys in southern and northern California, respectively, during earthquakes on the San Andreas fault. Each of these areas is a major population center containing many large structures that are vulnerable to seismic shaking at periods of 1 sec and larger. Thus, understanding the propagation of surface waves in these valleys is critical to designing earthquake-resistant structures.

METHOD

The finite-difference method was used to propagate the complete elastic wavefield through 3-D models of sedimentary basins. The wavefield includes P, SH, and SV waves, converted phases, surface waves, multiple reflections, diffractions, and head waves. The method has been described in more detail by Frankel and Vidale (*7*). Let u, v, and w be the displacements in the x, y, and z directions, respectively. denotes density and and are the Lamé constants. These medium properties vary with position. The three coupled wave

U.S. Geological Survey, 922 National Center, Reston, VA 22092.

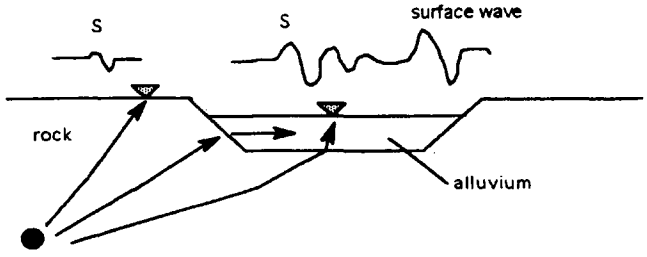

FIGURE 1 Schematic vertical cross section of ray paths between the hypocenter (*solid circle*) and sites on rock and in an alluvial basin (*inverted triangles*). Idealized seismograms for the rock and alluvial sites are shown above each receiver. The surface wave at the alluvial site is produced by conversion of the S-wave at the left edge of the basin.

equations are

$$\rho u_{tt} = [(\lambda + 2\mu)u_x + \lambda w_z + \lambda v_y]_x + (\mu u_y + \mu v_x)_y + (\mu u_z + \mu w_x)_z$$

$$\rho v_{tt} = [(\lambda + 2\mu)v_y + \lambda w_z + \lambda u_x]_y + (\mu v_x + \mu u_y)_x + (\mu v_z + \mu w_y)_z$$

$$\rho w_{tt} = [(\lambda + 2\mu)w_z + \lambda u_x + \lambda v_y]_z + (\mu w_x + \mu u_z)_x + (\mu w_y + \mu v_z)_y \quad (1)$$

Here subscripts denote partial derivatives. The model of the sedimentary basin can be arbitrarily complicated.

In the simulations described below, a grid spacing of 100 m was used. Given this grid spacing and the slowest S-wave velocity in the grid (0.6 km/sec), the simulations are accurate up to 1 Hz. Each grid contained about 4 million grid points.

The simulations described here were performed on a Cray YMP supercomputer. A run of 5,000 time steps takes about 8 CPU-hr on the Cray. Since each time step corresponds to 0.012 sec, such a run simulates 60 sec of ground motion. Videotapes have been made of the simulations described in this paper.

SAN BERNARDINO VALLEY SIMULATIONS

Figure 2 shows the area of the simulations for the San Bernardino Valley in southern California. These simulations are described in more detail by Frankel (*8*). The 3-D grid corresponds to 37 by 16 by 7 km in depth. The basin model was derived from the limited water well and oilwell data available, as well as one refraction line. For the alluvium, the shear wave velocity used was 0.6 km/sec; the P-wave velocity, 1.1 km/sec; and the density, 2.0 g/cc. For the rock just below the alluvium, the shear wave velocity used was 2.0 km/sec; the P-wave velocity, 3.5 km/sec; and the density, 2.6 g/cc. Below 3 km depth, V_P increased to 5.0 km/sec and V_S increased to 2.9 km/sec. Two hypothetical earthquakes along the San Andreas fault were considered: a moment-magnitude (M) 5 (point source, 6 km depth) and an M6.5 earthquake that ruptured a 30-km-long segment of the fault (Figure 3). The M6.5 earthquake ruptured from northwest to southeast along the fault at a rupture velocity of $0.8V_S$, with slip occurring over a depth range of 3.5 to 6.5 km. For both events, the slip velocity at any point on the fault was a truncated Gaussian pulse with a width of 1.0 sec. Both earthquakes were pure strike slip on vertical fault. A filtered random number field was used to represent slip on the fault. The realization used here had large areas of slip (asperities) near both ends of the fault.

The difference between synthetics from the 3-D simulation and those from a flat-layered (1-D) model is dramatic (Figure 4, for M5). The 3-D simulation has a much longer duration of shaking than the 1-D model. The basic reason for this is

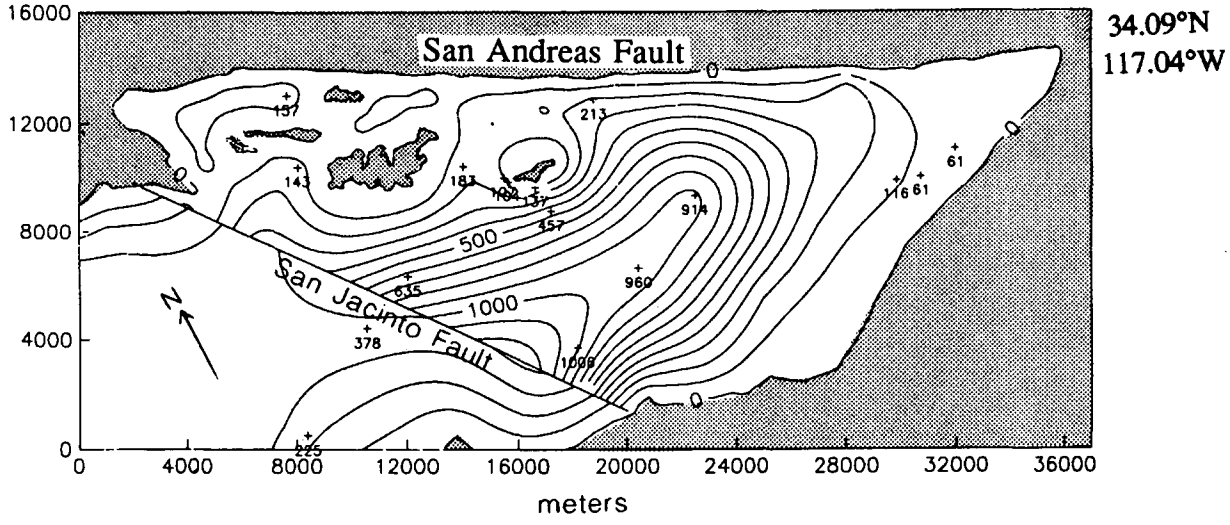

FIGURE 2 Map of San Bernardino Valley with outcrops of bedrock shaded. Crosses indicate depth to basement (in meters) from wells and from one refraction line; 635-m value is conjecture. Contours show depth to basement (in meters) used in simulation (100-m contour interval). Grid size was 370 by 160 by 70 (depth), with a grid spacing of 100 m.

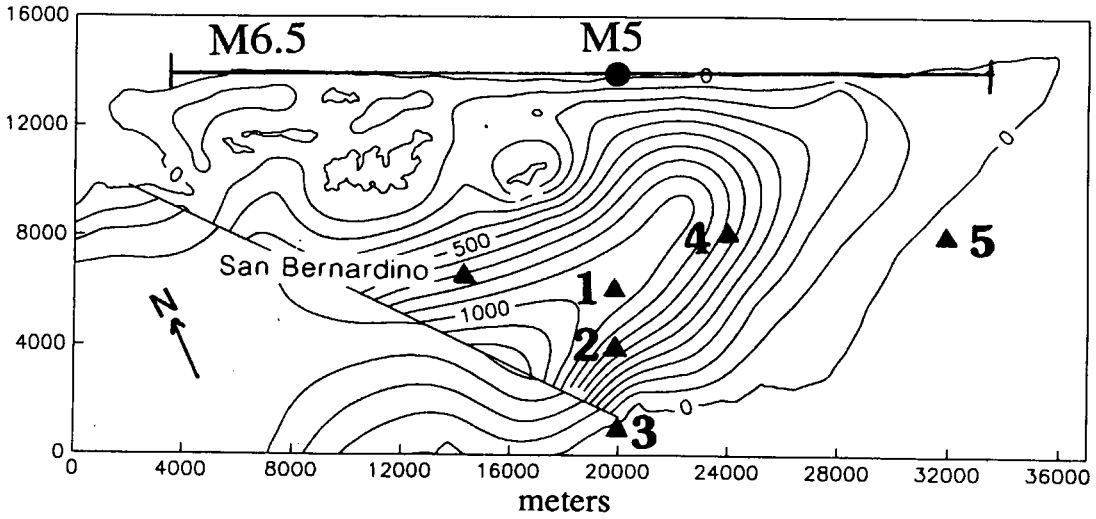

FIGURE 3 Location of moment magnitude M5 (*circle*) and M6.5 earthquakes along the San Andreas fault that were used in the simulations. The earthquakes were specified using their equivalent double couples in the grid. Triangles show receivers with displayed synthetics. Contour interval is 100 m.

the trapping of body waves in the alluvium that occurs in the 3-D simulation. The incident S-wave is essentially converted into surface waves (Rayleigh and Love) at the margins of the basin. These surface waves have relatively slow group velocities and prolong the duration of shaking in the basin. Models using flat layers cannot account for these body-wave-to-surface-wave conversions. The 2-D simulation shows some of the surface waves but considerably underestimates the duration of shaking compared with the 3-D simulation. The 3-D simulation contains substantial surface wave energy coming from azimuths different from the source direction, energy not modeled by the 2-D simulation.

Figure 5 contains the ground velocity from the 3-D simulation for the San Bernardino site for the M6.5 earthquake. The 3-D simulations do not include anelastic attenuation, which is incorporated into the sediments by convolving the synthetics with a time-varying Q-operator. The bottom seismograms in Figure 5 show the result for a shear wave Q of

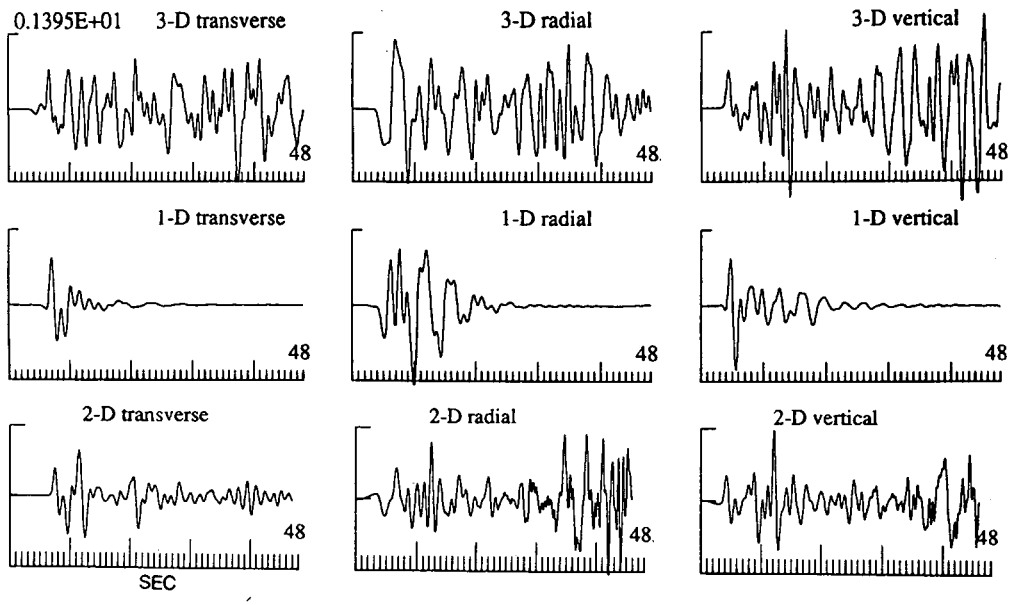

FIGURE 4 *Top:* Velocity synthetics from 3-D simulation of M5 event for San Bernardino site. *Middle:* Reflectivity synthetics for same site using flat-layered model. *Bottom:* Synthetics from 2-D finite-difference simulation (vertical cross section). Note large duration of synthetics from 3-D model compared with those from 1-D model. All synthetics are plotted with same scale. Peak amplitude is given in centimeters per second; time scale is marked in seconds.

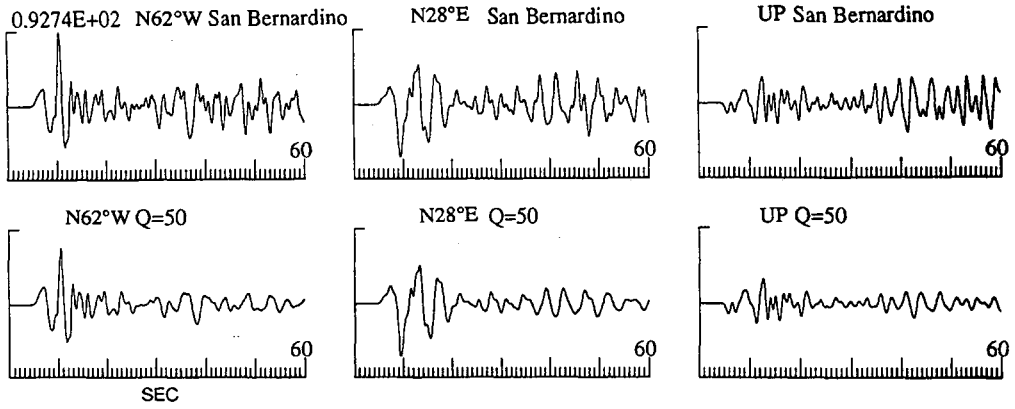

FIGURE 5 Velocity synthetics at San Bernardino from 3-D simulation of M6.5 earthquake *(top)* with no anelastic attenuation and *(bottom)* using Q of 50 in alluvium. Peak amplitude is given in centimeters per second. Synthetics are plotted with the same scale. Seismograms are for horizontal motion parallel to the fault strike *(left,* N62°W), horizontal motion perpendicular to the fault strike *(middle,* N28°E), and vertical motion *(right).*

50 in the sediments. High-frequency energy is significantly reduced in the later part of the synthetics. The substantial differences between shaking at basin and rock sites are shown in Figures 6 and 7, which give the synthetic seismograms at nearby rock and alluvium sites. Peak-to-peak amplitudes are three to seven times larger for the basin sites than the rock sites in these examples. The duration of shaking is much longer for the basin sites than the rock sites, primarily because of trapped waves in the sediment. The top set of seismograms in Figure 7 shows the largest peak velocities found in the simulation (Site 4). These large velocities are caused by a number of factors: directivity of the source, constructive interference from rupture events at different parts of the fault, and constructive interference of trapped waves generated along the near and far edges of the basin. Figure 8 is a contour plot of the maximum horizontal velocities from the 3-D simulation. In general, basin sites exhibit much larger peak velocities than the rock sites. The largest velocities occur near the deepest part of the basin. The location of the largest ground motions is dependent on the rupture direction, asperity positions, and radiation pattern of the earthquake.

SANTA CLARA VALLEY SIMULATION

Ground motions were also simulated for an M_L 4.4 aftershock of the Loma Prieta earthquake. This aftershock was recorded by a dense array of four seismometers at Sunnyvale in the Santa Clara Valley (Figure 9). The 3-D simulation covered the area of the Santa Clara Valley shown in Figure 10 (30 by 22 by 6 km in depth, 100-m grid spacing). The alluvium and rock properties used in this simulation were the same as those in the San Bernardino simulation but did not include the higher velocities below 3 km. The results of the Santa Clara Valley simulation have been discussed in detail by Frankel and Vidale (*7*).

Synthetic seismograms along a north-south profile are shown in Figure 11. Note the large difference in amplitude and du-

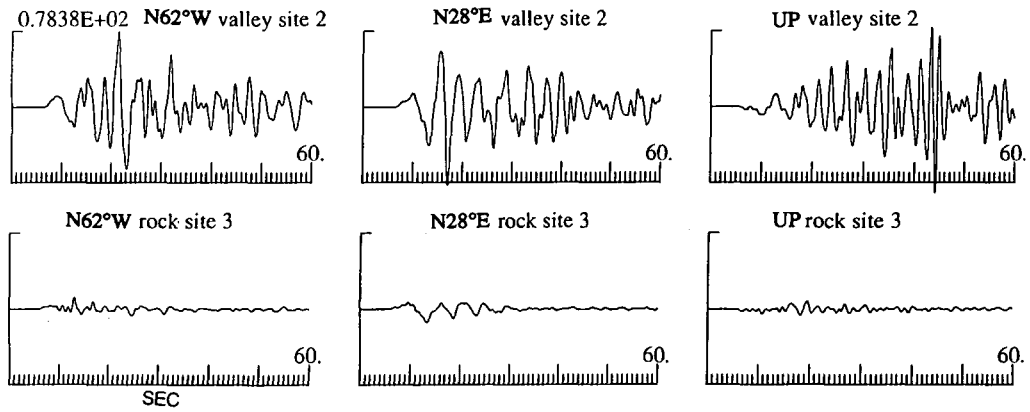

FIGURE 6 Velocity synthetics at Sites 2 and 3 from 3-D simulation of M6.5 event (no anelastic attenuation). Note large amplitude difference between valley and rock sites. Synthetics plotted with the same scale.

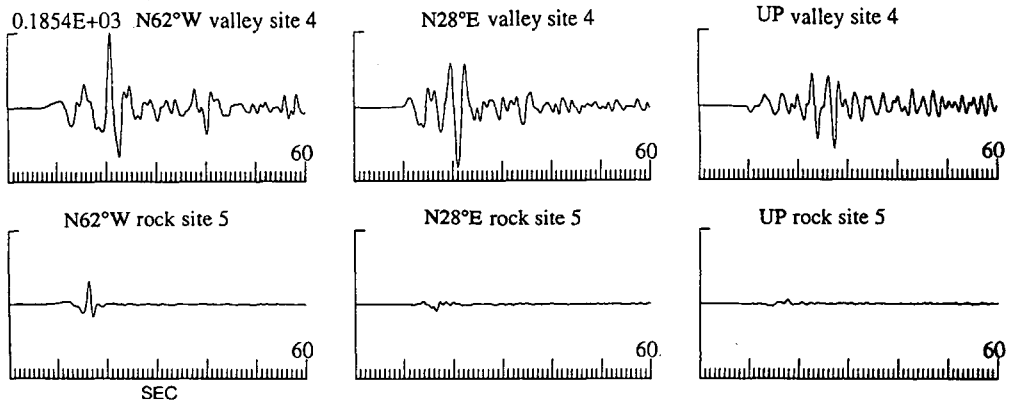

FIGURE 7 Velocity synthetics at Sites 4 and 5 from 3-D simulation of M6.5 event (no anelastic attenuation). Site 4 has the largest horizontal ground motions in the simulation for this event. All synthetics are plotted with same scale. Peak amplitude is given in centimeters per second.

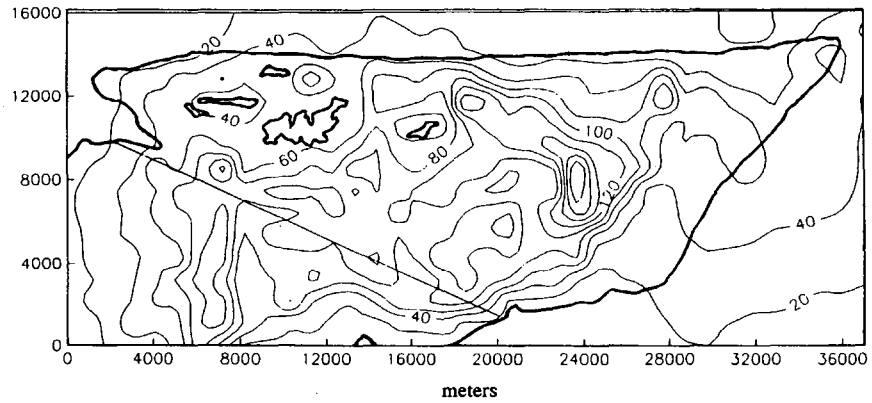

FIGURE 8 Contour plot of peak horizontal motions from synthetics from 3-D simulations of M6.5 earthquake (southeast-propagating rupture). Values are from vector sum of both horizontal components and are given in centimeters per second (20-cm/sec contour interval). Peak motions are generally larger in the valley than in the surrounding rock. Largest motions are about 185 cm/sec. Thick lines denote edges of bedrock outcrops.

ration between the rock site (Site 1) and the valley sites (Sites 2 to 4). Love and Rayleigh waves are the largest phases in the synthetics for the basin sites. These surface waves are produced by conversion of the incident S-waves at the southern margin of the valley. Figure 12 compares the synthetic displacements (bottom row) with the observed motions for this aftershock recorded at Sunnyvale (top row). The agreement between the synthetics and data is good for the radial component. However, the Love waves on the transverse synthetic arrive earlier than the Love waves in the data. This may be due to overestimating velocities of the alluvium or underestimating the alluvium thickness. It is noteworthy that 1-D models would not even predict these large Love waves.

SUMMARY

The 3-D simulations demonstrate the importance of S-wave-to-surface-wave conversions at the edges of the alluvial basin. These surface waves often include the largest arrivals in the synthetic seismograms and greatly prolong the duration of shaking in the basin. The surface waves are reflected from the edges of the basin and travel in different directions across the valley. Large motions occur where the reflected waves constructively interfere with trapped waves behind the direct S-wave.

FUTURE EFFORTS

The 3-D simulations represent a promising tool for predicting ground motions in sedimentary basins for frequencies ≤ 1 Hz. These efforts are largely limited by the lack of detailed knowledge of the velocity structure of sedimentary basins. For the two basins described above, the depth to bedrock is not known in most parts of the basins. The velocity and Q in the alluvium are poorly known. Refraction and reflection studies are needed to improve these models of the basin. The computational

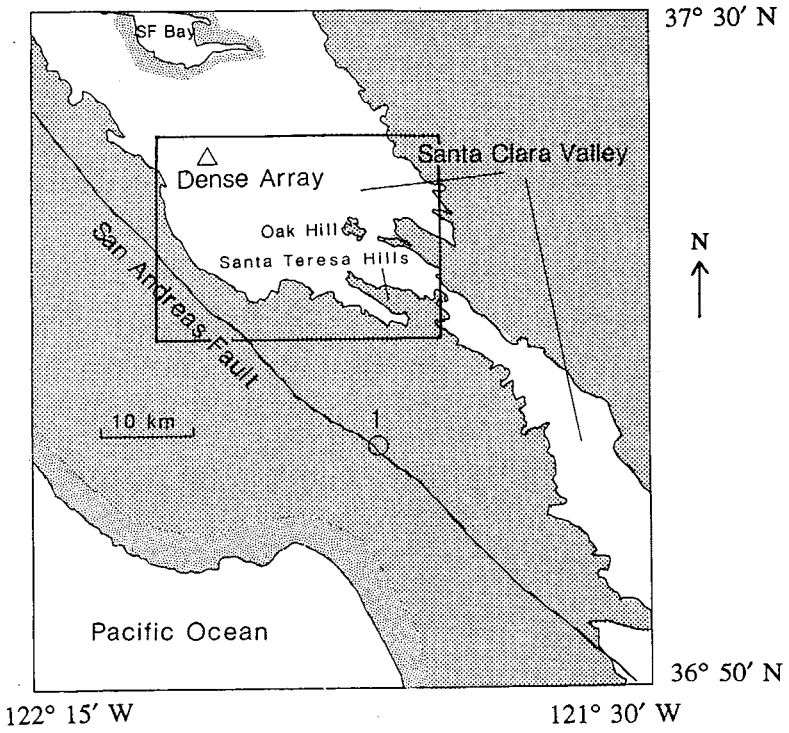

FIGURE 9 Map of area south of San Francisco Bay. Box denotes area for Santa Clara Valley simulation. *1* is epicenter of M_L 4.4 Loma Prieta aftershock (Oct. 25, 1989) that was modeled. Shaded areas are bedrock.

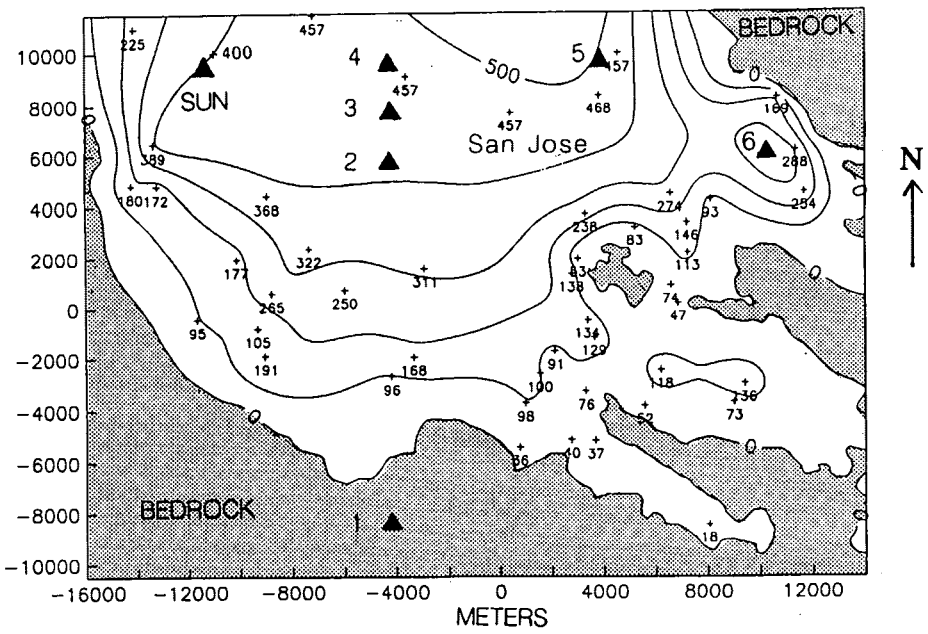

FIGURE 10 Map of area used in Santa Clara Valley simulation. Crosses indicate depths to bedrock from water wells (in meters). Depths for crosses in center of valley are educated guesses, since water wells do not reach bedrock there. Contours show depth to bedrock for model used in simulation (100-m contour interval). The following values were used: V_S of 0.6 km/sec for alluvium, 2.0 km/sec for bedrock; V_P of 1.1 km/sec for alluvium, 3.5 km/sec for bedrock; ρ of 2.0 gm/cc for alluvium, 2.6 gm/cc for bedrock. Triangles show locations of receivers for synthetic seismograms. *SUN* denotes location of Sunnyvale dense array that recorded this Loma Prieta aftershock.

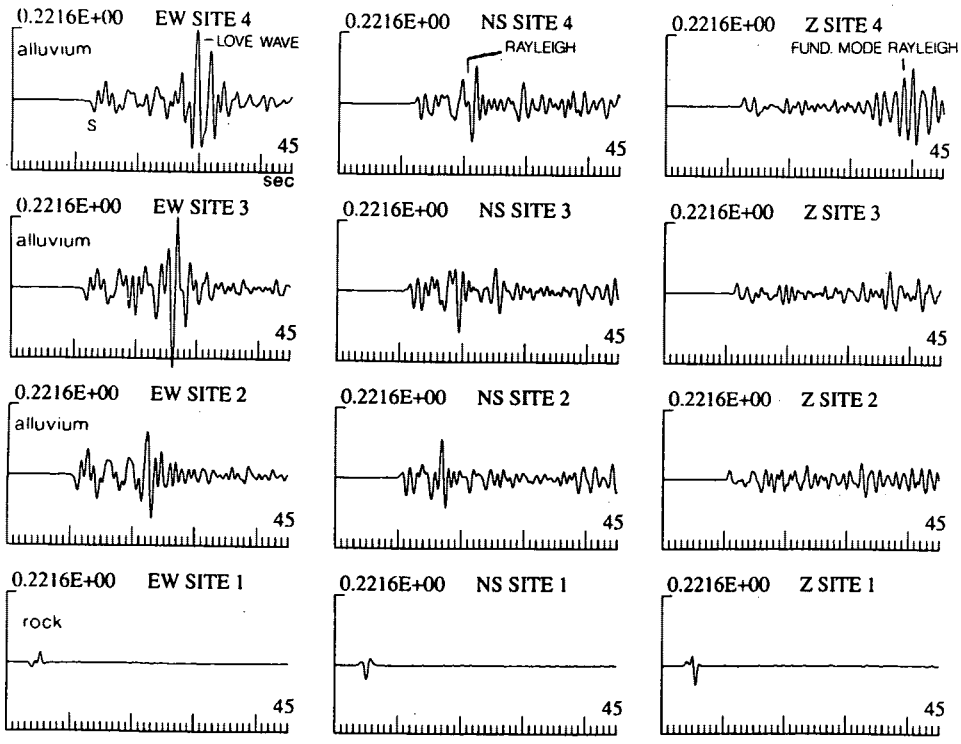

FIGURE 11 Synthetic velocity seismograms from 3-D simulation for Santa Clara Valley (east-west, north-south, and vertical components). Peak velocities are shown above each panel in centimeters per second.

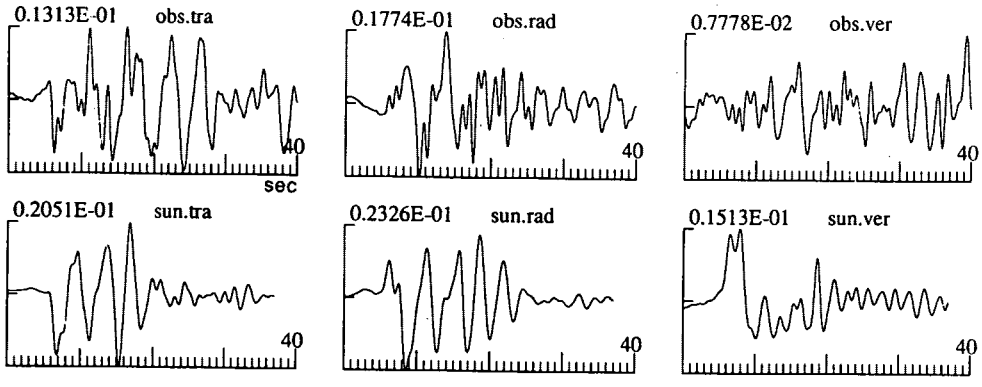

FIGURE 12 Observed (*top*) and synthetic (*bottom*) ground displacements for the Sunnyvale dense array site. Transverse, radial, and vertical motions are shown. Peak amplitudes are given in centimeters. The synthetics were convolved with a time-varying Q-operator corresponding to a shear wave Q of 50 in the sediments.

techniques are now available to incorporate these details into the simulations, which require large amounts of supercomputer time. However, the 3-D calculations can also be done on fast workstations and are particularly suited to parallel processors. Accurate prediction of ground motions also requires consideration of a range of rupture scenarios, with varying rupture directivity and slip distribution.

REFERENCES

1. Bard, P. Y., and M. Bouchon. The Seismic Response of Sediment-Filled Valleys. Part 1. The Case of Incident SH-waves. *Bulletin of the Seismological Society of America,* Vol. 70, 1980, pp. 1263–1286.
2. Vidale, J. E., and D. V. Helmberger. Elastic Finite-Difference Modeling of the 1971 San Fernando, California Earthquake. *Bul-*

letin of the Seismological Society of America, Vol. 78, 1988, pp. 122–141.
3. Frankel, A., S. Hough, P. Friberg, and R. Busby. Observations of Loma Prieta Aftershocks from a Dense Array in Sunnyvale, California. *Bulletin of the Seismological Society of America,* Vol. 81, 1991, pp. 1900–1922.
4. Kawase, H., and K. Aki. A Study on the Response of a Soft Basin for Incident S, P, and Rayleigh Waves with Special Reference to the Long Duration Observed in Mexico City. *Bulletin of the Seismological Society of America,* Vol. 79, 1989, pp. 1361–1382.
5. Phillips, W. S., S. Kinoshita, and H. Fujiwara. Basin-Induced Love Waves Observed Using the Strong Motion Array at Fuchu, Japan. *Bulletin of the Seismological Society of America,* Vol. 83, 1993, pp. 65–84.
6. Spudich, P., and M. Iida. The Seismic Coda, Site Effects, and Scattering in Alluvial Basins Studied Using Aftershocks of the 1986 North Palm Springs, California Earthquake as Source Arrays. *Bulletin of the Seismological Society of America,* Vol. 83, 1993, in press.
7. Frankel, A., and J. Vidale. Three-Dimensional Simulations of Seismic Waves in the Santa Clara Valley, California, from a Loma Prieta Aftershock. *Bulletin of the Seismological Society of America,* Vol. 82, 1992, pp. 2045–2074.
8. Frankel, A. Three-Dimensional Simulations of Ground Motions in the San Bernardino Valley, California, for Hypothetical Earthquakes on the San Andreas Fault. *Bulletin of the Seismological Society of America,* Vol. 83, 1993, in press.

Any use of a product name in this paper is for descriptive purposes only and does not constitute endorsement by the U.S. government.

Publication of this paper sponsored by Committee on Engineering Geology.

Predicting Earthquake-Induced Landslide Displacements Using Newmark's Sliding Block Analysis

RANDALL W. JIBSON

A principal cause of earthquake damage is landsliding, and the ability to predict earthquake-triggered landslide displacements is important for many types of seismic-hazard analysis and for the design of engineered slopes. Newmark's method for modeling a landslide as a rigid-plastic block sliding on an inclined plane provides a workable means of predicting approximate landslide displacements; this method yields much more useful information than pseudostatic analysis and is far more practical than finite-element modeling. Applying Newmark's method requires knowing the yield or critical acceleration of the landslide (above which permanent displacement occurs), which can be determined from the static factor of safety and from the landslide geometry. Earthquake acceleration-time histories can be selected to represent the shaking conditions of interest, and those parts of the record that lie above the critical acceleration are double integrated to determine the permanent landslide displacement. For approximate results, a simplified Newmark method can be used, which estimates Newmark displacement as a function of landslide critical acceleration and earthquake shaking intensity.

One of the principal causes of earthquake damage is landsliding triggered by strong shaking. Earthquakes with magnitudes greater than 4.0 can trigger landslides on very susceptible slopes, and earthquakes with magnitudes greater than 6.0 can generate widespread landsliding (*1*). Accurately predicting which slopes will move and the severity of that movement, however, is difficult. In this paper a brief review of some published methods to predict earthquake-triggered slope displacement is given and it is demonstrated how these methods can be applied to practical problems. The ability to predict approximate amounts of earthquake-induced landslide movement can be used for regional seismic-hazard analysis and in designing slopes to withstand earthquake shaking.

The seismic performance of a slope can be evaluated in several ways. The simplest approach is pseudostatic analysis, in which an earthquake acceleration acting on the mass of a potential landslide is treated as a permanent static body force in a limit-equilibrium (factor-of-safety) analysis. Different earthquake accelerations are applied until the factor of safety is reduced to 1.0. The earthquake acceleration needed to reduce the factor of safety to 1.0 is called the yield acceleration, the exceedance of which is defined as failure. This procedure is simple and requires no more information than is needed for a static factor-of-safety analysis. Pseudostatic analysis is useful for identifying yield accelerations and hence peak ground accelerations (PGA) below which no slope displacement will occur. In cases where the PGA does exceed the yield acceleration, pseudostatic analysis has proved to be vastly overconservative because many slopes experience transient earthquake accelerations well above their yield accelerations but experience little or no permanent displacement (*2*). The utility of pseudostatic analysis is thus limited because it provides only a single numerical threshold below which no displacement is predicted and above which total, but undefined, "failure" is predicted. In fact, pseudostatic analysis tells the user nothing about what will occur when the yield acceleration is exceeded.

At the other end of the spectrum, advances in two-dimensional finite-element modeling have facilitated very accurate evaluation of strain potentials and permanent slope deformation (*3–6*). These highly sophisticated methods require a broad spectrum of data of extremely high quality and density, which, combined with the intensive computing capacity required, makes their general use prohibitively expensive (*7*).

Newmark (*8*) proposed a method of analysis that bridges the gap between simplistic pseudostatic analysis and sophisticated, but generally impractical, finite-element modeling. Newmark's method models a landslide as a rigid-plastic friction block having a known yield or critical acceleration, the acceleration required to overcome frictional resistance and initiate sliding on an inclined plane. The analysis calculates the cumulative permanent displacement of the block as it is subjected to the effects of an earthquake acceleration-time history, and the user judges the significance of the displacement. Laboratory model tests (*9*) and analyses of earthquake-induced landslides in natural slopes (*2*) confirm that Newmark's method fairly accurately predicts slope displacements if slope geometry, soil properties, and earthquake ground accelerations are known. Newmark's method is relatively simple to apply and provides a quantitative prediction of the inertial landslide displacement that will result from a given level of earthquake shaking. Results from Newmark's method also are useful in probabilistic analyses (*10,11*), which further enhances their utility.

PAST APPLICATIONS OF NEWMARK'S METHOD

Newmark's method has been applied rigorously in a variety of ways to slope-stability problems. Most applications have dealt with the seismic performance of dams and embankments (*11,12*), which was Newmark's original intent (*8*). Newmark's

U.S. Geological Survey, Box 25046, MS 966, Denver Federal Center, Denver, Colo. 80225.

method also has been successfully applied to landslides in natural slopes (*2*). Several simplified approaches have been proposed for applying Newmark's method; these involve developing empirical relationships to predict slope displacement as a function of critical acceleration and one or more measures of earthquake shaking. Virtually all such studies plot displacement against critical acceleration ratio—the ratio of critical acceleration to PGA. Figure 1 shows the approximate locations of such plots from three studies (*12–14*). The relationship between critical acceleration ratio and displacement is magnitude dependent, as shown by separate curves for different magnitudes in two of the studies (*12,14*); the single curve from Ambraseys and Menu (*13*) is for a narrow range of magnitudes. Interestingly, no general agreement on the locations or even the shapes of the curves is apparent; predicted displacements for a given critical acceleration ratio and magnitude differ by as much as two orders of magnitude. Clearly, no universally applicable relationship between critical acceleration ratio and displacement exists at present.

Other studies of this type have related critical acceleration ratio to some normalized form of displacement that could not be compared directly with the curves in Figure 1. Yegian et al. (*11*) calculated exceedance probabilities for displacement normalized by PGA, the equivalent number of earthquake shaking cycles, and the square of the period of the base motion. Lin and Whitman (*10*) used simple, artificial ground-motion wave forms (triangular, rectangular, or sinusoidal) to relate critical acceleration ratio to displacement normalized by PGA.

Wilson and Keefer (*2*) applied Newmark's method to a landslide triggered by the 1979 Coyote Creek, California, earthquake. The slide occurred near a strong-motion instrument, and the landslide displacement predicted in the Newmark analysis using the record from that instrument agreed well with the observed displacement. This method of using real acceleration-time histories to predict displacements in natural slopes has been applied to experimentally predict and map seismic slope stability in San Mateo County, California (*15*). It also has been adapted to back-analyze shaking conditions required to trigger landslides formed in the Mississippi Valley during the 1811–1812 New Madrid earthquakes (*16*).

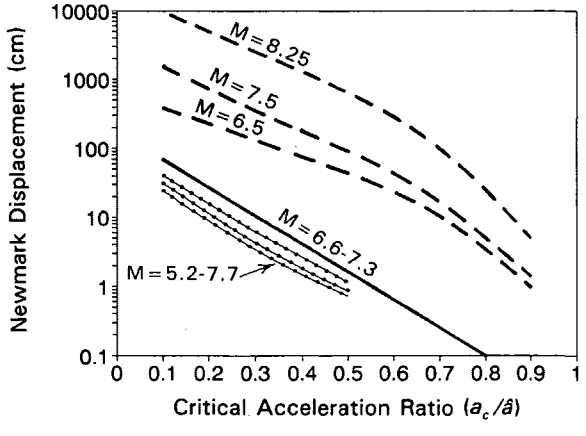

FIGURE 1 Newmark displacement as a function of critical acceleration ratio plotted from the results of three studies: Makdisi and Seed (*12*), dashed lines; Ambraseys and Menu (*13*), solid line; and Franklin and Chang (*14*), dotted lines.

CONDUCTING A NEWMARK ANALYSIS

Before describing the application of Newmark's method, the limiting assumptions need to be stated. Newmark's method treats a landslide as a rigid-plastic body; that is, the mass does not deform internally, experiences no permanent displacement at accelerations below the critical or yield level, and deforms plastically along a discrete basal shear surface when the critical acceleration is exceeded. Thus, Newmark's method is best applied to translational block slides and rotational slumps. Other limiting assumptions commonly are imposed for simplicity but are not required by the analysis:

1. The static and dynamic shearing resistance of the soil are taken to be the same (*7,8*).
2. The effects of dynamic pore pressure are neglected. This assumption generally is valid for compacted or overconsolidated clays and very dense or dry sands (*8,12*).
3. The critical acceleration is not strain dependent and thus remains constant throughout the analysis (*7,8,12,13*).
4. The upslope resistance to sliding is taken to be infinitely large such that upslope displacement is prohibited (*7,8,13*).

The procedure for conducting a Newmark analysis is outlined in the following sections and simple examples of its application are provided.

Critical Acceleration

The first step in the analysis is to determine the critical acceleration of the potential landslide. One way to do this is to use pseudostatic analysis, where critical acceleration is determined by iteratively employing different permanent horizontal earthquake accelerations in a static limit-equilibrium analysis until a factor of safety of 1.0 is achieved.

Newmark (*8*) simplified this approach by showing that the critical acceleration of a potential landslide is a simple function of the static factor of safety and the landslide geometry; it can be expressed as

$$a_c = (\mathrm{FS} - 1)g \sin \alpha \quad (1)$$

where a_c is the critical acceleration in terms of g, the acceleration due to earth's gravity; FS is the static factor of safety; and α is the angle (herein called the thrust angle) from the horizontal that the center of mass of the potential landslide block first moves. Thus, determining the critical acceleration by this method requires knowing the static factor of safety and the thrust angle.

Factor of Safety

As noted by Newmark (*8*), modeling dynamic slope response requires undrained or total shear-strength parameters. During earthquakes, slope materials behave in an undrained manner

because excess pore pressures induced by dynamic deformation of the soil column cannot dissipate during the brief duration of the shaking. Undrained strength also is called total strength because the contributions of friction, cohesion, and pore pressure are not differentiated, and the total strength is expressed as a single quantity.

The factor of safety can be determined using any appropriate method that uses undrained or total shear strength. In materials whose drained and undrained behaviors are similar, drained or effective shear strengths could be used if undrained strengths were unavailable or difficult to measure. This allows great flexibility for users. For a rough estimate of displacement, a simple factor-of-safety analysis, perhaps of an infinite slope using estimated shear strength, could be used. At the other end of the spectrum, a highly detailed site study could be conducted to determine the factor of safety very accurately. Clearly, the accuracy of the safety factor, and the resulting predicted displacement, depends on the quality of the data and analysis, but the user determines what is appropriate.

Thrust Angle

The thrust angle is the direction in which the center of gravity of the slide mass moves when displacement first occurs. For a planar slip surface parallel to the slope (an infinite slope), this angle is the slope angle. For simple planar block sliding, the thrust angle is the inclination of the basal shear surface. For circular rotational movement, Newmark (*8*) showed that the thrust angle is the angle between the vertical and a line segment connecting the center of gravity of the slide mass and the center of the slip circle. For irregular shear surfaces, the thrust angle can be approximated visually by estimating an "equivalent" circular surface or by averaging the inclinations of line segments approximating the surface.

Calculation of Critical Acceleration

Figure 2 shows a simple hypothetical slope and the critical failure surface having the lowest factor of safety (1.4) in undrained conditions. Newmark's (*8*) geometric construction indicates a thrust angle of 30 degrees. According to Equation 1, a factor of safety of 1.4 and a thrust angle of 30 degrees would yield a critical acceleration of 0.20 *g*.

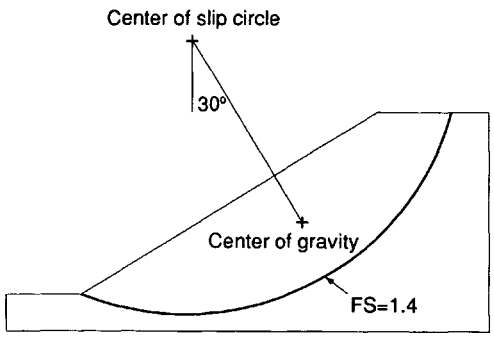

FIGURE 2 Model of hypothetical slope: basal shear surface, heavy line; FS, factor of safety; thrust angle is 30 degrees.

Selection of Earthquake Acceleration-Time History

The most difficult aspect of conducting a Newmark analysis is selecting an input ground motion, and many ways of doing so have been proposed. Most studies have used some combination of the two approaches mentioned by Newmark: (*a*) scaling acceleration-time histories from actual earthquakes to a desired level of PGA (*12,14*) and (*b*) using single or multiple cycles of artificial acceleration pulses having simple rectangular, triangular, or sinusoidal shapes (*10,11*). Both of these approaches yield useful results, but both also have inherent weaknesses. Scaling an acceleration-time history by simply expanding or contracting the acceleration scale does not accurately represent ground motion from earthquakes of different magnitudes or proximities because magnitude and source distance also affect the duration and predominant periods of shaking. And using simple artificial pulses of ground shaking is an unnecessary oversimplification in light of the current availability of digitized acceleration-time histories having a broad range of attributes.

Selecting a time history requires the user to know something of the shaking characteristics or design requirements pertinent to the situation of interest. Common design or hazard-assessment criteria include (*a*) a specified level of ground shaking, (*b*) a model earthquake of specified magnitude and location, or (*c*) an acceptable design amount of earthquake-triggered displacement.

Specified Level of Ground Shaking

Criterion a is by far the simplest; it requires only that the user locate a sampling of digitized acceleration-time histories having the desired measure of earthquake shaking intensity near the specified level. PGA is a common measure of ground-shaking intensity, and digitized time histories having a wide variety of PGAs, even exceeding 1 *g*, are currently available.

PGA measures only a single point in an acceleration-time history and is thus a rather crude measure of shaking intensity. A more comprehensive and quantitative measure of total shaking intensity developed by Arias (*17*) is useful in seismic hazard analysis and correlates well with the distribution of earthquake-induced landslides (*18*). Arias intensity is the integral over time of the square of the acceleration, expressed as

$$I_a = \pi/2g \int [a(t)]^2 \, dt \qquad (2)$$

where I_a is Arias intensity, in units of velocity, and $a(t)$ is the ground acceleration as a function of time. An Arias intensity thus can be calculated for each directional component of a strong-motion record. In cases where a given level of Arias intensity can be specified, selecting a strong-motion record of similar intensity is quite simple, and currently available records span a range of Arias intensities up to $I_a \approx 10$ m/sec.

Specified Earthquake Magnitude and Location

Criterion b can be somewhat more difficult. If acceleration-time histories exist for earthquakes of the desired magnitude that were recorded at appropriate distances, they can be used. Satisfying both magnitude and distance requirements is often impossible, however, so it may be necessary to estimate shaking characteristics at the site of interest using published empirical or theoretical relationships that predict PGA, duration, and Arias intensity as a function of earthquake magnitude and source distance. Estimated shaking characteristics can then be compared with those from existing time histories to provide a basis for selecting appropriate records.

An example of this procedure is from the Mississippi Valley, where large earthquakes occurred in 1811–1812 but where no strong-motion records exist. The problem is to predict the performance of a slope in a moment-magnitude (M) 6.2 earthquake centered at least 8 km away. If no time histories for that magnitude and distance existed, shaking characteristics at the site would have to be estimated.

PGA can be estimated using the attenuation relationship of Nuttli and Herrmann (*19*) for soil sites in the central United States:

$$\log \hat{a} = 0.57 + 0.50m_b - 0.83 \log (R^2 + h^2)^{1/2} - 0.00069R \quad (3)$$

where

$\hat{a}$ = PGA (cm/sec^2),
m_b = body-wave magnitude,
R = epicentral distance (km), and
h = focal depth (km).

An M6.2 earthquake corresponds to $m_b = 5.8$ (*20*). For $m_b = 5.8$, an epicentral distance of 8 km, and a minimum focal depth of 3 km, Equation 3 predicts a PGA of 491 cm/sec^2 or 0.50 g.

Estimating the Arias intensity at the site can be done in more than one way. Wilson and Keefer (*21*) developed a relationship among Arias intensity, earthquake magnitude, and source distance:

$$\log I_a = \mathbf{M} - 2 \log R - 4.1 \quad (4)$$

where I_a is in meters per second, M is moment magnitude, and R is earthquake source distance in kilometers. For M6.2 and $R = 8$ km, Equation 4 predicts an Arias intensity at the site of 1.97 m/sec.

Arias intensity also correlates closely with the combination of PGA and duration. R. C. Wilson (U.S. Geological Survey, unpublished data) developed an empirical equation using 43 strong-motion records to predict Arias intensity from PGA and a specific measure of duration:

$$I_a = 0.9T\hat{a}^2 \quad (5)$$

where I_a is in meters per second, $\hat{a}$ is PGA in g's, and T is duration (hereafter called Dobry duration) in seconds, defined as the time required to build up the central 90 percent of the Arias intensity (*22*). Estimating Arias intensities using this method requires an estimate of the duration of strong shaking. Dobry et al. (*22*) proposed an empirical relationship between duration and earthquake magnitude:

$$\log T = 0.432M - 1.83 \quad (6)$$

where T is Dobry duration in seconds and M is unspecified earthquake magnitude (probably local magnitude, M_L). In the magnitude range of interest, M_L-values are generally identical to M-values (*20*), so $M = 6.2$ yields a Dobry duration of 7.1 sec. If this duration and the PGA of 0.50 g estimated above are used in Equation 5, an Arias intensity of 1.59 m/sec is predicted, which agrees fairly well with that estimated by Equation 4.

These three indexes of shaking intensity—PGA, duration, and Arias intensity—form a rational basis for selecting strong-motion records for analysis. Caution and judgment must be used in making these estimates, however, because the process of combining values from Equations 3–6, each of which has a range of possible error, compounds the uncertainty at each step. For this example, three records are chosen whose shaking characteristics reasonably match those estimated (Table 1). Selecting multiple records that span the range of estimated shaking characteristics provides a range of displacements whose significance the user can judge.

Specified Design Displacement

Criterion c differs from the first two in that a limiting damage level (landslide displacement) is specified rather than the level of ground shaking. An example is to estimate the maximum level of ground shaking a slope having a critical acceler-

TABLE 1 Shaking Characteristics of Strong-Motion Records

Earthquake Recording Site, Component	PGA[a] (g)	Duration[b] (s)	I_a[c] (m/s)	Displacement[d] (cm)
Example Site (estimated values)	0.50	7.1	1.59-1.97	
27 June 1966 Parkfield, Calif. Parkfield Station 2, 65°	0.49	4.1	1.64	10.9
15 Oct. 1979 Imperial Valley, Calif. El Centro Array #8, 140°	0.61	6.8	1.60	3.5
Oct. 1979 Imperial Valley, Calif. El Centro Differential Array, 360°	0.49	6.6	2.12	3.9

[a] Peak ground acceleration
[b] Duration as defined by Dobry et al. (*22*)
[c] Arias intensity
[d] Calculated by Newmark's method

ation of 0.20 g could experience without exceeding 10 cm of displacement.

One approach to this problem is simply to analyze iteratively several strong-motion records to find those that yield about 10 cm of displacement at $a_c = 0.20\,g$. The magnitudes, source distances, focal depths, PGAs, Arias intensities, and durations of these records could then be examined to discern the approximate range of conditions the slope could withstand. Obviously, this approach could be time consuming, but it would produce a variety of possible threshold ground-shaking scenarios.

An easier approach to this type of problem is to apply the simplified Newmark method discussed subsequently.

Calculating Newmark Displacement

Once the critical acceleration of the landslide has been determined and the acceleration-time histories have been selected, Newmark displacement can be calculated by double integrating those parts of the strong-motion record that lie above the critical acceleration. Several methods for doing this, some rigorous and others highly simplified, have been proposed (*7,8,12,13*); perhaps the most useful rigorous method was developed by Wilson and Keefer (*2*). Figure 3*A* shows a strong-motion record having a hypothetical a_c of 0.2 g superimposed. To the left of Point X, accelerations are less than a_c, and no displacement occurs. To the right of Point X, those parts of the strong-motion record lying above a_c are integrated over time to derive a velocity profile of the block. Integration begins at Point X (Figure 3*A* and *B*), and the velocity increases to Point Y, the maximum velocity for this pulse. Past Point Y, the ground acceleration drops below a_c, but the block continues to move because of its inertia. Friction and ground motion in the opposite direction cause the block to decelerate until it stops at Point Z. All pulses of ground motion exceeding a_c are integrated to yield a velocity profile (Figure 3*B*), which in turn is integrated to yield a cumulative displacement profile of the landslide block (Figure 3*C*).

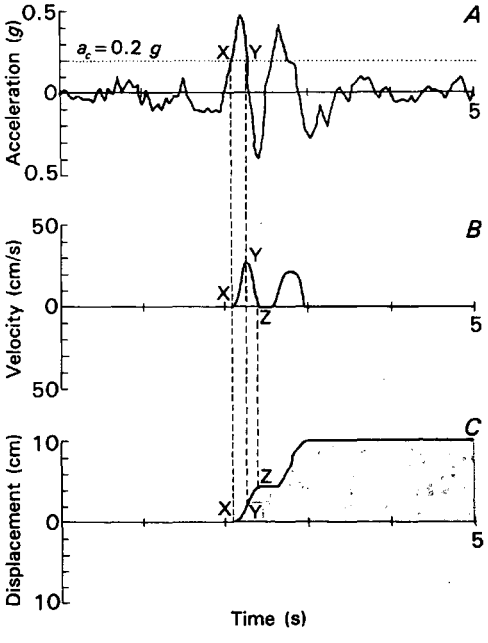

FIGURE 3 Demonstration of the Newmark-analysis algorithm, adapted from Wilson and Keefer (*2*). Points X, Y, and Z are discussed in text; *A*, earthquake acceleration-time history with critical acceleration (*dotted line*) of 0.20 g superimposed; *B*, velocity of landslide block versus time; *C*, displacement of landslide block versus time.

The algorithm of Wilson and Keefer (*2*) permits both downslope and upslope displacement by using the thrust angle to explicitly account for the asymmetrical resistance to downslope and upslope sliding. If pseudostatic yield acceleration is used and the thrust angle is not readily obtainable, the program can be simplified to prohibit upslope displacement. This prohibition was justified by Newmark (*8*), as well as by others (*7,10,13,14*), because a_c in the upslope direction is generally so much greater than a_c in the downslope direction that it can be assumed to be infinitely large. In most cases, the upslope a_c is greater than the PGA, and no error is introduced by prohibiting upslope displacement.

Integration programs for calculating Newmark displacement can be customized to accept acceleration-time histories in either of two formats: successive pairs of time and acceleration values or a single string of acceleration values sampled at a constant time interval. The latter is the simpler approach and ensures that the integration is performed consistently throughout the time history. Table 2 shows a simple BASIC program that uses the algorithm of Wilson and Keefer (*2*) modified to prohibit upslope displacement; the program accepts a string of acceleration values at a constant time interval.

Digitized strong-motion records can be obtained in several ways. Analog strong-motion records can be manually digitized to obtain a data file of time-acceleration pairs. Such a file can be used in a Newmark integration program that accepts paired data, or it can be resampled at a constant time interval by a simple linear interpolation program. Also, strong-motion records from many worldwide earthquakes are available in digital format from the National Oceanic and Atmospheric Administration's National Geophysical Data Center in Boulder, Colorado.

SIMPLIFIED NEWMARK METHOD

The previous sections contained a description of how to rigorously conduct a Newmark analysis. Although this approach is straightforward, many of its aspects are difficult for the average user: acquiring digitized strong-motion records can be very time consuming, and locating an appropriate record for the conditions to be modeled is not always easy. Also, writing the integration program can be difficult. For these reasons, a simplified approach for estimating Newmark displacements would be helpful.

As discussed above, previous studies have proposed general relationships between Newmark displacement and some normalized parameter or parameters of critical acceleration (*10–14*). Any of these that include parameters appropriate to a problem of interest can be applied with relative ease. Most

TABLE 2 BASIC Program for Calculating Newmark Displacement

Program Step	Instruction
1	REM Program for calculating Newmark displacement
2	REM Input data should be in units of cm/s/s
3	PRINT "Input file should be in cm/s/s"
4	INPUT "What is the name of the input file";A$
5	OPEN "I", #1, A$
6	INPUT "What is the critical acceleration in g's";T:T=980.665*T
7	INPUT "What is the digitization interval in seconds";D
8	INPUT "What is the duration of the record in seconds";Z
9	K=Z/D
10	Q=0
11	R=0
12	S=0
13	Y=0
14	V=0
15	U=0
16	FOR I=1 TO K
17	INPUT #1,A
18	IF V<0.0001 THEN 20
19	GOTO 26
20	IF ABS(A)>T THEN 22
21	GOTO 24
22	N=A/ABS(A)
23	GOTO 27
24	N=A/T
25	GOTO 27
26	N=1
27	Y=A−N*T
28	V=R+D/2*(Y+S)
29	IF V>0 THEN 32
30	V=0
31	Y=0
32	U=Q+D/2*(V+R)
33	Q=U
34	R=V
35	S=Y
36	NEXT I
37	PRINT "Total displacement in centimeters is ";U
38	END

depend directly on PGA, which, as noted, is a widely used but rather crude measure of shaking intensity. Therefore, a simplified method based on Arias intensity, a better measure of shaking intensity, is proposed below.

To develop an empirical relationship among Newmark displacement, critical acceleration, and Arias intensity, 11 strong-motion records were selected having Arias intensities between 0.2 and 10.0 m/sec (Table 3), which span the range between the smallest shaking intensities that might cause landslide movement and the largest shaking intensities ever recorded. For each strong-motion record, Newmark displacement was calculated for several critical accelerations between 0.02 and 0.40 g, the range of practical interest for earthquake-induced landslides (Figure 4). Data points for each critical acceleration plot fairly linearly in the log-log space of Arias intensity versus Newmark displacement. Best-fit lines from regression models for each value of critical acceleration have excellent fits (R^2 = 0.81–0.95), and the lines are roughly parallel and proportionately spaced, which suggests that a multivariate model would fit the data well. Therefore, a multivariate regression model of the following form was constructed:

$$\log D_N = A \log I_a + Ba_c + C \pm \sigma \quad (7)$$

where

D_N = Newmark displacement (cm),
I_a = Arias intensity (m/sec),
a_c = critical acceleration (g),
A, B, C = regression coefficients, and
σ = estimated standard deviation of the model.

The resulting model has an R^2 of 0.87, and all coefficients are significant above the 99.9 percent confidence level:

$$\log D_N = 1.460 \log I_a - 6.642a_c + 1.546 \pm 0.409 \quad (8)$$

This model yields the mean Newmark displacement when σ is ignored; the variation (σ) about this mean results from the stochastic nature of earthquake ground shaking. Thus, two strong-motion records having identical Arias intensities can produce different Newmark displacements for slopes having the same critical acceleration. Therefore, Equation 8 yields a range of displacements that must be interpreted with considerable judgment. Figure 5 shows critical acceleration lines defined by Equation 8. The model underestimates Newmark displacement (Figure 4) at low levels of Arias intensity (less

TABLE 3 Strong-Motion Records Selected for Analysis

Earthquake Recording Site, Component	M [a]	PGA [b] (g)	Duration [c] (s)	I_a [d] (m/s)
15 Oct. 1979 Imperial Valley, Calif., Coachella Canal, Station 4, 135°	6.5	0.13	10.4	0.20
6 Aug. 1979 Coyote Lake, Calif., Coyote Creek, San Martin, 250°	5.8	0.21	3.8	0.25
21 July 1952 Kern County, Calif., Taft School, 111°	7.5	0.14	17.7	0.46
6 Aug. 1979 Coyote Lake, Calif., Gilroy Array, San Ysidro School, 270°	5.8	0.23	8.5	0.60
15 Oct. 1979 Imperial Valley, Calif., Calexico Fire Station, 225°	6.5	0.28	11.1	0.86
1 Oct. 1987 Whittier Narrows, Calif., Bulk Mail Center, 280°	6.0	0.45	5.5	1.23
15 Oct. 1979 Imperial Valley, Calif., El Centro differential array, 360°	6.5	0.49	6.6	2.12
24 Nov. 1987 Superstition Hills, Calif., Parachute Test Site, 225°	6.5	0.46	10.1	4.15
15 Oct. 1979 Imperial Valley, Calif., Bonds Corner, 230°	6.5	0.79	9.8	6.00
9 Feb. 1971 San Fernando, Calif., Pacoima Dam, 164°	6.6	1.22	6.7	9.08
16 Sept. 1978 Tabas, Iran, 74°	7.4	0.71	16.1	9.96

[a] Moment magnitude
[b] Peak ground acceleration
[c] Duration as defined by Dobry et al. (22)
[d] Arias intensity

than 0.5 m/sec) for very small critical accelerations (0.02 g), but otherwise the data are well fit by the model.

Equation 8 can be applied to the example summarized in Table 1. For the lower estimated Arias intensity of 1.59 m/sec and a critical acceleration of 0.2 g, the mean value from Equation 8 is 3.2 cm, and the range bracketing two standard deviations is 1.3 to 8.3 cm. For the higher value of Arias intensity of 1.97 m/sec, Equation 8 yields a mean value of 4.4 cm and a range of 1.7 to 11.4 cm. Displacements calculated from the three selected strong-motion records fall within this range, and the mean values from Equation 8 are very close to two of the three calculated displacements. Thus, the simplified Newmark method presented here yields reasonable results.

Equation 8 and Figure 5 can be applied to estimate the dynamic performance of any slope of known critical acceleration because they are derived from generic values of critical acceleration that are not site specific. Thus, several types of

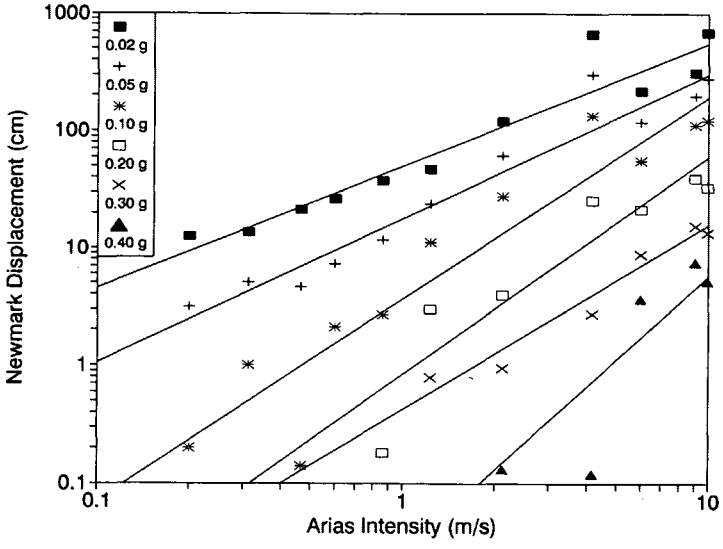

FIGURE 4 Newmark displacement plotted as a function of Arias intensity for different values of critical acceleration. Lines are best fits from regressions for each value of critical acceleration plotted.

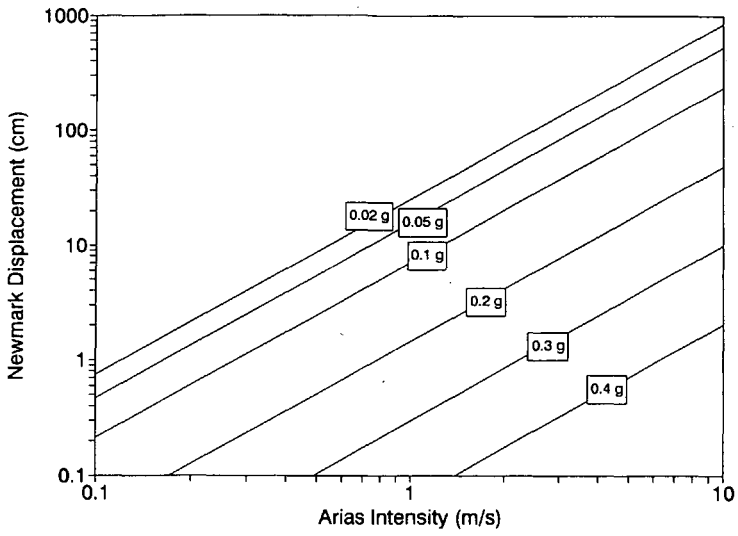

FIGURE 5 Newmark displacement as a function of Arias intensity for several values of critical acceleration as modeled by the regression equation shown.

hazard analyses for earthquake-triggered landslides can be developed:

1. If the Arias intensity at a site can be specified, and if the critical acceleration of the slope can be determined, the Newmark displacement can be estimated.
2. If critical displacement can be estimated and the critical acceleration of the slope is known, the threshold Arias intensity that will cause slope failure can be estimated.
3. If a critical displacement and Arias intensity can be estimated, the threshold critical acceleration below which slope failure will occur can be estimated.

INTERPRETING NEWMARK DISPLACEMENTS

The significance of Newmark displacements must be judged by their probable effect on a potential landslide. Wieczorek et al. (*15*) used 5 cm as the critical displacement leading to macroscopic ground cracking and general failure of landslides in San Mateo County, California; Keefer and Wilson (*23*) used 10 cm as the critical displacement for coherent landslides in southern California; and Jibson and Keefer (*16*) used this 5- to 10-cm range as the critical displacement for landslides in the Mississippi Valley. In most soils, displacements in this range cause ground cracking, and previously undeformed soils can lose some of their peak shear strength and end up in a weakened or residual-strength condition. In such a case of strength loss, a static stability analysis in residual-strength conditions can be performed to determine the slope stability after earthquake shaking ceases.

Any level of critical displacement can be used according to the parameters of the problem under study and the characteristics of the landslide material. Highly ductile materials may be able to accommodate more displacement without general failure; brittle materials might accommodate less displacement. What constitutes failure may vary according to the needs of the user. Results of laboratory shear-strength tests can be interpreted to estimate the strain necessary to reach residual strength.

DISCUSSION OF RESULTS

Any idealized model is limited by its simplifying assumptions. The fundamental assumption of Newmark's model is that landslides behave as rigid-plastic materials; that is, no displacement occurs below the critical acceleration, and displacement occurs at constant shearing resistance when the critical acceleration is exceeded. This assumption is reasonable for some types of landslides in some types of materials but it certainly does not apply universally. Many slope materials are at least slightly sensitive—they lose some of their peak undrained shear strength as a function of strain. In such a case, Newmark's method would underestimate the actual displacement because the strength loss during shear would reduce the critical acceleration as displacement occurs. For such materials, the Newmark displacement might be considered a minimum displacement and so would be unconservative.

Some highly plastic, fine-grained soils behave as viscoplastic rather than rigid-plastic materials. The viscous response of these soils results in part from low permeability and high cohesion, and the result can be a radically dampened seismic response. Some active, slow-moving landslides having factors of safety at or below 1.0 have experienced negligible inertial displacement even during large earthquakes (*24*) because of viscous energy dissipation. In Newmark's method, displacement depends on the critical acceleration, which in turn depends on the static factor of safety. Therefore, a landslide at or very near static equilibrium should have a very low critical acceleration (theoretically, $a_c = 0$ if FS = 1) and thus should undergo large inertial displacements in virtually any earth-

quake. Thus, Newmark's method probably overestimates landslide displacements in viscoplastic materials.

Generally, Newmark's method has considered static and dynamic shear strength to be the same and has ignored dynamic pore-pressure response; this has permitted use of static shear strengths, which are much more easily determined than dynamic strengths. For many soils, this assumption introduces little error, but static and dynamic strengths differ significantly for some soils. In such cases, dynamic shear-strength testing may be required, or static strengths can be adjusted by an empirical correction factor (*12*). Similarly, dynamic pore-pressure response, if considered significant, can be measured in dynamic tests or accounted for empirically by reducing the static shear strength.

Ongoing research is addressing ways to account for strain-dependent strength reduction, viscoplastic behavior, and the effects of the vertical component of ground shaking. Results of such research will facilitate refinement of dynamic landslide modeling and improve the ability to predict dynamic slope response.

CONCLUSION

Newmark's method is useful for characterizing seismic slope response. It presents a viable compromise between simplistic pseudostatic analysis and sophisticated finite-element modeling, and it can be applied to a variety of problems in seismic slope stability. The new simplified method presented here provides an easy way to estimate ranges of possible displacement in cases where the seismic shaking intensity can be estimated.

REFERENCES

1. Keefer, D. K. Landslides Caused by Earthquakes. *Geological Society of America Bulletin,* Vol. 95, No. 6, 1984, pp. 406–421.
2. Wilson, R. C., and D. K. Keefer. Dynamic Analysis of a Slope Failure from the 6 August 1979 Coyote Lake, California, Earthquake. *Bulletin of the Seismological Society of America,* Vol. 73, No. 3, 1983, pp. 863–877.
3. Elgamal, A. W., A. M. Abdel-Ghaffar, and J. H. Prevost. 2-D Elastoplastic Seismic Shear Response of Earth Dams: Application. *Journal of Geotechnical Engineering,* Vol. 113, No. 5, 1987, pp. 702–719.
4. Prevost, J. H., A. M. Abdel-Ghaffar, and S. J. Lacy. Nonlinear Dynamic Analysis of an Earth Dam. *Journal of Geotechnical Engineering,* Vol. 111, No. 7, 1985, pp. 882–897.
5. Seed, H. B., K. L. Lee, I. M. Idriss, and F. I. Makdisi. The Slides in the San Fernando Dams During the Earthquake of February 9, 1971. *Journal of the Geotechnical Engineering Division,* ASCE, Vol. 101, No. 7, 1975, pp. 651–688.
6. Taniguchi, E., R. V. Whitman, and W. A. Marr. Prediction of Earthquake-Induced Deformation of Earth Dams. *Soils and Foundations,* Vol. 23, No. 4, 1983, pp. 126–132.
7. Chang, C. J., W. F. Chen, and J. T. P. Yao. Seismic Displacements in Slopes by Limit Analysis. *Journal of Geotechnical Engineering,* Vol. 110, No. 7, 1984, pp. 860–874.
8. Newmark, N. M. Effects of Earthquakes on Dams and Embankments. *Geotechnique,* Vol. 15, No. 2, 1965, pp. 139–159.
9. Goodman, R. E., and H. B. Seed. Earthquake-Induced Displacements in Sand Embankments. *Journal of the Soil Mechanics and Foundations Division,* ASCE, Vol. 92, No. SM2, 1966, pp. 125–146.
10. Lin, J. S., and R. V. Whitman. Earthquake Induced Displacements of Sliding Blocks. *Journal of Geotechnical Engineering,* Vol. 112, No. 1, 1986, pp. 44–59.
11. Yegian, M. K., E. A. Marciano, and V. G. Ghahraman. Earthquake-Induced Permanent Deformations: Probabilistic Approach. *Journal of Geotechnical Engineering,* Vol. 117, No. 1, 1991, pp. 35–50.
12. Makdisi, F. I., and H. B. Seed. Simplified Procedure for Estimating Dam and Embankment Earthquake-Induced Deformations. *Journal of the Geotechnical Engineering Division,* ASCE, Vol. 104, No. GT7, 1978, pp. 849–867.
13. Ambraseys, N. N., and J. M. Menu. Earthquake-Induced Ground Displacements. *Earthquake Engineering and Structural Dynamics,* Vol. 16, No. 7, 1988, pp. 985–1006.
14. Franklin, A. G., and F. K. Chang. *Earthquake Resistance of Earth and Rock-Fill Dams: Permanent Displacements of Earth Embankments by Newmark Sliding Block Analysis.* Miscellaneous Paper S-71-17, Report 5. U.S. Army Engineer Waterways Experiment Station, Vicksburg, Miss., 1977.
15. Wieczorek, G. F., R. C. Wilson, and E. L. Harp. *Map Showing Slope Stability During Earthquakes in San Mateo County, California.* Miscellaneous Investigations Map I-1257-E. U.S. Geological Survey, 1985.
16. Jibson, R. W., and D. K. Keefer. Analysis of the Seismic Origin of Landslides: Examples from the New Madrid Seismic Zone. *Geological Society of America Bulletin,* Vol. 105, No. 4, 1993, pp. 521–536.
17. Arias, A. A Measure of Earthquake Intensity. In *Seismic Design for Nuclear Power Plants,* Massachusetts Institute of Technology Press, Cambridge, 1970, pp. 438–483.
18. Harp, E. L., and R. C. Wilson. Shaking Intensity Thresholds for Seismically Induced Landslides. *Geological Society of America Abstracts with Programs,* Vol. 21, No. 5, 1989, p. 90.
19. Nuttli, O. W., and R. B. Herrmann. Ground Motion of Mississippi Valley Earthquakes. *Journal of Technical Topics in Civil Engineering,* Vol. 110, No. 1, 1984, pp. 54–69.
20. Heaton, T. H., F. Tajima, and A. W. Mori. Estimating Ground Motions Using Recorded Accelerograms. *Surveys in Geophysics,* Vol. 8, 1986, pp. 25–83.
21. Wilson, R. C., and D. K. Keefer. Predicting Areal Limits of Earthquake-Induced Landsliding. In *Evaluating Earthquake Hazards in the Los Angeles Region—An Earth-Science Perspective,* Professional Paper 1360, U.S. Geological Survey, 1985, pp. 316–345.
22. Dobry, R., I. M. Idriss, and E. Ng. Duration Characteristics of Horizontal Components of Strong-Motion Earthquake Records. *Bulletin of the Seismological Society of America,* Vol. 68, No. 5, 1978, pp. 1487–1520.
23. Keefer, D. K., and R. C. Wilson. Predicting Earthquake-Induced Landslides, With Emphasis on Arid and Semi-Arid Environments. In *Landslides in a Semi-Arid Environment,* Inland Geological Society, Riverside, Calif., Vol. 2, 1989, pp. 118–149.
24. Jibson, R. W., C. S. Prentice, C. J. Langer, E. A. Rogozhin, and B. A. Borissoff. Unusual Landslides and Other Strong-Shaking Effects of the 29 April 1991 Racha Earthquake in the Republic of Georgia. *Bulletin of the Seismological Society of America,* submitted 1992.

Publication of this paper sponsored by Committee on Engineering Geology.

Estimation of Earthquake-Induced Pile Bending in a Thick Peat Deposit

STEVEN L. KRAMER, MATTHEW A. CRAIG, AND SUJAN PUNYAMURTHULA

An investigation of the nature of earthquake-induced deformation of piles supporting highway bridges that cross a thick peat deposit in Washington State is presented. The results of a field and laboratory testing program were used to predict free-field ground response for several soil profiles representative of subsurface soil conditions across the site. The computed free-field soil displacements were used in an approximate soil-pile interaction analysis to estimate the curvature demand on different types of piles. The interaction analysis was based on three-dimensional finite element analysis of a pile embedded in a column of soil. The results indicated that the curvature demands on the piles were much smaller than the free-field curvatures but were still quite large.

The seismic response of piles in soft soil deposits is a problem of considerable interest and importance to geotechnical engineers and owners of pile-supported structures such as highway bridges. The need for careful attention to potential problems with pile-supported bridges in soft soil areas has been illustrated in many previous earthquakes, perhaps most recently in the 1989 Loma Prieta earthquake. The large displacements and eventual failure of the Struve Slough bridge in Watsonville, California, during the Loma Prieta earthquake emphasized the need for evaluation of potential pile deformations in very soft peat deposits. This paper presents the results of an investigation of the potential levels of earthquake-induced bending of piles extending through a thick peat deposit in Washington State.

PILE BENDING DURING EARTHQUAKES

Earthquake-induced ground shaking causes vertical and horizontal displacements of soil at and below the ground surface. The nature of the deformations depends on the geometry and material properties of the various soil and underlying rock units at the site and on the characteristics of the seismic waves that reach the site. Ground displacement amplitudes are typically small for small or distant earthquakes or for very stiff or dense soil profiles; however, they may become quite large in soft soil deposits. Displacement amplitudes are generally largest at the ground surface and tend to decrease with depth.

In soft soil areas, significant transportation structures such as highway bridges are often supported on deep foundations. These deep foundations may be subjected to lateral loading at their heads from traffic, thermal expansion, and other sources; methods for evaluating their response to such loads are now well established (*1–4*). When deep foundation elements extend through soft soils in seismically active areas, however, they may be subjected to a different form of lateral loading—that which is imposed by earthquake-induced displacement of the surrounding soils. Since earthquake-induced soil displacements are not uniform with depth, the soil displacement profile will be curved, thereby inducing bending moments in the piles. Soil profile curvatures are generally greatest at boundaries between materials of different stiffness. Damage to pile foundations for highway bridges has been observed in a number of earthquakes (*5–7*).

Until relatively recently, designers commonly assumed that the mass and stiffness of piles were sufficiently small that piles would move with the surrounding soil during earthquakes (*8,9*). As a result, the curvature demand for piles was considered to be equal to the maximum computed free-field soil profile curvature. Margason and Holloway (*8*) used numerical analyses to predict the curvature profile for a soft soil site in the San Francisco Bay area. The soil curvature profile was far from constant, with large pile curvatures occurring over relatively short vertical distances. The largest computed curvature was located at the boundary between soft Bay mud and an underlying layer of stiff clay at which the small strain impedance ratio was approximately 1.6. This computed soil curvature, approximately 4.0×10^{-4} in.$^{-1}$ (1.6×10^{-4} cm^{-1}), corresponded to a radius of curvature of about 208 ft (63.4 m), which exceeds the elastic limit of many piles. Margason and Holloway (*8*) indicated that maximum pile curvatures of 2.0 to 4.0×10^{-4} in.$^{-1}$ (0.8 to 1.6×10^{-4} cm^{-1}) could be expected for magnitude (**M**) 7.0 earthquakes and 8.0×10^{-4} in.$^{-1}$ (3.2×10^{-4} cm^{-1}) could be expected for **M**8.0 earthquakes in the San Francisco Bay area.

Banerjee et al. (*10*) repeated the analysis of the San Francisco Bay area profile for which Margason and Holloway had obtained a maximum curvature of 4.0×10^{-4} in.$^{-1}$ (1.6×10^{-4} cm^{-1}). Banerjee et al., however, performed a two-dimensional, soil-structure interaction analysis with a 12-in. (30.5-cm) precast, prestressed concrete pile embedded in the soil profile and found that the maximum computed pile curvature was only 2.2×10^{-4} in.$^{-1}$ (0.9×10^{-4} cm^{-1}), or slightly more than half of the free-field soil profile curvature. These analyses showed that the flexural stiffness of the pile was sufficient to span short distances of high-soil-profile curvature with significantly lower pile curvature. Other methods for analysis of seismic pile-soil interaction have also been developed.

Department of Civil Engineering, University of Washington, Seattle, Wash. 98195.

SITE CONDITIONS

The Puget Sound area of Washington State is well known as a seismically active region. Strong ground motion has been induced by a number of historical earthquakes, most recently by the 1949 Olympia (M7.1) and 1965 Seattle-Tacoma (M6.5) earthquakes. These earthquakes are thought to have been caused by the release of strain energy accumulated by bending of the Juan de Fuca plate as it subducts beneath the North American plate; a maximum magnitude of 7.5 is generally accepted for this mechanism. Recent research, however, indicates that much larger subduction earthquakes occurred before the Pacific Northwest was settled (*11,12*). The possibility of subduction-zone earthquakes of magnitude up to 9.5 has been postulated for the Pacific Northwest.

Mercer Slough is a peat-filled extension of Lake Washington that covers several square miles in Bellevue, Washington (Figure 1). Lake Washington water levels are maintained at a nearly constant depth at the Hiram Chittenden Locks in Seattle; consequently, the groundwater level in Mercer Slough is generally within 1 ft of the ground surface. The thickness of the Mercer Slough peat is variable across the slough, with a maximum thickness of approximately 60 ft (18.3 m) along the alignment of Interstate 90, which crosses Mercer Slough by means of four pile-supported bridge structures. Although some of the deepest peat has been dated at more than 13,000 years old, most was deposited after Lake Washington was isolated from Puget Sound by the Cedar River alluvial fan some 7,000 years ago (*13*). Since that time, the peat appears to have accumulated at a average rate of approximately 0.07 in./year (0.18 cm/year). The peat is underlain by very soft to medium stiff silty clay and occasional loose to dense sand, which is in turn underlain by heavily overconsolidated, dense glacial till. Tertiary bedrock in the area is at a depth of about 1,000 ft (305 m) (*14*). A subsurface profile of Mercer Slough along the I-90 alignment is shown in Figure 2.

The existing bridges across Mercer Slough are supported on vertical piles driven to depths sufficient to resist vertical design loads of 20 to 70 tons (178 to 623 kN) each. Piling consists of timber piles and 14- and 18-in. (35- and 46-cm) concrete-filled steel pipe piles. A distant landslide along Lake Washington Boulevard caused lateral movement of the bridge and, presumably, the pile foundations supporting the bridge. A previous investigation associated with that landslide (*15,16*) indicated that the Mercer Slough peat offers very little resistance to lateral movement of piles under static conditions.

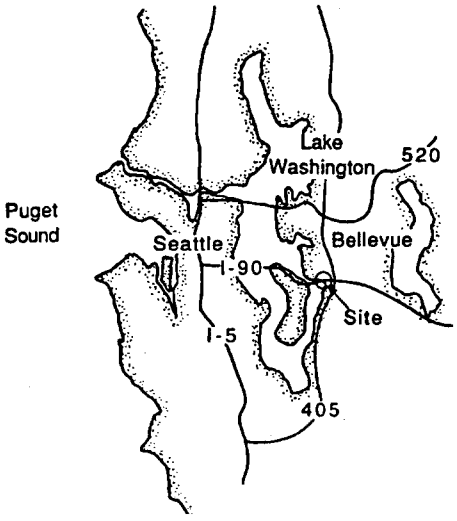

FIGURE 1 Location of Mercer Slough in Bellevue, Washington.

MERCER SLOUGH PEAT PROPERTIES

The unusual and problematic behavior of peats has been known for many years. Considerable progress has been made in understanding their long-term static behavior, thus allowing them to be dealt with rationally when they cannot be removed or avoided. Problems associated with the dynamic response of peat, however, have not been addressed.

Index and Static Properties

The Mercer Slough peat is fibrous at shallow depths and becomes less fibrous and more highly decomposed with increasing depth. In recent subsurface investigations, water contents were generally between approximately 500 percent and 1,200 percent, with no apparent trend with depth. Buoyant unit weights were generally less than 5 lb/in.^{3} (0.79 kN/m^3). The strength of the peat was very low (*16*); a cohesive strength of about 200 lb/ft^2 (9.6 kPa) appears to best represent its shearing resistance (*15*). A significant time-dependent response, in the form of creep and stress relaxation, has been observed in field and laboratory strength tests on Mercer Slough peat.

Dynamic Properties

Very little research has been performed on the dynamic properties of peat or on the dynamic response of peat deposits. The only such work identified in the literature was associated with the foundation investigation for a proposed (but never constructed) highway tunnel in the Union Bay area of Seattle, Washington (*17*). The Union Bay site, also located on Lake Washington but about 7 mi (11 km) northwest of Mercer Slough, consisted of up to 60 ft (18.3 m) of peat underlain by up to 80 ft (24.4 m) of soft to medium stiff clay. The clay was underlain by heavily overconsolidated, dense glacial till. In 1966, water contents in the Union Bay peat ranged from 700 to 1,500 percent at the surface, with a trend of slightly decreasing water content with increasing depth. Saturated unit weights ranged from 62.6 to 66.0 lb/in.^{3} (9.8 to 10.4 kN/m^3) and averaged 63.7 lb/ft^3 (10.0 kN/m^3). Atterberg limits tests showed liquid limits of 700 to 1,000 and plasticity indices of 200 to 600. The Union Bay and Mercer Slough peats were deposited under very similar conditions, and it is expected that their important geotechnical characteristics will also be similar. Seed and Idriss (*18*) interpreted the results of field and laboratory tests performed by Shannon & Wilson (*17*) to propose the dynamic properties shown in Figure 3. Shear moduli were obtained from shear wave velocity measurements and repeated loading tests. Damping ratios were estimated with the reasoning that "because of its fibrous and less co-

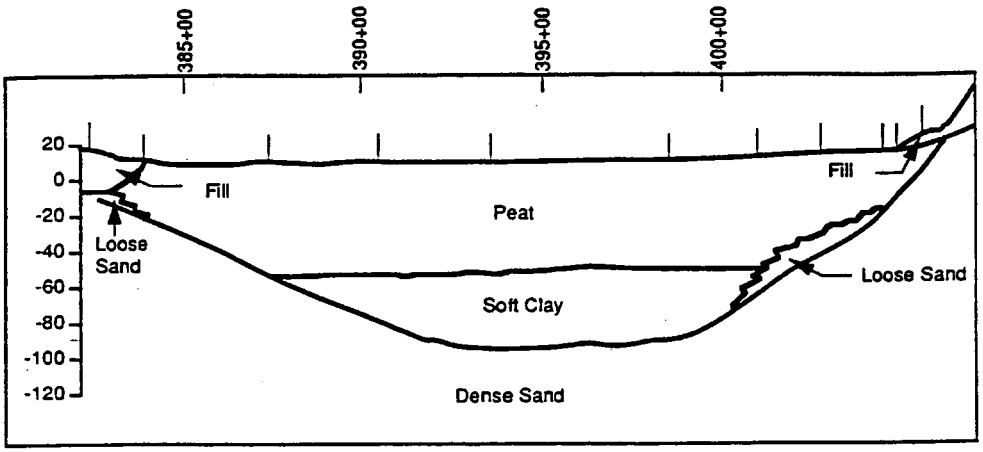

FIGURE 2 Subsurface profile of Mercer Slough along alignment of I-90 bridges (vertical scale exaggerated by factor of 10).

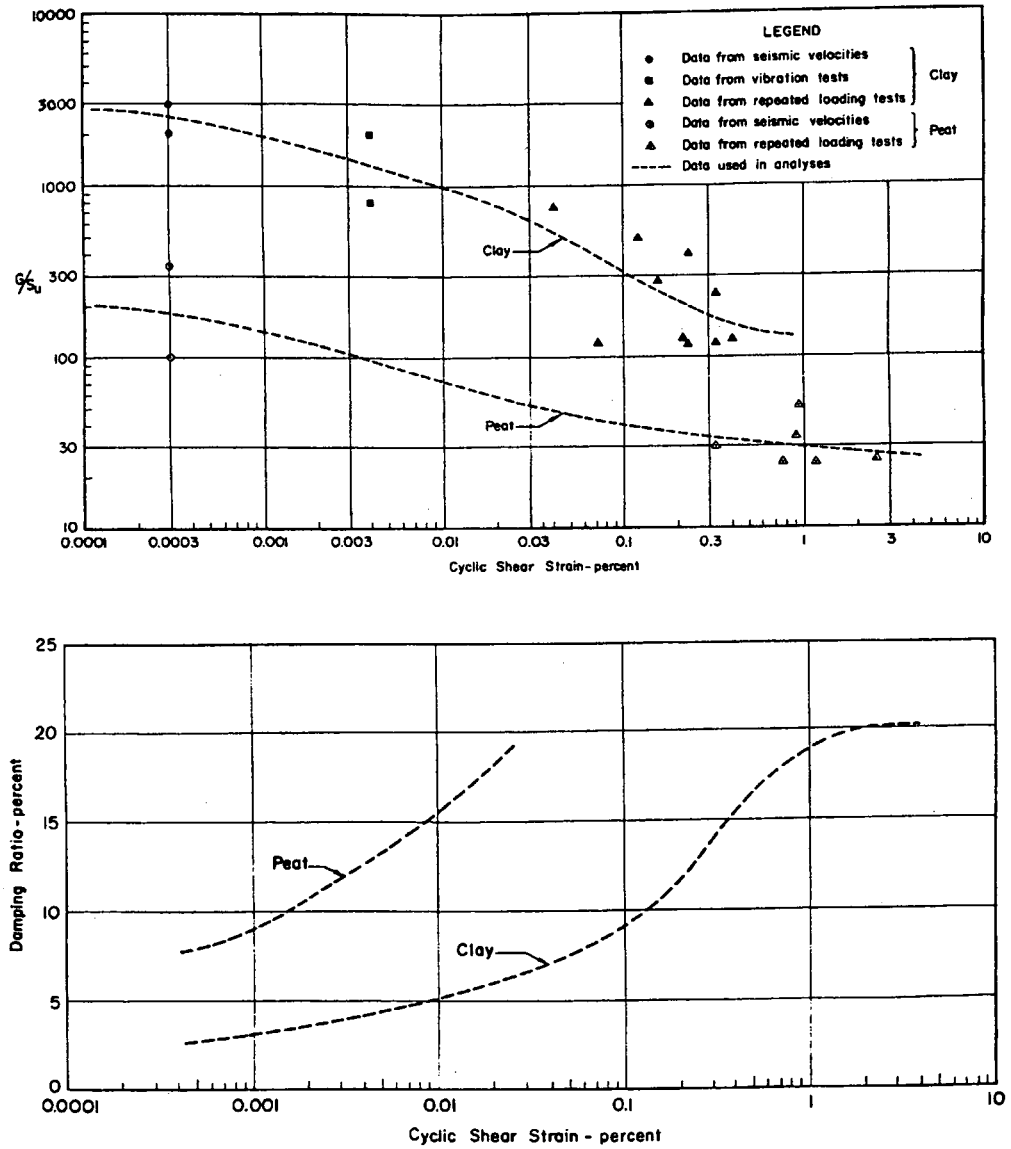

FIGURE 3 Peat properties assumed by Seed and Idriss (*18*).

hesive characteristics, damping for peat would be expected to be higher than for clay" (*18*). These damping ratios were approximately three times as large as those used at the time for clay.

A field and laboratory testing program was undertaken to evaluate the dynamic properties of the Mercer Slough peat. To estimate the low-strain stiffness of the peat, a seismic cone sounding was performed near the edge of a parking lot fill. The results of the sounding, shown in Figure 4, indicated that the peat had an average shear wave velocity of approximately 100 ft/sec (30 m/sec) despite having been consolidated to some extent by the overlying fill. An initial series of cyclic triaxial tests on undisturbed samples taken from the same location showed shear moduli greater than those inferred from the shear wave velocities. These results were considered unsatisfactory, and it was deemed necessary to obtain sample-specific low-strain stiffness data. The cyclic triaxial testing equipment was then modified by the addition of piezoelectric bender elements for subsequent testing. The resulting variation of normalized shear modulus with cyclic shear strain amplitude observed in a small number of cyclic triaxial-bender element tests on Mercer Slough peat is shown in Figure 5 (*top*); the shear modulus of the Mercer Slough peat samples degraded at a slower rate than that observed for inorganic clays (*19*). Damping ratio data, shown in Figure 5 (*bottom*), was typically scattered but showed a distinct and consistent trend of decreasing damping ratio with increasing strain amplitude above strain amplitudes of approximately 0.02 percent. The reason for this behavor is not yet understood; it may be related to stretching and straightening of the peat fibers at larger strain levels. Damping ratios could not be measured at lower strain amplitudes with the available testing equipment. Further research on the dynamic properties of the Mercer Slough peat and other peats is continuing.

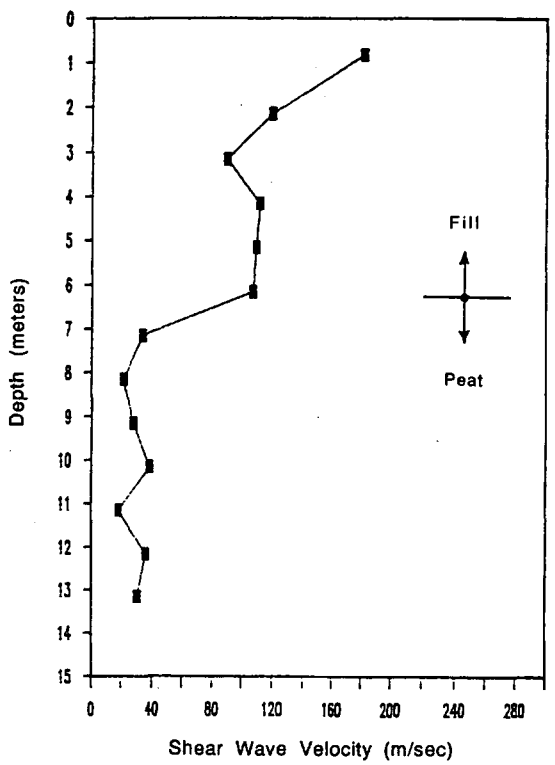

FIGURE 4 Results of seismic cone penetration test sounding.

GROUND RESPONSE ANALYSES

Very little information on the dynamic response of peat deposits is available in the literature. Seed and Idriss (*18,20*) analyzed recorded motions at Union Bay from a small (M4.5), distant (R = 49 km) earthquake using an equivalent linear, lumped mass technique. The motion measured in the glacial till, which had a peak acceleration of 0.03 g, was applied as a rigid base motion (I. M. Idriss, personal communication, 1991) at the clay-till interface, and reasonable agreement was obtained between the measured and predicted accelerations. Because the level of shaking was very low, however, the nonlinear behavior of the peat was not significant.

For a large, design-level ground motion at the Mercer Slough site, nonlinear behavior is expected to be significant. In order to investigate the effects of the measured dynamic peat properties on ground-shaking characteristics during such earthquakes, a series of ground response analyses was performed.

Soil Profiles

Soil conditions along the I-90 alignment were divided into the five ground-response zones shown in Figure 6. The typical soil profiles for the ground-response zones are given in Table 1. As indicated by the total thickness of each soil profile, the depth to bedrock was assumed to be 1,000 ft (305 m). Subsurface investigations indicated that the fill was loose and cohesionless with Standard Penetration Test resistances similar to that of the loose sand layer. The fill and loose sand layer were consequently assigned a K_{2max}-value of 51.8. The soft clay deposit beneath the Mercer Slough peat in the central portion of the site had an average plasticity index of approximately 20 and was modeled as such using the modulus and damping ratio curves of Vucetic and Dobry (*19*). The glacial till consisted primarily of dense sand and gravel and was modeled as a dense sand with K_{2max} = 80. Bedrock was assigned a shear wave velocity of 8,000 ft/sec.

Input Motions

The design ground motion was assumed, for consistency with other nearby Washington State Department of Transportation projects, to have a peak bedrock acceleration of 0.30 g and a predominant period of 0.36 sec. The response of each soil profile was computed using three separate bedrock motions, which were obtained by scaling the El Centro, Lake Hughes, and Castaic historical records to produce the characteristics of the design ground motion.

Computed Ground Motions

Ground response was computed using the well-known one-dimensional, equivalent linear, complex response method in-

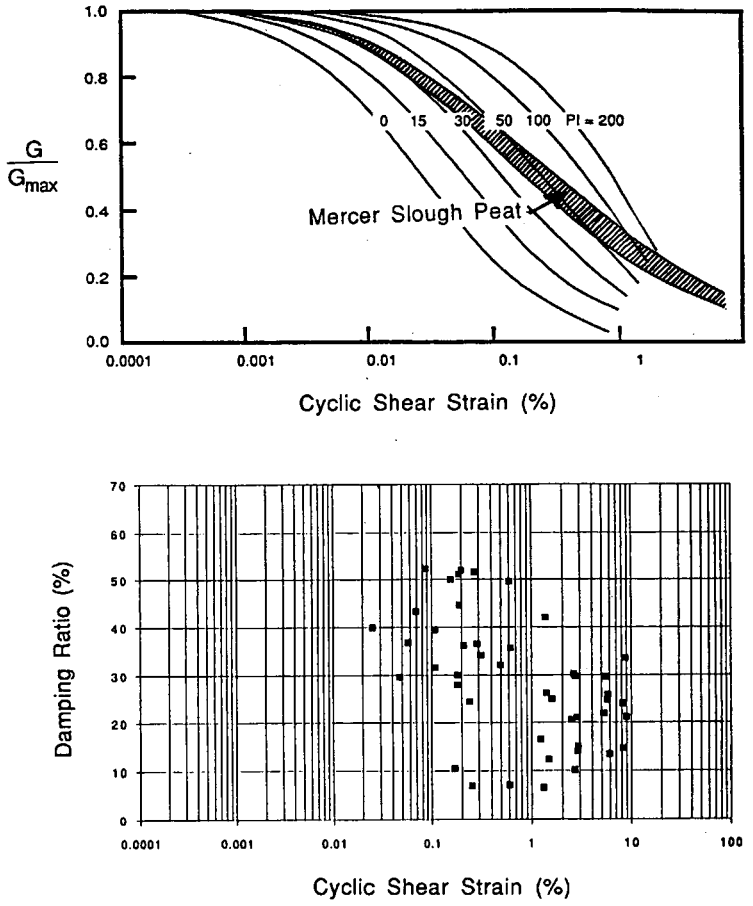

FIGURE 5 Measured dynamic properties of Mercer Slough peat: (*top*) normalized shear modulus and (*bottom*) damping ratio.

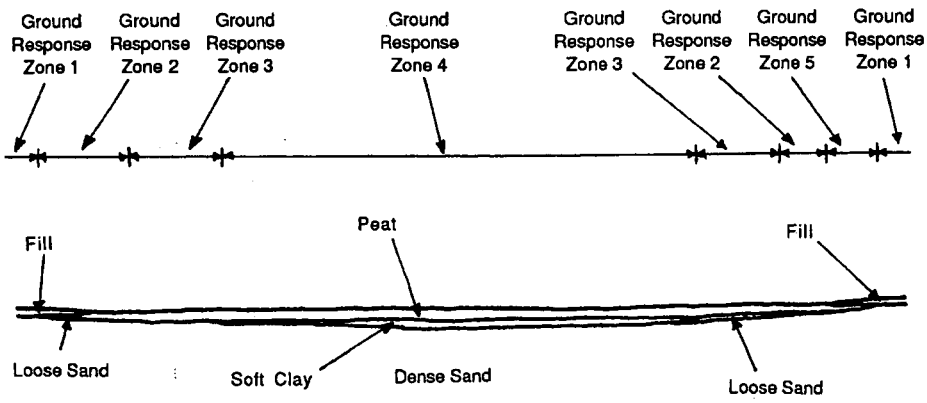

FIGURE 6 Location of ground-response zones (identical vertical and horizontal scales).

TABLE 1 Soil Profiles Used in Ground-Response Analyses

	Thickness of Layer in ft (m)				
Layer	Zone 1	Zone 2	Zone 3	Zone 4	Zone 5
Fill	23 (7.0)	0	0	0	8 (2.4)
Peat	0	30 (9.1)	44 (13.4)	60 (18.3)	11 (3.4)
Soft Clay	0	0	0	43 (13.1)	0
Loose Sand	0	0	11 (3.4)	0	0
Glacial Till	977 (298)	970 (296)	945 (288)	897 (273)	981 (299)

corporated in the computer program SHAKE (*21*). The input motions, applied at the bedrock-till interface, induced significant strains in the very soft Mercer Slough peat. The ground-response analyses predicted the following peak ground surface accelerations:

Zone	*Avg Peak Ground Surface Acceleration (g)*
1	0.16
2	0.12
3	0.12
4	0.08
5	0.12

The average computed peak accelerations for all ground-response zones were lower than the peak bedrock acceleration. For ground-response Zones 2 through 5, which contained varying thicknesses of Mercer Slough peat, the peak ground surface accelerations were considerably lower than the peak bedrock acceleration, illustrating the deamplifying effect of the very soft peat. The effects of the peat were also reflected in the frequency content of the computed ground surface motions. Examination of the time histories of ground motion further illustrates the influence of the thick peat layer on ground surface motions. Figure 7 shows time histories of acceleration, velocity, and displacement computed for ground-response Zone 3 in response to the scaled El Centro input motion. Though the computed peak ground surface acceleration is only 0.2 g, it occurs at a very low frequency and consequently produces very large displacements. The maximum computed relative displacements between the ground surface and the top of the glacial till are as follows (1 ft = 0.3 m):

Zone	*Maximum Relative Displacement (ft)*
1	0.01
2	0.95
3	4.04
4	3.73
5	0.58

These maximum relative displacements were generally produced when the displacements of the ground surface and the top of the glacial till were out of phase. As indicated by the tabulation above, the maximum relative displacement was

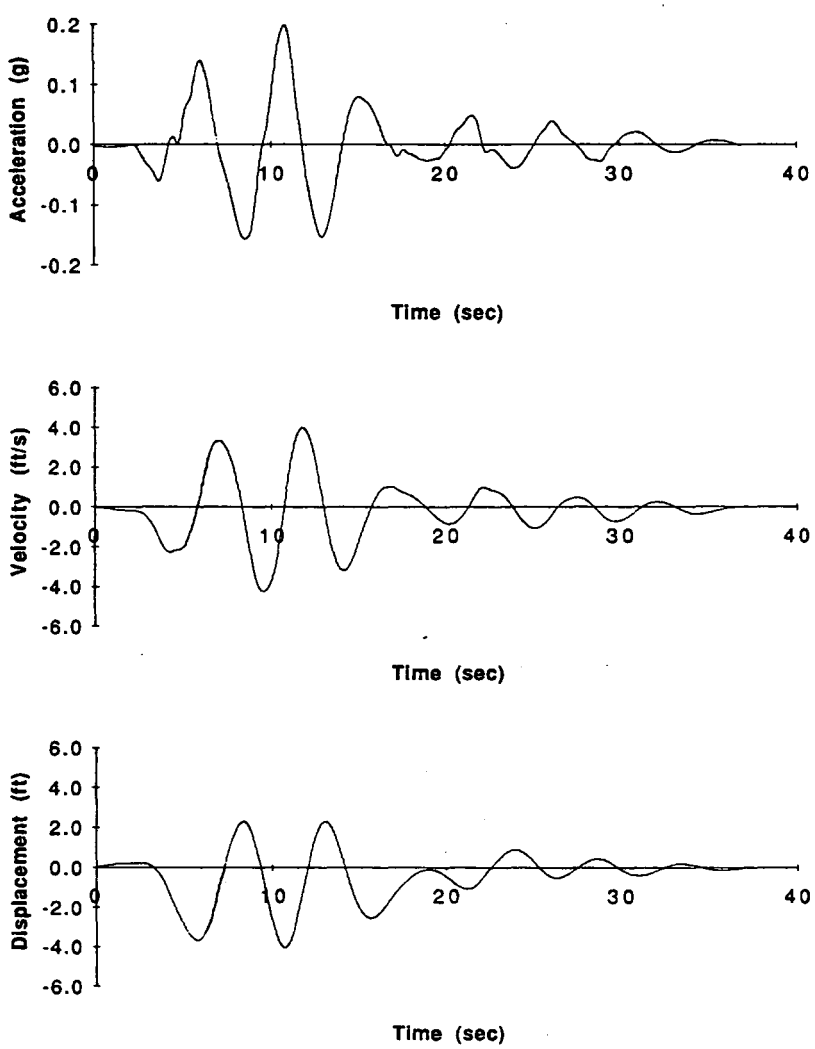

FIGURE 7 Computed time histories of acceleration, velocity, and displacement for ground-response Zone 3 (scaled El Centro input motion).

very small for ground-response Zone 1, which contained no peat, and very large for the other ground-response zones.

Average, normalized ground surface response spectra for each of the five ground-response zones are shown, along with the Applied Technology Council standard design response spectra (*9,22*), in Figure 8. Although the standard design spectra adequately describe the computed response for ground-response Zone 1, which contained no peat, they are not consistent with the computed response of the ground-response zones that did contain peat.

Free-field soil profile curvatures were computed for ground-response Zones 2 and 3. In both cases, the time at which the maximum soil profile curvature occurred did not coincide with the time at which the maximum relative displacement occurred. The soil curvature profiles at the time of maximum soil curvature are shown in Figure 9. In both cases, the peak computed curvature occurred at the bottom of the peat layer, where the computed impedance ratios were 16 and 11 for ground-response Zones 2 and 3, respectively. These impedance ratios were much larger than those from the San Francisco Bay area sites analyzed by Margason and Holloway (*8*) and Banerjee et al. (*10*). As a result, the maximum computed soil profile curvatures were also very large: 14.5×10^{-4} in.$^{-1}$ (5.7×10^{-4} cm^{-1}) for ground-response Zone 2 and 150×10^{-4} in.$^{-1}$ (59×10^{-4} cm^{-1}) for ground-response Zone 3. These soil curvatures correspond to radii of curvature of 57 ft (17.5 m) for ground-response Zone 2 and 5.5 ft (1.7 m) for ground-response Zone 3. These extraordinarily large computed curvatures resulted from the unusually low stiffness and density of the Mercer Slough peat.

SOIL-PILE INTERACTION

The existence of locally high curvatures suggests that the free-field soil displacement profile exhibits "kinks" at the depths corresponding to high curvature, as shown in Figure 9. The assumption that the concrete-filled steel pipe piles and timber piles supporting the I-90 bridges will move with the soil and assume the same kinked shape is clearly inappropriate, particularly in light of the very low stiffness and strength of the Mercer Slough peat.

Method of Analysis

To estimate the curvature demand on the piles, approximate soil-pile interaction analyses were performed using a three-dimensional finite element model of a column of soil containing a pile. The meshes used in the analyses are shown in Figure 10. To minimize potential boundary effects, all boundaries were located at least 10 pile diameters from the center of the pile. The analyses were performed in the following manner:

1. With the pile elements assigned the same properties as the surrounding soil at the same depth, the finite element mesh was deformed such that the lateral displacements of the nodal points along the centerline of the pile were equal to the computed free-field soil profile displacements at the time of maximum soil profile curvature (Figure 9).
2. The nodal point forces required to deform the mesh into this configuration were computed and stored.

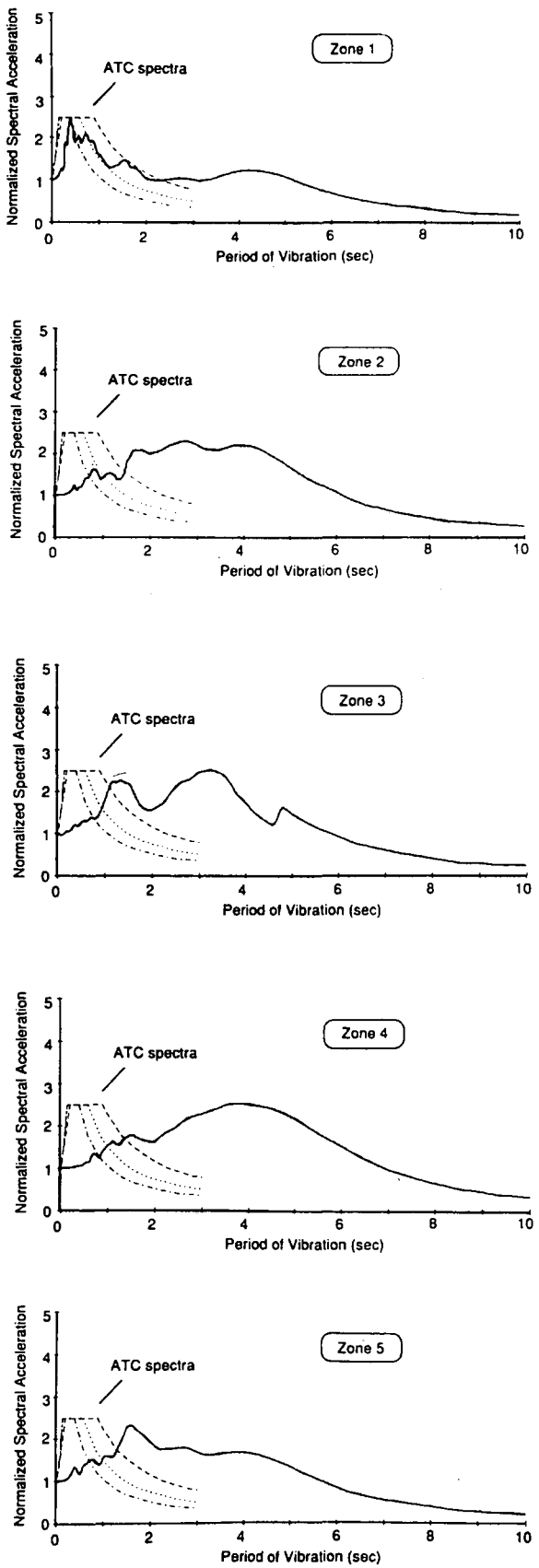

FIGURE 8 Computed normalized response spectra for ground-response Zones 1 through 5.

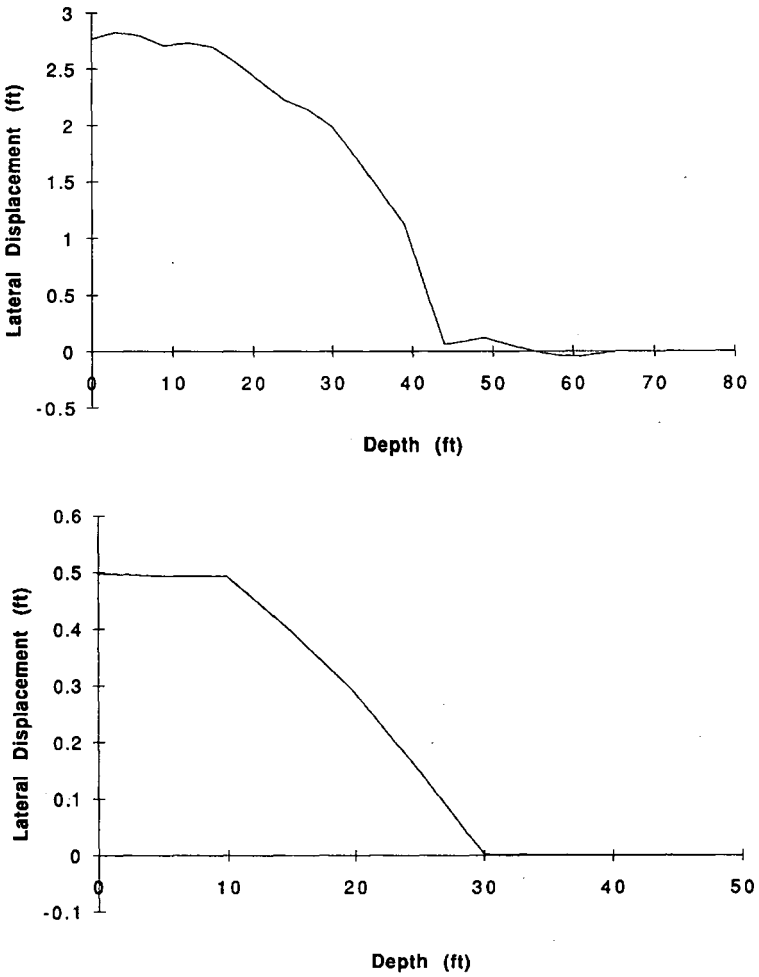

FIGURE 9 Computed free-field soil displacement profiles at time of maximum curvature: (*top*) ground-response Zone 2 and (*bottom*) ground-response Zone 3.

3. The pile elements were then assigned properties that produced the flexural stiffnesses of the various piles being considered.

4. The modified finite element model was subjected to the nodal point forces computed in Step 2. The resulting lateral displacements of the nodal points along the centerline of the pile were then used to compute the curvature demand on the piles.

Assumptions and Justification

This approximate method of interaction analysis involved a number of simplifying assumptions. First, the interaction analysis was static, not dynamic. Second, inertial forces at the pile heads resulting from the mass of the superstructure were not modeled. Third, the P-D effect associated with large lateral deflections was not modeled.

Though the interaction analysis itself was performed statically, the displacements imposed on the piles were obtained by dynamic analysis. At the time of maximum curvature for each ground-response zone, accelerations were small, particularly at the depth of maximum curvature; consequently the error involved in the static interaction analysis was assumed to be small. Because accelerations were low, inertial forces at the pile head were not large, and those that would develop would be resisted by the soil near the ground surface rather than the soil at the depth of maximum curvature; consequently, the error associated with neglecting these inertial forces was assumed to be small. Because the vertical loads were relatively small, bending moments due to the P-D effect were estimated to be much smaller than those caused by seismically induced curvature of the surrounding soil profile.

Results

The approximate interaction analyses indicated that the curvatures induced in the piles would be considerably lower than the free-field soil profile curvatures. The influence of the flexural stiffness of the piles is most easily illustrated by comparing the deflected shape of the piles and the free-field soil profile at the times of maximum curvature, as shown in Figure 11, in which it may be seen that the flexural stiffness of the piles allows the kink in the free-field soil profile to be bridged with considerably smaller pile curvatures. The reduction in maximum curvature for the various types of pile is shown in Table 2. Obviously, the maximum computed pile curvatures are considerably smaller than the maximum computed free-field soil profile curvatures. The curvature reduction clearly

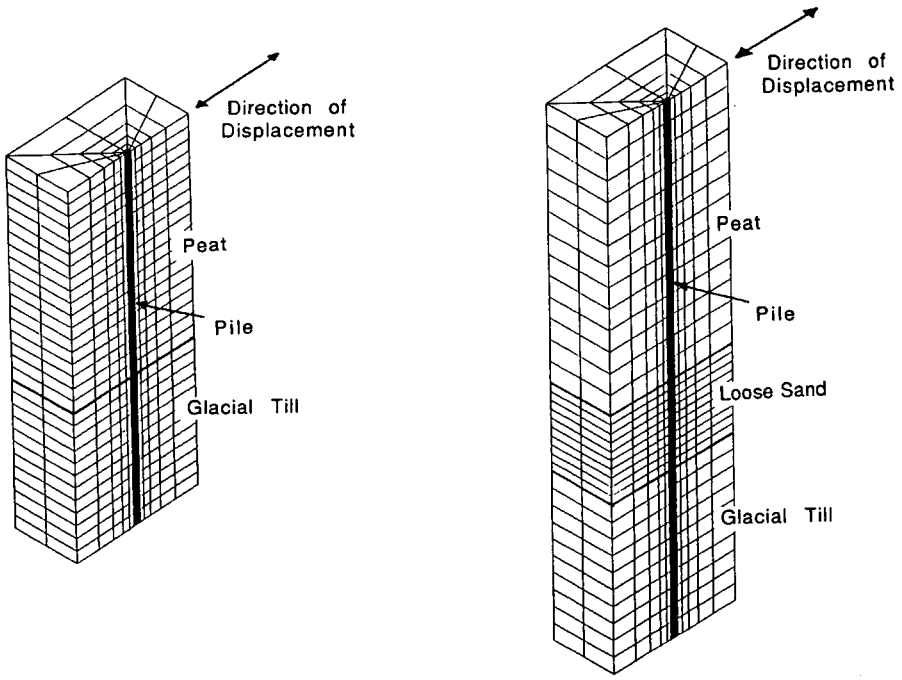

FIGURE 10 Finite element meshes used in approximate soil-pile interaction analyses: (*left*) ground-response Zone 2 and (*right*) ground-response Zone 3.

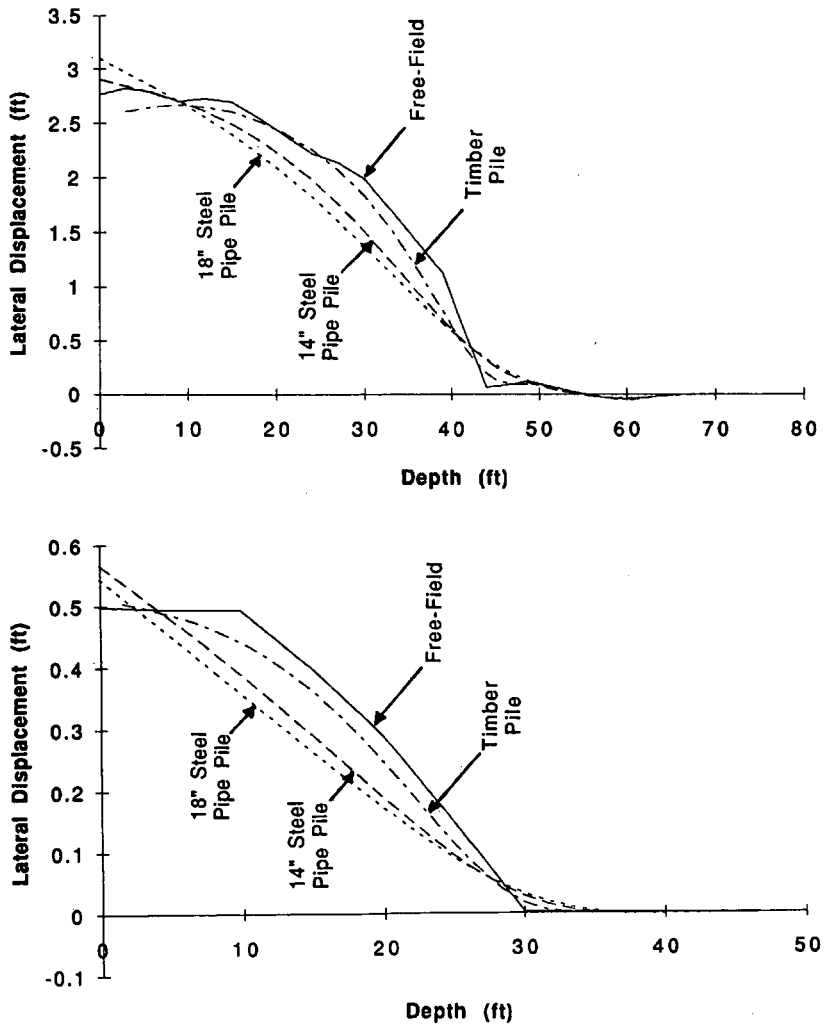

FIGURE 11 Computed pile and free-field soil displacement profiles: (*top*) ground-response Zone 2 and (*bottom*) ground-response Zone 3.

TABLE 2 Maximum Computed Pile and Free-Field Soil Curvatures

	Ground Response Zone 2			Ground Response Zone 3		
	14" Pipe	18" Pipe	Timber	14" Pipe	18" Pipe	Timber
$\phi_{max,pile}$	1.5 (0.59)	1.1 (0.45)	3.6 (1.40)	29.2 (11.5)	25.7 (10.1)	42.4 (16.7)
$\phi_{max,soil}$	14.5 (5.7)	14.5 (5.7)	14.5 (5.7)	150 (59)	150 (59)	150 (59)
$\frac{\phi_{max\ pile}}{\phi_{max\ soil}}$	0.103	0.079	0.246	0.195	0.171	0.283

Note: Values are in $in^{-1} \times 10^{-4}$ ($cm^{-1} \times 10^{-4}$).

varies with the flexural stiffness of the pile; greater curvature reduction is associated with greater flexural stiffness. However, the computed pile curvatures are still very large. Analysis of the influence of such large curvatures on the structural integrity of the piles is currently under way.

SUMMARY AND CONCLUSIONS

Ground-response and approximate soil-pile interaction analyses were performed to estimate the curvature demand on existing piles supporting bridges that cross a peat-filled slough. The ground-response analyses indicated that large strains would be induced in the peat near its interface with the underlying soil and that these large strains would produce large, localized curvature in the soil displacement profile. The approximate soil-pile interaction analysis indicated that the maximum pile curvatures would be considerably smaller than the maximum soil profile curvatures, but that they would still be very large.

ACKNOWLEDGMENTS

The research described in this paper was supported by the Washington State Department of Transportation and the National Science Foundation. Graduate and undergraduate students Fan-Yie von Laun, N. Sivaneswaran, Jun Xu, Jerry Wu, Peter Sajer, Terry Martin, and Kuan Sian Go assisted in various field testing, laboratory testing, and analytical aspects of the research.

REFERENCES

1. Matlock, H., and L. C. Reese. Generalized Solution for Laterally Loaded Piles. *Journal of the Soil Mechanics and Foundations Division,* ASCE, Vol. 86, No. SM5, 1960, pp. 63–91.
2. Matlock, H. Correlations for Design of Laterally Loaded Pile in Soft Clays. Paper OTC 1204. *Second Annual Offshore Technology Conference,* Houston, Texas, 1970, Vol. 1, pp. 577–594.
3. Nogami, T., and M. Novak. Resistance of Soil to a Horizontally Vibrating Pile. *Journal of Earthquake Engineering and Structural Dynamics,* Vol. 5, 1977, pp. 249–261.
4. Blaney, G. W., and M. W. O'Neill. *Lateral Response of a Single Pile in Overconsolidated Clay to Relatively Low-Frequency Pile-Head Loads and Harmonic Ground Surface Loads.* Research Report UHCE 83-19. Department of Civil Engineering, University of Houston, Houston, Texas, 1983.
5. Kachedoorian, R. *Effects of Earthquake of March 27, 1964 on the Alaska Highway System.* Professional Paper 545-C. U.S. Geological Survey, Department of Interior, Washington, D.C., 1968.
6. Elliot, A. L., and I. Nagai. Earthquake Damage to Freeway Bridges. In *San Fernando, California Eathquake of February 9, 1971,* Vol. 2, National Oceanic and Atmospheric Administration, U.S. Department of Commerce, 1973.
7. Hideaki, K. Damage of Reinforced Precast Piles During the Miyagi-Ken-Oki Earthquake of June 12, 1972. *Proc., 7th World Conference on Earthquake Engineering,* Vol. 9, Istanbul, Turkey, 1980.
8. Margason, E., and D. M. Holloway. Pile Bending During Earthquakes. *Proc., 6th World Conference on Earthquake Engineering,* Vol. 4, New Delhi, India, 1977.
9. *Tentative Provisions for the Development of Seismic Regulations for Buildings.* Report ATC-3-06. Applied Technology Council, Redwood City, Calif., 1984, 599 pp.
10. Banerjee, S., J. F. Stanton, and N. M. Hawkins. Seismic Performance of Precast Prestressed Concrete Piles. *Journal of Structural Engineering,* ASCE, Vol. 113, No. 2, 1987, pp. 381–396.
11. Heaton, T. H., and H. Kanamori. Seismic Potential Associated with Subduction in the Northwestern United States. *Bulletin of the Seismological Society of America,* Vol. 74, No. 3, 1984, pp. 933–941.
12. Atwater, B. F. Evidence for Great Holocene Earthquakes Along the Outer Coast of Washington State. *Science,* Vol. 236, No. 4804, 1987, pp. 942–944.
13. Newman, D. E. *A 13,500 Year Pollen Record from Mercer Slough, King County, Washington.* M.S. thesis. Department of Geological Sciences, University of Washington, Seattle, 1983.
14. Galster, R. W., and W. T. Laprade. Geology of Seattle, Washington, United States of America. *Bulletin of the Association of Engineering Geologists,* Vol. 28, No. 3, 1991, pp. 235–302.
15. Kramer, S. L., R. Satari, and A. P. Kilian. Evaluation of In Situ Strength of a Peat Deposit from Laterally Loaded Pile Test Results. In *Transportation Research Record 1278,* TRB, National Research Council, Washington, D.C., 1990, pp. 103–109.
16. Kramer, S. L. *Behavior of Piles in Full-Scale, Field Lateral Loading Tests.* Washington State Transportation Center, Seattle, Oct. 1991, 79 pp.
17. *Thomson Way Crossing of Union Bay, Seattle, Washington.* Foundation Engineering Report Technical Supplement, Shannon & Wilson, Nov. 1967, 108 pp.
18. Seed, H. B., and I. M. Idriss. Analyses of Ground Motions at Union Bay, Seattle During Earthquakes and Distant Nuclear Blasts, *Bulletin of the Seismological Society of America,* Vol. 60, No. 1, 1970, pp. 125–136.
19. Vucetic, M., and R. Dobry. Effect of Soil Plasticity on Cyclic Response. *Journal of Geotechnical Engineering,* ASCE, Vol. 117, No. 1, 1991, pp. 89–107.
20. Idriss, I. M., and H. B. See. Seismic Response of Soil Deposits. *Journal of the Soil Mechanics and Foundations Division,* ASCE, Vol. 96, 1970.
21. Schnabel, P. B., J. Lysmer, and H. B. Seed. SHAKE: A Computer Program for Earthquake Response Analysis of Horizontally Layered Sites. Report EERC 72-12. Earthquake Engineering Research Center, University of California, Berkeley, Dec. 1972, 88 pp.
22. *Seismic Design Guidelines for Highway Bridges.* Report ATC-6. Applied Technology Council, Redwood City, Calif., 1986, 204 pp.

Publication of this paper sponsored by Committee on Engineering Geology.

Characterizing Fault Rupture Hazards for Design of Buried Pipelines

JEFFREY R. KEATON

Location of buried pipelines may not be able to avoid fault traces that have the potential to rupture the ground surface. For detailed hazard analysis, geologic evaluation must be done to determine the age and recurrence intervals of surface faulting events. These data, along with the proximity to population as an index of public risk, are used to identify those faults that require pipeline treatment for design. Detailed geologic evaluation also allows characterization of fault movement for pipeline stress analyses. The type of fault, orientation of the fault with respect to the pipeline, direction of movement, and amount of movement must be quantified for stress analyses. The design procedure is iterative and can be done with an analytical or a finite-element method. Variable parameters in the design are unanchored length, pipeline-fault intersection angle, ditch geometry, backfill material properties, pipe material, and pipe coating.

Linear facilities, such as canals and pipelines, cannot be located to avoid all linear geologic features, such as rivers and faults. Active processes associated with unavoidable linear geologic features must be characterized to provide a basis to (*a*) reduce the risk of damage to the facility, which could result in a threat to public safety; (*b*) reduce the owner's exposure to loss of facility function; and (*c*) comply with mitigation measures required by federal, state, or local agencies, such as the Federal Energy Regulatory Commission (FERC).

Design of buried pipelines exposed to surface fault rupture hazards is discussed. Faults in the vicinity of pipeline alignments must be evaluated to identify potentially hazardous movements. Fault movement parameters must be defined for those considered hazardous. The parameters provide the geologic basis for an iterative design process that allows adjustment of several variables so that stresses, strains, and deformations remain within the allowable range. The procedure described in this paper can also be used for design of pipelines crossing sites that have similar potential ground movements, such as landslides and liquefaction zones.

HAZARDOUS FAULTS

A fault is a plane across which displacement of opposite sides has occurred parallel to the plane. A fault zone is a zone of such planes that may merge at depth into a single plane. Displacements across faults can be purely parallel to the strike of the plane (strike-slip faults), purely parallel to the dip of the plane (dip-slip faults), or a combination of the two directions (oblique-slip faults). Idealized slip alternatives are shown in Figure 1.

SHB AGRA, Inc., 4137 South 500 West, Salt Lake City, Utah 84123.

Hazardous faults are those faults that are "active" (*2*) or "capable" (*3*). An active fault is one along which movement will occur in the future. Sites that have had fault movement in the recent past may be more likely to have future movements than sites that have not had recent fault movements. The length of time appropriate to represent the recent past has been the subject of much discussion within the geologic community. State and local ordinances regulating development in areas with known fault traces commonly are based on the most recent 10,000 years of earth history (Holocene time). FERC defines capable faults as those that have moved at least once during the past 35,000 years (late Pleistocene time) or multiple times during the past 500,000 years (late Quaternary time). Thus, the degree of hazard may be expressed by the age of the most recent movement and the recurrence interval between movements. For example, faults can be distinguished on some maps by age of most recent movement, as indicated in Figure 2.

In some areas of less frequent earthquake activity, faults may appear to have been inactive for long periods but be oriented in such a way that they might be expected to move again under the current stress field. The orientations of faults and folds associated with simple shear in a strike-slip fault zone are shown in Figure 3. Thus, if a fault trace were identified in an area of interest but the geologic record needed to determine the age of most recent movement were missing, the potential for future activity could be based on its relationship to the stress field associated with the nearest known active fault.

Not all faults that were active during Quaternary time represent the same hazard in terms of frequency or amount of surface displacement (*1*,*6*). Therefore, not all Quaternary faults represent the same risk of damage to pipelines. Furthermore, although many pipelines pass through urban areas, most pipeline alignments that cross active faults are remote from populated areas. An approach has been developed for three categories of pipeline treatment at active fault crossings: full design treatment, contingency-planning treatment, and no treatment (*7*). This approach uses geologic factors to screen the faults crossed by pipelines and is based in part on proximity to populated areas, as discussed below.

Fault Evaluation Procedure

The first task in a fault evaluation is to examine published geologic maps and reports and inventory fault traces and ages of displaced deposits. In many cases, published geologic maps were made to show bedrock relationships, and Quaternary deposits and fault traces are generalized.

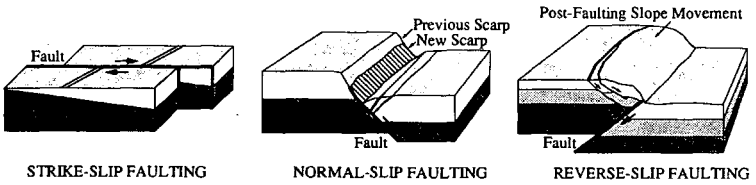

FIGURE 1 Idealized types of faults [modified from Slemmons (*1*)].

The second task is to examine aerial photographs for lineaments, particularly in deposits or across surfaces of Quaternary age. The most detailed photographs may not provide adequate information because they may cover only a limited area along a project. For example, photographs taken specifically for a pipeline project are usually oriented along a single flight line parallel to the project and often do not extend far enough from the alignment to be useful for fault evaluation. A pipeline alignment may cross a fault in an area where the fault is concealed by very young deposits, and photographs taken along the strike of the fault or with multiple flight lines may be needed for fault evaluation. Consequently, aerial photograph coverage may be supplemented with photographs from available federal agency collections (Soil Conservation Service and Forest Service, U.S. Department of Agriculture, and Bureau of Land Management and Geological Survey, U.S. Department of the Interior). Photographs taken at several times of the year may be useful for vegetation contrasts that may be present along fault traces. One of the most useful scales for fault evaluation is 1:12,000 because a reasonable area is visible in a single view at reasonable detail. A standard 9-in. (22.9-cm) contact print covers an area of 9,000 ft (2.74 km by 2.74 km) and can be viewed at a scale of about 1:2,400 with a conventional stereoscope with 5-power magnification.

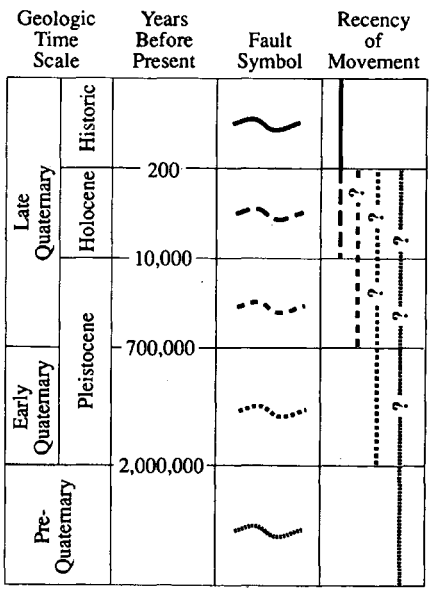

FIGURE 2 Distinction of faults by age of most recent movement [modified from Jennings (*4*)].

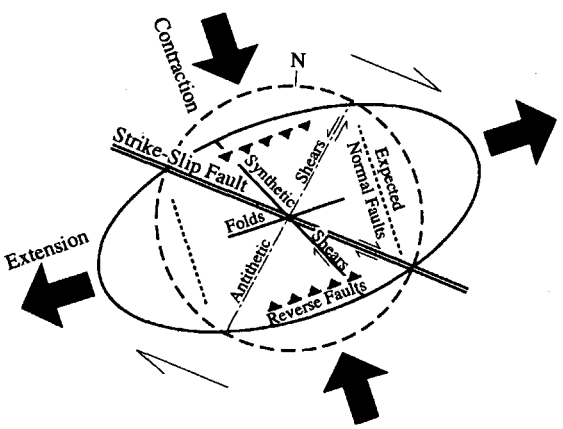

FIGURE 3 Orientations of faults and folds associated with simple shear in a strike-slip fault zone [modified from Keller (*5*)].

The third task is aerial reconnaissance of the project area and faults and lineaments previously identified. Aerial reconnaissance during low-sun-angle illumination enhances shadows cast by scarps facing away from the sun and bright lineaments caused by reflectance from scarps facing toward the sun. The shadow and highlight enhancement can be particularly valuable for identifying subtle or low scarps in young sediments along Quaternary faults. It may be useful for selected segments of a project and possible fault-related features to be photographed at a scale of about 1:12,000 under low-sun-angle lighting.

Following examination of the low-sun-angle photographs, the fourth task is detailed field mapping of locations most promising to yield data regarding (*a*) whether lineaments are actually faults, (*b*) the age of most recent activity, and (*c*) likely recurrence intervals between surface faulting events.

The fifth task is preparation of a summary fault characterization listing

1. Fault type (strike-slip, normal-slip, reverse-slip),
2. Orientation with respect to the pipeline (angles of intersection are referenced to the pipeline as viewed in a downstream direction; positive angles are to the right and negative angles are to the left of the pipeline axis),
3. Direction of movement (such as right-lateral, down-to-the-southwest, up-from-the-north),
4. Probable age of most recent movement (estimated in years, such as >10,000 years), and
5. Amount of movement per fault rupture event (estimated in feet or meters).

Fault type, orientation with respect to the pipeline, and direction of movement are straightforward parameters that

require no further explanation. The probable age of most recent movement and recurrence intervals can be estimated from geologic relationships involving the youngest faulted material and the oldest unfaulted material. The degradation of fault scarps in alluvial deposits can be used to estimate the age of the most recent movement, and the shape of the scarp can be used to estimate the number of surface faulting events responsible for creating the scarp (*8*).

The amount of fault movement per event can often be determined from the height of scarps in young sediments or the distance stream channels have been offset. Scarps in very young sediments may record only one surface faulting event; therefore, the height of the scarp may be a reasonable estimate of the amount of fault movement expected during the next event. The scarp along the entire length of a fault trace should be examined to determine the maximum single-event scarp height, which is the height that should be used for design (*9*). Subsurface investigations often provide the best information regarding the vertical component of displacement in past fault rupture events. Geomorphic evidence of lateral slip along faults, such as offset stream channels, often provides the best estimate of the amount of movement; estimating the age of such movement can be particularly challenging. Maximum displacements may be estimated on the basis of field data and relationships between fault rupture length and earthquake magnitude displacement (*10,11*).

Proximity to Populated Areas

For some projects, public risk exposure may be an important issue. The population classifications of the U.S. Department of Transportation (DOT) (*12*) for natural gas pipelines are based on the distance from pipelines to number of buildings within certain areas. The DOT classification is summarized in Table 1.

Fault Crossing Philosophy

A philosophy for design of pipelines crossing active fault traces is illustrated in Figure 4. This philosophy was developed for the Kern River pipeline project, which extends from southwestern Wyoming to southern California and crosses the seismically active Basin and Range Province with its numerous Quaternary faults (*13*). Three design treatment options were considered: no treatment, operational treatment, and full treatment. No treatment was considered necessary for the design of the pipeline where it crossed faults that seemed to pose little risk to the project and were relatively remote from populated areas. Operational treatment consisted of a contingency plan for rapid repair of the pipeline where it crossed faults that seemed to pose some risk to the project but were relatively remote from populated areas. Full treatment consisted of controlling six variables, discussed later in the section headed Summary of Design Procedure, where the pipeline crossed hazardous faults in relatively close proximity to populated areas.

TABLE 1 U.S. Department of Transportation Population Classifications for Areas Crossed by Natural Gas Pipelines [adapted from DOT pipeline safety regulations (*12*)]

DOT Population Classification	Number of buildings within 200 m on either side of the centerline of any 1.61-km length of pipeline
1	0 to 10
2	11 to 45
3	46 or more, or within 100 m of a place occupied by 20 or more persons on at least 5 days per week, 10 weeks per year
4	Class 1, 2, or 3 where buildings of 4 or more stories are prevalent

FAULT RUPTURE DESIGN PARAMETERS

If fault rupture must be included in pipeline design, it must be described in a way that can be used to compute stresses, strains, and deformations in the pipe material. Fault rupture design parameters are (*a*) fault orientation, (*b*) direction of movement, and (*c*) amount of movement. The orientations of fault traces can usually be determined from observation of scarps and other surface features created by past faulting events. The dip of the fault plane may be somewhat more difficult to determine from surface observations. The direction of movement should be clear from the surface expression and the seismotectonic setting. For example, northwest-trending faults in southern California are right-lateral strike-slip faults, and north-trending faults in Nevada and Utah are normal faults. Subsurface investigations may be needed to locate the fault at the pipeline crossing; however, the amount of movement visible in a trench exposure may be less than the maximum displacement, which is the value that should be used in calculating stress and strain.

Logs of trenches excavated across a normal fault and a strike-slip fault are shown in Figures 5 and 6, respectively. The Granger fault, part of the West Valley fault zone near Salt Lake City, is a north-trending normal fault with no lateral component to the movement; therefore the vertical displacements of layers visible in a trench (Figure 5) represent the true character of the fault movement. Important aspects of the fault shown in Figure 5 are that it is relatively narrow (less than 1 m wide) and movement has occurred repeatedly along the same plane. The average displacement per event at the Granger fault is estimated to be about 1.5 m (*14*), yet the displacement of the Bonneville alloformation in Figure 5 is greater than 4.3 m, suggesting that at least three surface faulting events occurred in post-Bonneville time (the past 12,000 years). The Coyote Creek fault, near Anza Borrego State Park in southern California, is a northwest-trending strike-slip fault with little vertical component to the displacement; therefore the vertical displacements of layers visible in a trench (Figure 6) do not represent the true character of fault movement. In fact, the displacements of layers are apparent vertical separation due to lateral displacement of gently inclined beds. Important aspects of the fault shown in Figure 6 are that it is relatively narrow (less than 1 m wide) and movement has occurred repeatedly along the same plane. The vertical dis-

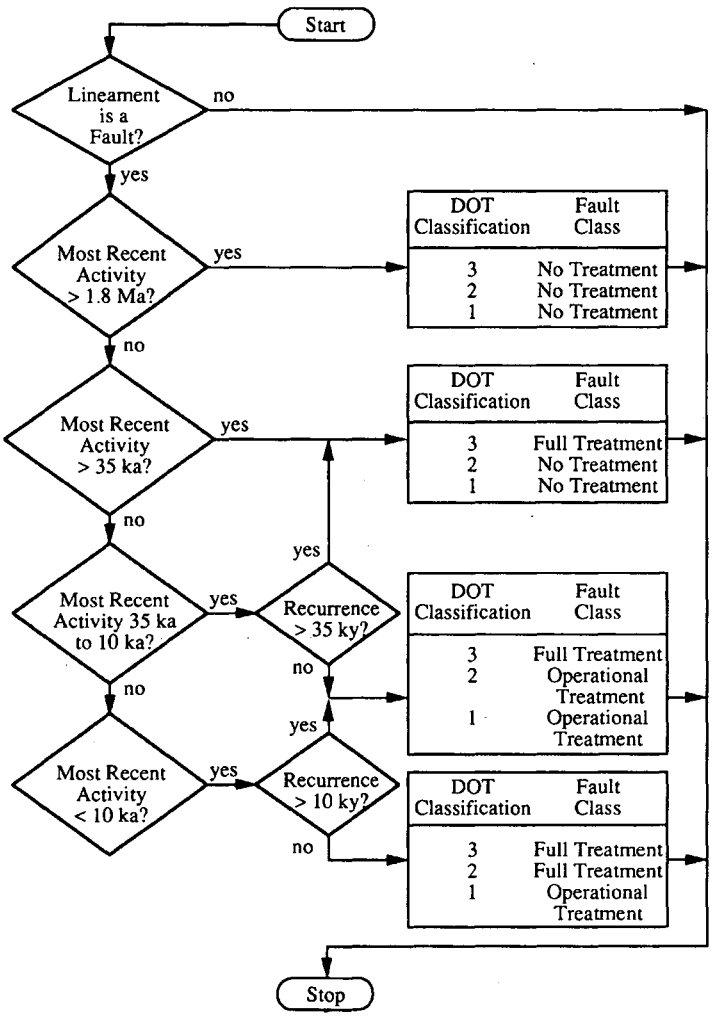

FIGURE 4 Flow diagram for treatment of the Kern River pipeline at active fault crossings [modified from Keaton et al. 1991 (*7*)].

placement values shown in Figure 6 indicate a slip rate of about 0.6 m per 1,000 years; however, the slip rate based on lateral offset of geomorphic features is about 3 m per 1,000 years (*15*).

The most reliable method of estimating the amount of fault rupture movement for use in stress analyses is direct observation of displaced features of known age. An alternative method of estimating maximum displacements associated with future fault rupture is statistical analyses of displacements cause by historic earthquakes, such as those by Bonilla et al. (*11*) and by Slemmons et al. (*10*). However, improper use of regression equations can result from careless application of statistical analyses (*16*). Since fault displacement is needed for stress analyses, displacement is the dependent variable. The appropriate independent variable would be fault length if it is estimated from published geologic maps or reconnais-

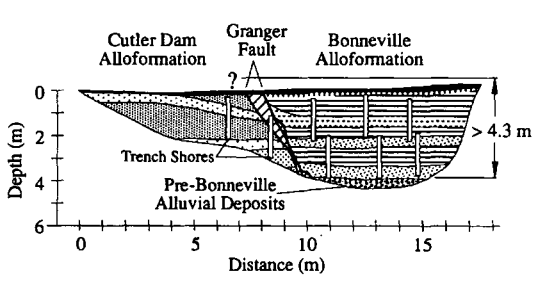

FIGURE 5 Log of trench across the West Valley fault [modified from Keaton et al. 1987 (*14*)].

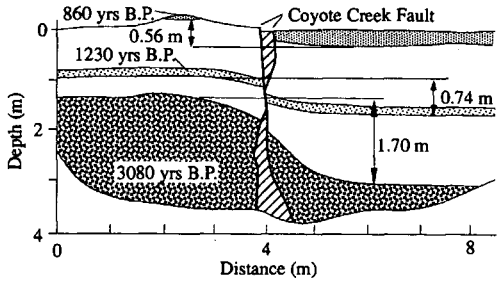

FIGURE 6 Log of trench across the Coyote Creek fault. [modified from Clark et al. (*15*)].

sance mapping. However, improper use of the regression equations results if earthquake magnitude is predicted from fault length and displacement is then predicted from earthquake magnitude.

As an example of fault displacement parameters, the values used in the design of the Kern River pipeline at its crossing of the Calico fault, the Antelope fault, and the Wasatch fault are presented in Figures 7, 8, and 9, respectively. The Calico fault is a northwest-trending, right-lateral strike-slip fault in the Mojave Desert of southern California. The Kern River pipeline crosses the Calico fault on gently sloping ground at an angle of +68 degrees. The Antelope fault is a north-northwest-trending, down-to-the-west normal fault in southwestern Utah. The Kern River pipeline crosses the fault on gently sloping ground at an angle of −50 degrees. The Wasatch fault is a north-trending, down-to-the-west normal fault in north-central Utah. The Kern River pipeline crosses the fault on steeply sloping ground at an angle of −45 degrees.

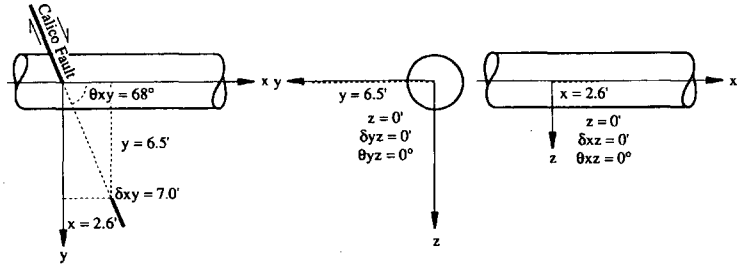

FIGURE 7 Design fault displacement parameters for the Calico fault crossing of the Kern River pipeline [modified from reports by Sergent, Hauskins & Beckwith (*17*)]. The reference coordinate system is oriented so that the positive *x*-direction is along the pipeline axis in the direction of increasing pipeline station numbers, the positive *z*-direction is perpendicular to the pipeline in a downward direction, and the positive *y*-direction extends to the right. *θxy*, *θyz*, and *θxz* are the angles between the fault plane and reference coordinate system axes in the respective planes. δ*xy*, δ*yz*, and δ*xz* are the displacement vectors in the respective planes. *x*, *y*, and *z* are the orthogonal components of displacement.

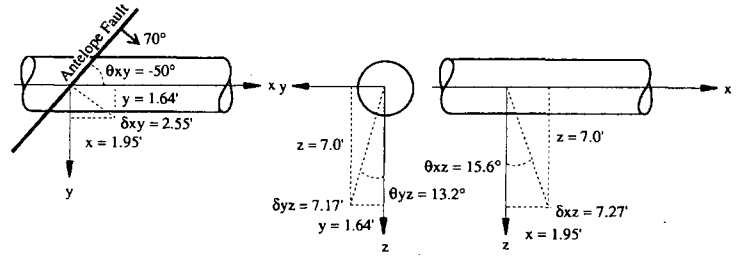

FIGURE 8 Design fault displacement parameters for the Antelope fault crossing of the Kern River pipeline [modified from reports by Sergent, Hauskins & Beckwith (*17*)]. See Figure 7 for explanation of coordinate system and symbols.

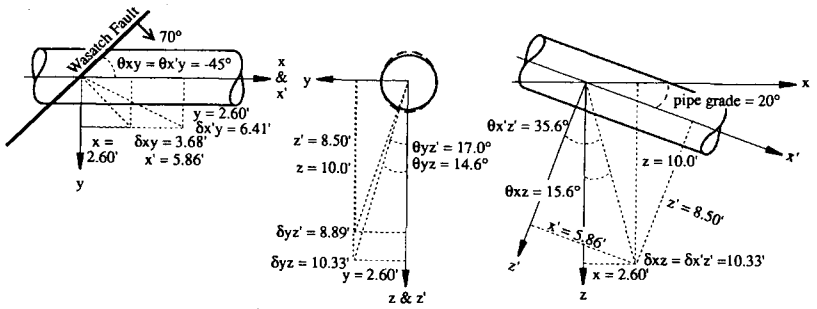

FIGURE 9 Design fault displacement parameters for the Wasatch fault crossing of the Kern River pipeline [modified from reports by Sergent, Hauskins & Beckwith (*17*)]. See Figure 7 for explanation of coordinate system and symbols.

Sloping ground and angle of crossing result in apparent lateral displacement due to normal-slip fault movement and apparent vertical displacement due to strike-slip fault movement.

SUMMARY OF DESIGN PROCEDURE

The following brief summary of the design procedure demonstrates the application of fault rupture parameters; the Kern River pipeline project is used as an example. An analytical method (*18*) and two finite-element methods [PIPLIN-PC (*19*) and B-SPLINE (*20*)] are in common usage. The pipeline design parameters are unanchored length, intersection angle, ditch geometry, backfill characteristics, pipe material, and pipe coating.

The unanchored pipeline length allows strain to be distributed. An unanchored length of 200 pipe diameters was used for the Kern River pipeline [approximately 180 m (600 ft) for the 91.4-cm (36-in.) diameter pipeline] on the basis of work by Newmark and Hall (*21*), Kennedy et al. (*18*), and Roe (*22*). Heavy-wall pipe [1.57 cm (0.618 in.) thick] made of API X-70 steel has favorable stress-strain characteristics and can accommodate substantial deformation while remaining anelastic. A soil-pipe friction angle of 14.3 degrees was estimated for the epoxy coating of the pipe (Shore D hardness of 84) on the basis of studies by O'Rourke et al. (*23*). Analytical procedures by Kennedy et al. (*18*) and the PIPLIN-PC finite element computer program (*19*) were used to perform soil-pipe interaction analyses to evaluate pipe stresses and strains for various backfill configurations to optimize the treatment. Medium-dense sand [ϕ = 35 degrees, γ = 18.85 kN/m^3 (120 lb/ft^3)] was specified for backfill around and beneath the pipe. Force-displacement relationships (*p-y* curves) (Figure 10) for the backfill were determined by procedures of Audibert and Nyman (*24*), Nyman (*25*), Trautmann et al. (*26*), and Trautmann and O'Rourke (*27*) for use in the analysis. The configuration of the ditch provides overexcavation of the bottom on the footwalls of normal faults and widening the sidewalls across the strike-slip faults, as shown in Figure 11. For the type and amount of fault movement assumed in the design, the analysis indicated that the ditch configuration would limit tensile strains in the pipe to less than 2 percent. The pipe was oriented at strike-slip and normal-slip fault crossings so that it will be in tension for the design fault displacements.

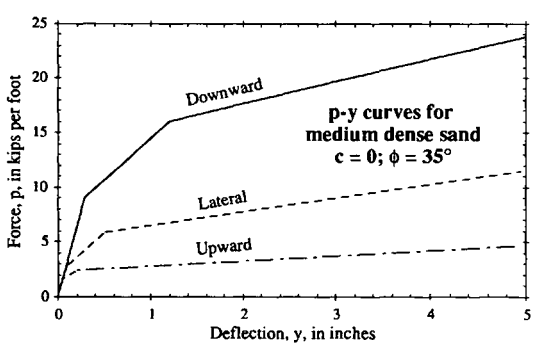

FIGURE 10 Load-deflection characteristics for medium-dense sand backfill [modified from reports by Sergent, Hauskins & Beckwith (*17*)].

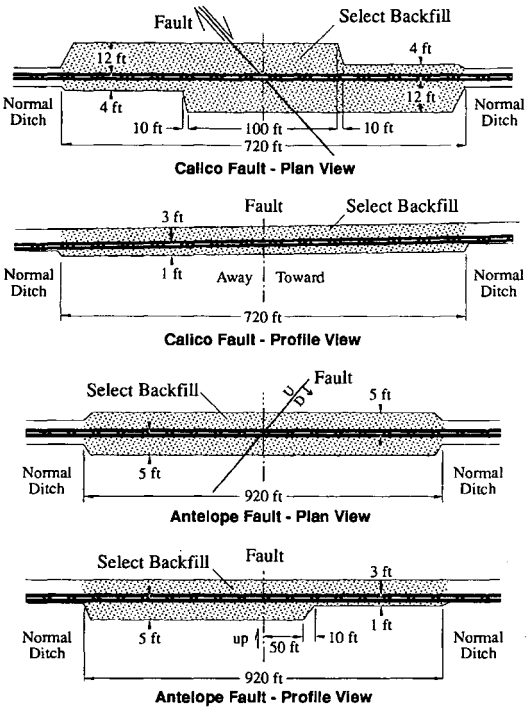

FIGURE 11 Construction ditch geometries for crossing active faults [modified from reports by Sergent, Hauskins & Beckwith (*17*)].

CONCLUSIONS

Hazardous faults can be identified and characterized with conventional detailed geologic studies. A risk-based philosophy for treatment of pipelines crossing active faults has been developed that appears to be conservative, particularly in remote (DOT classification 1) areas. Stress analyses using API X-70 steel, appropriate backfill *p-y* curve data, pipeline-fault geometry, and maximum fault offset amount from detailed geoseismic analyses allow one to determine the ditch dimensions needed to limit stresses and strains in the pipe. An analytical procedure (*18*) and a finite-element method (*19*) are commonly used in this context.

ACKNOWLEDGMENTS

Preparation of this paper was authorized by Frank E. Koscich, Kern River Gas Transmission Company, Salt Lake City. The author benefitted from discussions with Robert M. Robison, David B. Slemmons, and George H. Beckwith. The manuscript was improved as a result of comments from several anonymous reviewers.

REFERENCES

1. Slemmons, D. B. Faults and Earthquake Magnitude. In *State of the Art for Assessing Earthquake Hazards in the United States*, Report 6, Miscellaneous Paper S-73-1, U.S. Army Engineer Waterways Experiment Station, Vicksburg, Miss., 1977, 129 pp.
2. Slemmons, D. B., and R. McKinney. *Definition of "Active Fault"*.

Miscellaneous Paper S77-8. U.S. Army Corps of Engineer Waterways Experiment Station, Vicksburg, Miss., 1977.
3. Reiter, L. *Earthquake Hazard Analysis—Issues and Insights*. Columbia University Press, New York, 1990, 254 pp.
4. Jennings, C .W. *Preliminary Fault Activity Map of California*. Open-file Report 92-03. California Division of Mines and Geology, 1992.
5. Keller, E. A. Investigation of Active Tectonics: Use of Surficial Earth Processes. In *Active Tectonics*, National Academy Press, Washington, D.C., 1986, pp. 136–147.
6. Bonilla, M. G. *Evaluation of Potential Surface Faulting and Other Tectonic Deformation*. Open-file Report 82-732. U.S. Geological Survey, 1982, 88 pp.
7. Keaton, J. R., R. M. Robinson, G. H. Beckwith, and D. B. Slemmons. Philosophy for Treatment of High-Pressure Natural Gas Pipelines at Active Fault Crossings. In *Lifeline Earthquake Engineering* (M.D. Cassaro, ed.), Technical Council of Lifeline Earthquake Engineering Special Publication No. 4, American Society of Civil Engineers, 1991, pp. 898–906.
8. Wallace, R. E. Profiles and Ages of Young Fault Scarps, North-Central Nevada. *Geological Society of America Bulletin*, Vol. 88, 1977, pp. 1267–1281.
9. Machette, M. N. *Preliminary Assessment of Paleoseismicity at White Sands Missile Range, Southern New Mexico—Evidence for Recency of Faulting, Fault Segmentation, and Repeat Intervals for Major Earthquakes in the Region*. Open-file Report 87-444. U.S. Geological Survey, 1987, 46 pp.
10. Slemmons, D. B., P. Bodin, and X. Zhang. Determination of Earthquake Size from Surface Faulting Events. In *Proc., International Seminar on Seismic Zonation*, Guangzhou, China, 1989, pp. 157–169.
11. Bonilla, M. G., R. F. Mark, and J. J. Lienkaemper. Statistical Relations Among Earthquake Magnitude, Surface Rupture Length, and Surface Fault Displacement. *Bulletin of the Seismological Society of America*, Vol. 74, 1984, pp. 2379–2411.
12. *Pipeline Safety Regulations*. U.S. Department of Transportation, 1989. (*Code of Federal Regulations*, 1989, Title 49, Part 192, Subpart A, Section 192.5.)
13. Nakata, J. K., C. M. Wentworth, and M. N. Machette. *Quaternary Fault Map of the Basin and Range and Rio Grande Rift Provinces, Western United States*. Open-file Report 82-579. U.S. Geological Survey, 1982 (2 sheets).
14. Keaton, J. R., D. R. Currey, and S. J. Olig. *Paleoseismicity and Earthquake Hazards Evaluation of the West Valley Fault Zone, Salt Lake City Urban Area, Utah*. Final Technical Report. U.S. Geological Survey, Denver, 1987, 55 pp.
15. Clark, M. M., A. Grantz, and R. Meyer. *Holocene Activity of the Coyote Creek Fault as Recorded in the Sediments of Lake Cahuilla in the Borrego Mountain Earthquake of April 9, 1968*. Professional Paper 787, U.S. Geological Survey, 1972, pp. 112–130.
16. Williams, G. Improper Use of Regression Equations in Earth Sciences. *Geology*, Vol. 11, 1983, pp. 195–197.
17. Sergent, Hauskins & Beckwith. *Engineering Geology and Geotechnical Engineering Evaluations for Design of the Kern River Pipeline, Wyoming to California*. Federal Energy Regulatory Commission, Washington, D.C., 1990.
18. Kennedy, R. P., A. W. Chow, and R. A. Williamson. Fault Movement Effects of Buried Oil Pipelines. *Transportation Engineering Journal*, ASCE, Vol. 103, No. TE5, 1977, pp. 617–633.
19. *PIPLIN-PC (Version 3.11) Computer Program for Stress and Deformation Analysis of Pipelines*. SSD, Inc., Berkeley, Calif., 1990, 208 pp.
20. O'Rourke, T. D. *B-SPLINE Computer Program for Stress and Deformation Analysis of Pipelines*. Cornell University, Ithaca, N.Y., 1991.
21. Newmark, N. M., and W. J. Hall. Pipeline Design To Resist Large Fault Displacements. In *Proc., U.S. National Conference on Earthquake Engineering 1975*, Ann Arbor, Michigan, Earthquake Engineering Research Institute, 1975.
22. Roe, D. Computational Methods for Analysis of Response of Buried Pipelines to Soil Movements and Ground Distortion, Abatement of Seismic Hazards to Lifelines. In *Proceedings of a Workshop on Development of an Action Plan*, Vol. 5, Papers of Gas and Liquid Fuel Lifelines and Special Workshop Presentations, Federal Emergency Management Agency, Washington, D.C., FEMA 139, 1987.
23. O'Rourke, T. D., S. J. Druschel, and A. N. Netravali. Shear Strength Characteristics for Sand-Polymer Interfaces. *Journal of Geotechnical Engineering*, ASCE, Vol. 116, No. GT3, 1990, pp. 451–469.
24. Audibert, J. M. E., and K. J. Nyman. Soil Restraint Against the Horizontal Motion of Pipes. *Journal of Geotechnical Engineering*, ASCE, Vol. 103, No. GT10, Oct. 1977, pp. 1119–1142.
25. Nyman, K. J. Thaw Settlement Analysis for Buried Pipelines in Permafrost. *Pipelines in Adverse Environments*, American Society of Civil Engineers Specialty Conference, San Diego, Vol. 2, 1983, pp. 300–325.
26. Trautmann, C. H., T. D. O'Rourke, and F. H. Kulhawy. Uplift Force-Displacement Response of Buried Pipe. *Journal of Geotechnical Engineering*, ASCE, Vol. 111, No. GT9, 1985, pp. 1061–1076.
27. Trautmann, C. H., and T. D. O'Rourke. Lateral Force-Displacement Response of Buried Pipe. *Journal of Geotechnical Engineering*, ASCE, Vol. 111, No. GT9, 1985, pp. 1077–1092.

Publication of this paper sponsored by Committee on Engineering Geology.

Liquefaction-Induced Damage to Bridges

T. LESLIE YOUD

Liquefaction-induced lateral spread is a major cause of earthquake damage to bridges built across streams and rivers. Lateral spreads are characterized by horizontally displaced ground with extensional deformations at the head of the feature, shear deformations along the margins, and compressed ground at the toe. Displacements generally range from a few centimeters to several meters and are directed down mild slopes or toward a free face, such as an incised river channel. Such displacements thrust bridge abutments and piers riverward, generating large shear forces in connections and compressional forces in the superstructure. These forces have sheared connections, allowing decks to be thrust into, through, or over abutment walls or causing decks to buckle. In other instances, connections have remained intact with the deck acting as a strut, holding tops of piers and abutments in place while the bases of these elements are displaced toward the river. These actions have inflicted severe damage and even bridge collapse. The performance of bridges during past earthquakes is reviewed to illustrate types of damage as a consequence of liquefaction-induced ground displacement.

Liquefaction-induced ground failure is a major cause of earthquake damage to bridges. Bridges spanning rivers are particularly vulnerable to liquefaction because such structures commonly are founded on floodplain alluvium in areas with high groundwater levels. These conditions—recent deposition and high groundwater—are characteristics of sediments with high liquefaction susceptibility. Floodplain topography—including gentle slopes and incised river channels—is characteristic of areas susceptible to liquefaction-induced lateral spread.

Lateral spreads (Figure 1) are characterized by ground displacement down mild slopes or toward a free face, such as an incised channel. Lateral displacements may range from a few centimeters to several meters and are generated by a combination of gravitational and seismic forces. Bridge piers and abutments founded on a lateral spread are usually transported riverward with the spreading ground. Consequent differential displacements between foundation elements create severe stresses, deformations, or both within the bridge structure. To illustrate and categorize the types of damage inflicted by lateral spreads, several case histories of bridge damage are reviewed.

BRIDGE DAMAGE DURING PAST EARTHQUAKES

Hayward, California, 1868

One of the first instances of bridge damage caused by liquefaction-induced lateral spread in the United States apparently occurred during the 1868 Hayward, California, earthquake. Halley (*2*) noted the following: "The drawbridge on the line of the S.F. and O.R.R. was thrown out of place about eight inches [0.2 m], and as the locomotive and nearly all the cars were at San Antonio, no train left Oakland at 8 o'clock." This description is not very clear, but the type of damage—compression of the bridge structure—is typical of damage inflicted by lateral spread.

Charleston, South Carolina, 1886

The evidence is more explicit that liquefaction-induced lateral displacement damaged several bridges during the 1886 Charleston, South Carolina, earthquake. For example, Earle Sloan [quoted by Peters and Hermann (*3*)] penned the following cryptic notes concerning the Bacous bridge over the Ashley River: "[The damage] affords evidence of tendency of banks to approach centre of channel. Here expressed by compression of bridge causing one plank to overlap another seven inches [0.18 m] and jamming joints." The same investigator gave the following description of the railroad bridge over Rantowles Creek:

> Close inspection revealed fact that there had been a vibratory movement of sufficient energy to have caused entire [word missing] plastic earth with included piling on each side of "draw" to bodily approach channel of stream; the piling which affords no indication of relative movement from enclosing earth has dragged attached bents from vertical position and jerked superstructure from opposite sides to center line with a violence wrecking rails, bulging up stringers, forcing up caps of bents, mortised and spiled with 4 inch tenons, to top of latter, and in general affording liberal indications of shortening of distance separating the banks. Superstructure on both sides of "draw" was violent flexured both transversely and vertically with accumulated length of rail. Latter accumulation accounted for by near summit of involved grade where joints are liberally parted. (*3*)

These descriptions document lateral movements and the damage they caused. Ground displacements as great as several tenths of a meter shifted abutments and piers toward the centers of the channels, compressing bridge decks with attendant bulging up of stringers and overlapping of planks. Documented ground disturbances—including ground fissures and sand boils—confirm that liquefaction was widespread near these bridges.

San Francisco, California, 1906

Lateral spreads generated by the 1906 San Francisco earthquake damaged several bridges, including the highway bridge over the Salinas River south of Salinas, California (Figure 2).

Department of Civil Engineering, Brigham Young University, Provo, Utah 84602.

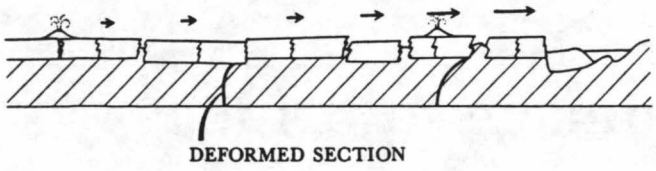

FIGURE 1 Diagram of a lateral spread showing liquefied layer, ground displacement, and disrupted ground surface [after National Research Council (*1*)].

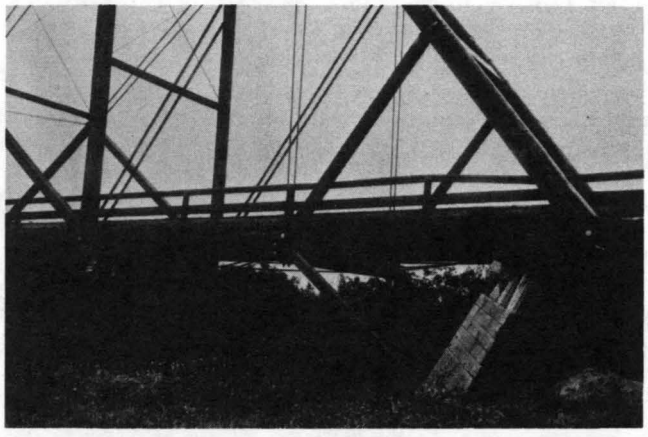

FIGURE 2 Highway bridge over Salinas River south of Salinas, California, that was damaged by lateral ground displacement during the 1906 San Francisco earthquake. The ground displacement physically moved the base of the southern pier 2.8 m toward the river (*photograph by J. C. Branner, courtesy of Stanford University Archives*).

Lateral displacement of the floodplain physically displaced both ground and pile foundation about 1.8 m northward toward the river channel. The bridge trusses and deck were strong enough to remain intact and were essentially undamaged. The deck, which remained attached to the tops of the piers, acted as a strut, holding the tops of the piers in place while their bases shifted riverward. This motion left the southern pier inclined, with the top of the pier tilted outward, away from the river.

Prince William Sound, Alaska, 1964

The most devastating earthquake damage to bridges in U.S. history occurred during the great Alaskan earthquake of 1964. Liquefaction and lateral spread damaged 266 railway and highway bridges, collapsing about 20 and damaging many others beyond repair. This destruction severely impaired the surface transportation system in southern Alaska for many months after the earthquake.

In nearly all instances, the Alaskan bridges were compressed as a consequence of lateral ground displacement. Those displacements inflicted different types of damage, depending on the amount of ground displacement, the strengths of various structural elements, and the orientation of the bridge relative to the river. The general types of damage are discussed in the following sections.

Railway Bridges

According to McCulloch and Bonilla (*4*), 125 railway bridges and 110 culverts were damaged or destroyed during the 1964 Alaska earthquake. None of those bridges collapsed, although many were irreparable and had to be replaced. The estimated cost to repair and replace these structures was about $2.5 million (1964 dollars). For comparison, the cost to regrade, repair, and realign railway embankments, which were also severely affected by ground failure and ground subsidence, was nearly $9 million. McCulloch and Bonilla recorded the following general description of ground displacements and consequent damage to railway bridges, most of which were timber structures:

> In all but six bridges, the net compression shown by interbent measurements exceeded the net extension. Net compression was generally 20 inches [0.50 m] or less, regardless of bridge length, but in two bridges compression was as large as 64 and 81.5 inches [1.62 and 2.07 m]. . . . In addition to having their supporting bents torn free, most stringers were put into compression by converging streambanks. Distances between streambanks were decreased by as much as 6.5 feet [2.0 m]. As a result, the stringers acted as struts, and either jammed into the fillers on the bulkheads or, where compression was greater, drove through the bulkhead planks. In some bridges most of the compression was released at one end, and the stringers were thrust up over the top of the bulkhead onto one of the approach fills. . . . Compressive forces not released by failures at the bulkheads produced lateral deflections in the decks of several bridges. Stringers were either thrown into long horizonal bends, or were broken at sharp kinks, with as much as 8 feet [2.4 m] of lateral deflection at the apex of the bends. (*4*)

The following examples of damaged railway bridges illustrate these effects. The damage to the bridge at Milepost 61.9 is representative of stringers thrust through bulkhead walls (Figure 3). This bridge consisted of seven 4.5-m long spans supported on interior timber pile bents with timber bulkheads at either end. About 0.5 m of streambank convergence compressed the bridge structure, tearing stringers from their seatings and thrusting the loosened stringers through the bulkhead walls.

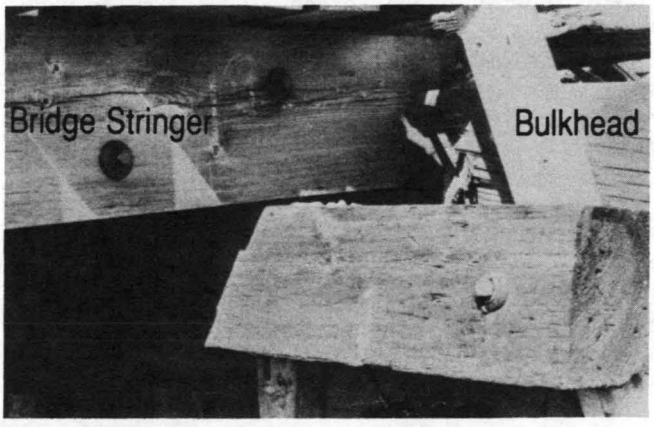

FIGURE 3 Stringers of Bridge 61.9 that were driven though the bulkhead wall by convergence of the stream banks during the 1964 Alaska earthquake [after McCulloch and Bonilla (*4*)].

A similar type of failure occurred to a highway bridge over one of the channels of the Resurrection River near Seward. The banks of the river spread into the channel, causing more than 0.3 m of convergence between bridge abutments (Figure 4). The narrowing of the channel thrust the bridge girders and deck into the abutment wall, which fractured and rotated under the impact, allowing the deck to penetrate about 0.3 m into the adjacent fill. The ground displacement carried the adjacent bridge pier about 0.3 m toward the channel, with the top of the pier remaining attached to the deck. As shown in Figure 4, this displacement fractured the pier at the ground line and tilted the upper part of the pier outward, away from the river.

The bridge at Milepost 37.3 is representative of a structure that fractured and buckled because of compressional forces applied by the converging stream banks (Figure 5). This bridge was composed of five 4.5-m long spans. The stream banks converged about 0.18 m, causing the deck to buckle horizontally by about 1.2 m (*4*). A few similarly stressed bridge decks buckled upward rather than laterally.

Bridges that crossed streams at oblique angles commonly skewed, rather than buckled, under ground-induced compressional forces. For example, the railway bridge at Milepost 63.0 (Figure 6) skewed horizontally as a consequence of about 2.8 m of stream bank convergence. The bridge was a 58.4-m long structure supported by 14 pile bents. The convergence of the stream banks shifted the pile bents streamward on both sides of the channel. Because the direction of ground displacement was at an angle to the longitudinal axis of the bridge, the compressional forces generated horizontal forces between the deck and the southern bulkhead. These forces fractured the stringer connections at the bulkhead and deflected the deck 2.4 m eastward (to the right in Figure 6). The deck rotated and bowed horizontally as a unit, breaking connections between some pile caps and stringers and dragging others laterally with the displaced deck.

In their field investigations, McCulloch and Bonilla (*4*) found no instances in which piles had sunk to greater depths than their pre-earthquake positions. Conversely, in several instances the piles had risen. McCulloch and Bonilla attribute that rise to lateral spread of the ground toward river channels, which compressed sediments within the channels, causing channel beds to heave upward and lift the piles with the rising soil. Buoyancy of the piles and upward pull by arching superstructures also may have contributed to the upward movement.

FIGURE 4 Highway bridge over Resurrection River that was compressed by lateral spreading during the 1964 Alaska earthquake. The compression thrust the deck into and fractured the abutment wall, and ground displacement carried the adjacent pier streamward, fracturing that element at the ground line [after McCulloch and Bonilla (*4*)].

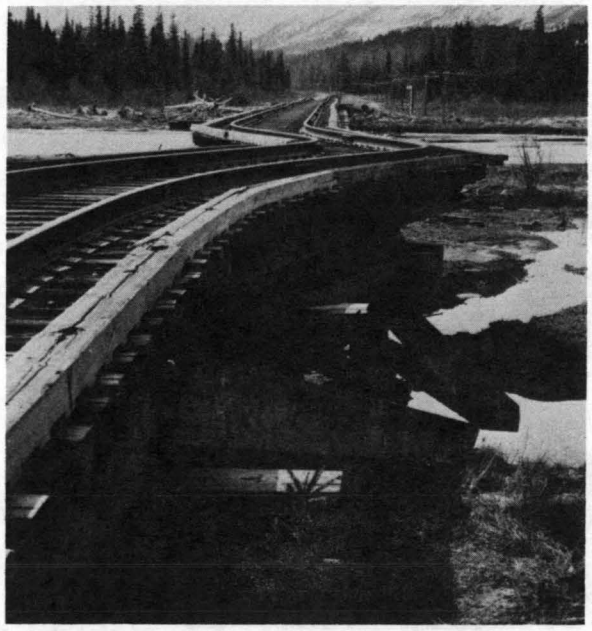

FIGURE 5 Deck of the Alaska railway bridge at Milepost 63.0 buckled by stream bank convergence of about 0.18 m [after McCulloch and Bonilla (*4*)].

Highway Bridges

Highway bridges were affected even more severely than railway bridges during the 1964 earthquake. Kachadoorian (*5*) classified more than 20 highway bridges as destroyed, by which he generally meant that foundations had failed and decks had collapsed. Nearly all of this destruction was caused by lateral displacement of piers and abutments. These displacements

FIGURE 6 The Alaska railroad bridge at Milepost 63.0 that was compressed by lateral ground displacement, causing near end of the bridge to shear connections with the bulkhead and skew to the right [after McCulloch and Bonilla (*4*)].

broke connections with the superstructure, leaving decks unsupported. One collapsed bridge—the structure over Twentymile River—is shown in Figure 7. This and other severely damaged bridges were at localities of intense liquefaction effects—including ground oscillation and lateral spread—as described by Kachadoorian (*5*):

> The seismic shaking and lateral displacement of the sediments pulled the wood ties off the caps, and the superstructure became independent of the substructure. The deck or superstructure had a vertical as well as a horizontal component of movement during the earthquake. Eventually the wood bents failed beneath the superstructure and the bridge collapsed. In many bridges the wood piles were driven through the reinforced concrete deck [Figure 7]. Eye witness reports show that the decks had an up-and-down motion period of about 1 second. That is, a wave apparently passed through the deck, and, as it passed through, the superstructure moved up and down in about a 1-second cycle. (*5*)

Kachadoorian then indicates that the up-and-down motions caused impacts between the piles and bridge decks (after the pile caps had failed) that drove the piles through the deck.

This description of bridge failure indicates that seismic shaking liquefied the underlying soils, which in turn spread laterally toward the river channel. That ground movement pushed the pile bents riverward, shearing connections with the superstructure. The ground apparently did not move in a single uniform motion, but oscillated back and forth and up and down in waves as it migrated toward the river. This oscillatory movement caused the bridge deck to vibrate vertically—and apparently out of phase with the underlying ground—generating intense impacts between the deck and the detached piles, with the piles eventually punching through the paved surface as the deck fell to the ground.

In addition to bridges classified as "destroyed," Kachadoorian classified more than 70 bridges as severely damaged. Such a rating generally meant that abutments and pile bents shifted horizontally, breaking connections with superstructure. This action was accompanied by ramming of decks into abutment walls, severely damaging either stringers or trusses or the abutment, as shown in Figure 3. However, none of the severely damaged bridges collapsed.

With respect to postearthquake pile elevations, Kachadoorian (*5*) noted that after the earthquake, most of the piles beneath destroyed or severely damaged highway bridges were lower, but by no more than about 0.1 m. The reason for this penetration of piles is not given, but it may have been caused by pounding of the deck. This small amount of settlement indicates that major loss of pile-bearing resistance did not occur.

In total, Kachadoorian (*5*) classed 92 highway bridges (45 percent of those in the heavily shaken area) as destroyed or severely damaged. An additional 49 bridges (24 percent of the total) were classed as slightly to moderately damaged. The estimated cost to repair or replace these structures was more than $25 million (1964 dollars). The tenfold-greater monetary damage to highway bridges compared with railway bridges indicates the greater destruction to the highway structures.

Niigata, Japan, 1964

Three months after the 1964 Alaskan earthquake, a large earthquake struck the west coast of Japan near the city of Niigata. That earthquake generated some of the most widespread and spectacular effects of liquefaction of any modern earthquake. The combined effects of the 1964 Alaska and Niigata earthquakes forcefully drew the world's attention to the destructive capability of liquefaction; rigorous studies of the liquefaction phenomenon were initiated immediately thereafter. Liquefaction-induced lateral spread during the Niigata earthquake caused bank convergence of as much as 23 m across the 250-m wide Shinano River (*6*). Those displacements severely damaged one railway and three highway

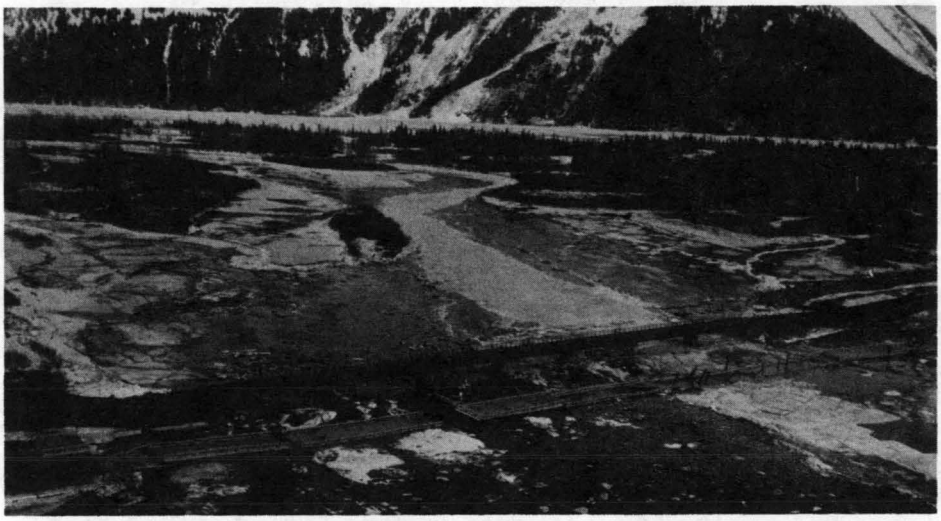

FIGURE 7 Collapsed highway bridge across Twentymile River (bridge nearest camera); a damaged but intact railway bridge is behind highway structure [after McCulloch and Bonilla (*4*)].

bridges. For example, several deck segments of the Showa highway bridge collapsed into the river as a consequence of ground displacement (Figure 8). Hamada and others (*6*) give the following description of that collapse:

> There were obvious signs that a violent collision had occurred between the girders themselves and the abutment on the left bank. From the above, it can be conjectured that a large horizontal force had been exerted on the girder from the abutment on the left bank, and this is considered to have been one of the causes of the collapse. There were also signs that the bridge pier foundations on the left bank had moved toward the center of the river. In particular, pier P_6 had tilted considerably toward the right bank. It may be considered that such movement of the bridge pier foundations also contributed to the collapse. (*6*)

The steel-pipe piles supporting another pier, P_4 (located within the river), were extracted and examined after the earthquake. The deformed shapes of those piles indicate that about 0.5 m of lateral displacement had occurred at the level of the river bed and that ground displacement reached depths as great as 7 to 8 m below the bed.

As noted by Hamada and others, horizontal displacement of the piers supporting the Showa bridge was much less than displacement of the ground a short distance either upstream or downstream from the bridge. This reduced displacement indicates that the bridge restrained ground deformation. Other bridges across the Shinano River impeded lateral ground movements as well. In the latter instances, the decks remained attached to the piers and acted as struts or braces, increasing resistance to ground displacement. For example, a postearthquake aerial photograph (Figure 9) shows reconstructed river revetments above and below the Bandai Bridge. Those revetments formed a straight line before the earthquake. The revetments were pushed toward the river during the earthquake and then reconstructed in their postearthquake position. The reduced ground displacement near the bridge is graphically illustrated by the landward curvature of the reconstructed revetments. Further evidence that the bridges restricted bank displacements is given by Hamada and others (*6*), who calculated vectors of ground displacement from photogrammetric analyses of pre- and postearthquake aerial photographs. Those vectors indicate that river bank displacements were about 8 to 9 m upstream from the Bandai Bridge, but only about 4 to 5 m near the bridge. Thus the bridge apparently restrained lateral ground movements by about 4 m.

FIGURE 8 Showa highway bridge that collapsed into the Shinano River during the 1964 Niigata, Japan, earthquake (*photograph by T. L. Youd*).

Limon Province, Costa Rica, 1991

During the April 22, 1991, earthquake in Limon Province, Costa Rica, eight major highway and railway bridges collapsed, and several other bridges were severely damaged. All of these bridges were at river crossings and in nearly all instances, liquefaction-induced ground displacement was the cause of damage.

The modes of bridge damage in Costa Rica were generally similar to those described above; that is, lateral displacement of floodplain deposits pushed abutments and piers riverward, shearing connections and causing other damage. In several instances, however, the connections between the foundation and the deck sheared readily, preventing the deck from acting as a strut or brace. The connection failures allowed the abutments and piers to readily shift or tilt toward the river channel, removing support from the superstructure. An example of this type of failure is illustrated by the tipped railroad bridge over the Rio Bananito near Bananito Sur (Figure 10). The steel-truss single-span bridge was supported by four 1.5 m by 2.1 m oval-shaped concrete caissons, one placed under each corner of the truss. Liquefaction and lateral spread on both sides of the river pushed the tops of the caissons inward (Figure 11), removing support from the truss, which then dropped and tilted downstream. Displacements of the tops of the caissons ranged from 1.9 to 5.7 m (*7*).

The highway bridge over the Rio Estrella is of interest because although the superstructure collapsed, the foundation did not permanently displace. The bridge was composed of one 25 m long plate girder section and two 75 m long truss sections. During the earthquake, the two trusses fell from their common support on a central pier and dropped into the river (Figure 12). Simultaneously, the roadway approach to the south end of the bridge settled about 2 m, broke up, and

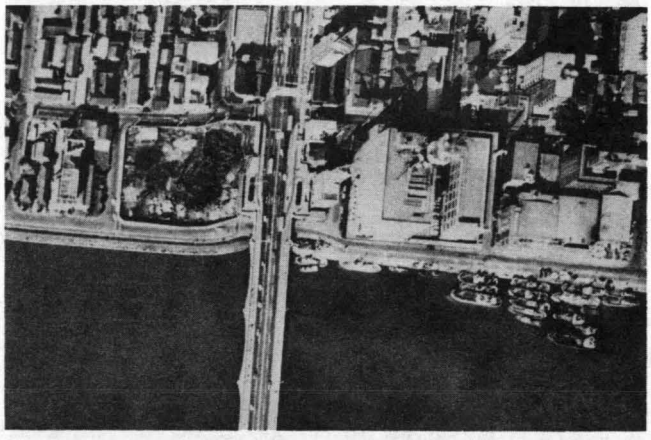

FIGURE 9 Aerial view of Bandai Bridge showing curved revetments along water-bank interface. The curvature was caused by lateral ground displacements during the 1964 Niigata earthquake [after Hamada et al. (*6*)].

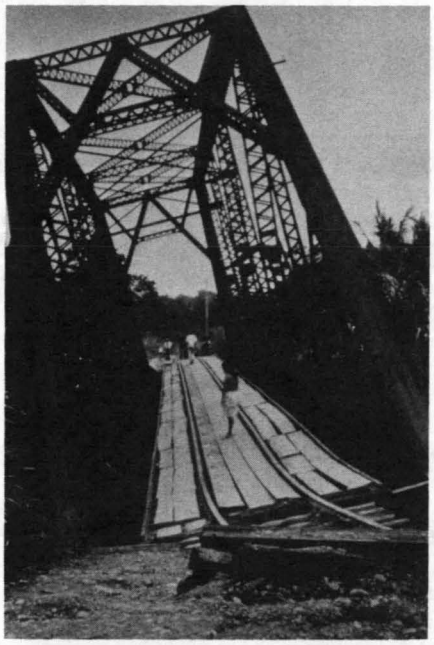

FIGURE 10 Railway bridge over the Rio Bananito that tipped during the 1991 Costa Rican earthquake; lateral ground displacement pushed the supporting caissons from the bridge seatings leaving the truss unsupported (*photograph courtesy of Laboratorio de Ingeniria Seismica de la Universidad de Costa Rica*).

FIGURE 11 Caissons beneath the Rio Bananito railway bridge that were pushed riverward by lateral ground displacement during the 1991 Costa Rica earthquake (*photograph by T. L. Youd*).

spread laterally (Figure 13). Large fissures parallel to the river developed in banana plantations on either side of the approach road. These effects indicate that liquefaction and lateral spread were widespread near the southern abutment.

Youd et al. (*7*) surveyed the bridge site after the earthquake and compared measured distances with those noted on the bridge plans (Table 1). Differences between the pre- and postearthquake distances were small and fall within the range of survey and construction error. These comparisons indicate

FIGURE 12 Highway bridge that collapsed into the Rio Estrella during the 1991 Costa Rica earthquake (*photograph by T. L. Youd*).

FIGURE 13 Liquefaction-induced settlement and deformation of approach fill adjacent to southern abutment of Rio Estrella highway bridge (*photograph courtesy of Laboratorio de Ingeniria Seismica de la Universidad de Costa Rica*).

that the abutments and piers withstood earthquake shaking and the development of liquefaction without significant permanent displacement. In particular, the foundation beneath the southern abutment remained in place, even though liquefaction and substantial ground disruption occurred in the immediate vicinity (Figure 13). This abutment consisted of a concrete wall supported on two substantial groups of piles, which extend to depths of about 14 m below river level (*8*).

PREDICTION OF GROUND DISPLACEMENT AND BRIDGE DAMAGE

Two pieces of information are required to determine bridge safety against ground failure: an estimate of ground displacement and an assessment of bridge capability to withstand that displacement. Some progress has been made over the past few years in developing techniques for evaluating ground displacement. Case histories have been compiled from which the primary factors controlling displacement have been identified and regression analyses have produced predictive models (*9*). Several investigators have also applied analytical techniques to estimate ground movements, but more development and

TABLE 1 Comparison of Plan and Measured Postearthquake Distances Between Bridge Elements for the Highway Bridge over Rio Estrella (*8*)

Distance Between Centers Of Bridge Seats On:	Plan (m)	Post-Earthquake (m)
North Abutment and Pier 1	25.00	24.96
Pier 1 and Pier 2	75.00	75.02
Pier 2 and South Abutment	75.00	75.24
North and South Abutments	176.32	176.14

verification of those techniques are required. The second component, assessment of the capability of bridges to resist ground displacement, is practically unstudied. Likewise, the effectiveness of remedial measures that might be used to strengthen bridges or to stabilize the ground to resist displacement has not been widely researched. It is beyond the scope of this paper to discuss these topics further except to note that much more research attention is required to develop engineering guidelines for design or retrofit of bridges to withstand liquefaction-induced ground displacements.

CONCLUSIONS

The following conclusions were reached as a result of this study:

1. Lateral spread has been the primary cause of liquefaction-induced damage to bridges. Lateral ground displacements physically have moved abutments and piers riverward, creating large shear forces at connections and compressional forces within the superstructure.
2. Compressional forces generated by lateral ground displacement generally cause one of the following reactions:
   a. The superstructure may act as a strut, bracing tops of abutments and piers and holding them relatively in place while the bases of these elements shift streamward with the spreading ground. This action leaves piers and abutments tilted outward away from the river.
   b. The connections between the foundation and the superstructure may fail, allowing piers and abutments to shift or tilt toward the river with little restraint. In this instance, the deck may strike the backwall of the abutment, which may either fracture the wall and allow the deck to penetrate into the embankment or deflect the deck upward and over the abutment and embankment.
   c. The deck may buckle laterally or vertically, causing severe damage to the superstructure.
3. Only limited study has been made of bridge damage caused by ground displacement or of mitigative measures to prevent such damage. More research is needed on this topic.

REFERENCES

1. National Research Council. *Liquefaction of Soils During Earthquakes.* National Academy Press, Washington, D.C., 1985.
2. Halley, W. *The Centennial Year Book of Alameda County, California.* Oakland, 1876.
3. Peters, K. E., and R. B. Hermann. *First-Hand Observations of the Charleston Earthquake of August 31, 1886, and Other Earthquake Materials.* Bulletin 41, South Carolina Geological Survey, 1986.
4. McCulloch, D. S., and M. G. Bonilla. *Effects of the Earthquake of March 27, 1964, on the Alaska Railroad.* Professional Paper 545-D. U.S. Geological Survey, 1970.
5. Kachadoorian, R. *Effects of the Earthquake of March 27, 1964, on the Alaska Highway System.* Professional Paper 545-C. U.S. Geological Survey, 1968.
6. Hamada, M., S. Yasuda, R. Isoyama, and K. Emoto. *Study on Liquefaction Induced Permanent Ground Displacements.* Association for the Development of Earthquake Prediction, Tokyo, Japan, 1986.
7. Youd, T. L., K. M. Rollins, A. F. Salazar and R. E. Wallace. Bridge Damage Caused by Liquefaction During the 22 April 1991 Costa Rica Earthquake. *Proceedings, 10th World Conference on Earthquake Engineering,* Madrid, Spain, 1992, Vol. 1, pp. 153–158.
8. Earthquake Engineering Research Institute. Costa Rica Earthquake Reconnaissance Report. *Earthquake Spectra,* Vol. 7, Supplement B, Oct. 1991.
9. Bartlett, S. F., and T. L. Youd. *Empirical Prediction of Lateral Spread Displacement.* Technical Report NCEER-92-0021. National Center for Earthquake Engineering Research, State University of New York at Buffalo, 1992.

Publication of this paper sponsored by Committee on Engineering Geology.

Paleoliquefaction Features as Indicators of Potential Earthquake Activity in the Southeastern and Central United States

STEPHEN F. OBERMEIER

Prehistoric earthquake-induced liquefaction features of Holocene age have been discovered in coastal South Carolina, in the epicentral area of the 1811–1812 New Madrid earthquakes, and in areas peripheral to portions to the New Madrid seismic zone. These discoveries show that areas of historic, moderate-to-strong earthquakes are likely to have been areas of strong prehistoric earthquakes in the central and southeastern United States. Locating prehistoric liquefaction features is valuable for identification of regions of potential strong earthquakes.

The central and eastern parts of North America lie within an area known to tectonic specialists as the "stable continental region" or "intraplate region" because their plate boundaries lie far away. Earthquake zones worldwide are associated chiefly with plate boundaries. Yet within central and eastern North America, some extraordinarily strong earthquakes have struck during the past 200 years. The four strongest are the 1811–1812 New Madrid earthquakes [body-wave magnitude m_b ~7.0 to 7.4; moment magnitude (**M**) ~7.8 to 8.3 (*1*)], which originated in the Mississippi Valley near Memphis, Tennessee. These events were felt as far away as Washington, D.C. A Modified Mercalli intensity of XI has been assigned to the epicentral region of several thousand square kilometers. Prominent effects of liquefaction extend over an area on the order of 10,000 km^2 and are plainly visible on the surface today (*2,3*). In 1886 another very strong intraplate earthquake [m_b ~6.7, **M** ~7.5 (*1*)] occurred near Charleston, South Carolina. Throughout much of the epicentral region, an area about 35 km wide and 50 km long, the Modified Mercalli intensity ranged from IX to X. Liquefaction effects were especially noteworthy (*4*). Other scattered strong historic earthquakes (on the order of **M**7) have taken place in southeastern Canada and the northeastern United States (*5,6*). Most of these earthquakes have also been associated with liquefaction.

To realistically assess the seismic hazard, it is necessary to know which areas of this intraplate region have the potential for future destructive earthquakes. The short historic record is not sufficient to determine if places where strong earthquakes have taken place during the past 200 to 300 years are also locales of recurring strong earthquakes. In addition, the tectonic mechanisms that cause large intraplate earthquakes are not well understood, and strong earthquakes in the intraplate region usually do not produce surface faulting that can be used to evaluate the locations and times of previous large events. For these reasons, numerous recent searches have been undertaken for secondary evidence of large prehistoric earthquakes, such as seismically induced liquefaction features (i.e., paleoliquefaction features). Paleoliquefaction features can indicate the recurrence interval of prehistoric strong earthquakes and can also be used to identify regions in which earthquake shaking has been strong enough to be of concern to engineers. The threshold for formation of liquefaction features during strong earthquakes is a horizontal acceleration on the order of 0.1 *g* (*7,8*). In addition, liquefaction data can be used in some cases to infer the magnitude of prehistoric earthquakes.

In the United States, paleoliquefaction studies have concentrated on coastal South Carolina (Figure 1), the 1811–1812 New Madrid seismic zone (Figure 2), the Wabash Valley seismic zone (Figure 2), and the northeastern United States and southeastern Canada. An overview is given here of paleoliquefaction studies in those areas except the northeastern United States and southeastern Canada, which are discussed by Tuttle and Seeber (*9*) and Tuttle et al. (*10*). Preliminary studies along the coast of the mid-Atlantic states from North Carolina to New Jersey (where no evidence of prehistoric earthquakes was found) are reported by Amick et al. (*11*).

CRITERIA FOR EARTHQUAKE ORIGIN

Earthquake-induced liquefaction in different physical settings can lead to very different manifestations of the process. For example, observers at the time of the 1886 Charleston earthquake noted the formation of great numbers of approximately circular craters along ancient beach ridges (Figure 3). Figure 4 shows how prehistoric earthquake-induced craters, now filled, appear in vertical section. In the epicentral region of the 1811–1812 New Madrid earthquakes, many thousands of more-or-less linear fissures formed through which liquefied sand vented onto the ground surface (Figure 5). In vertical section, they are now expressed as nearly vertical, planar, sand-filled fissures (dikes) that cut across the flat-lying clay and silt strata of the flood plains (Figure 6).

Because of the various expressions of earthquake-induced liquefaction, because liquefaction can have a nonseismic or-

U.S. Geological Survey, 922 National Center, Reston, Va. 22092.

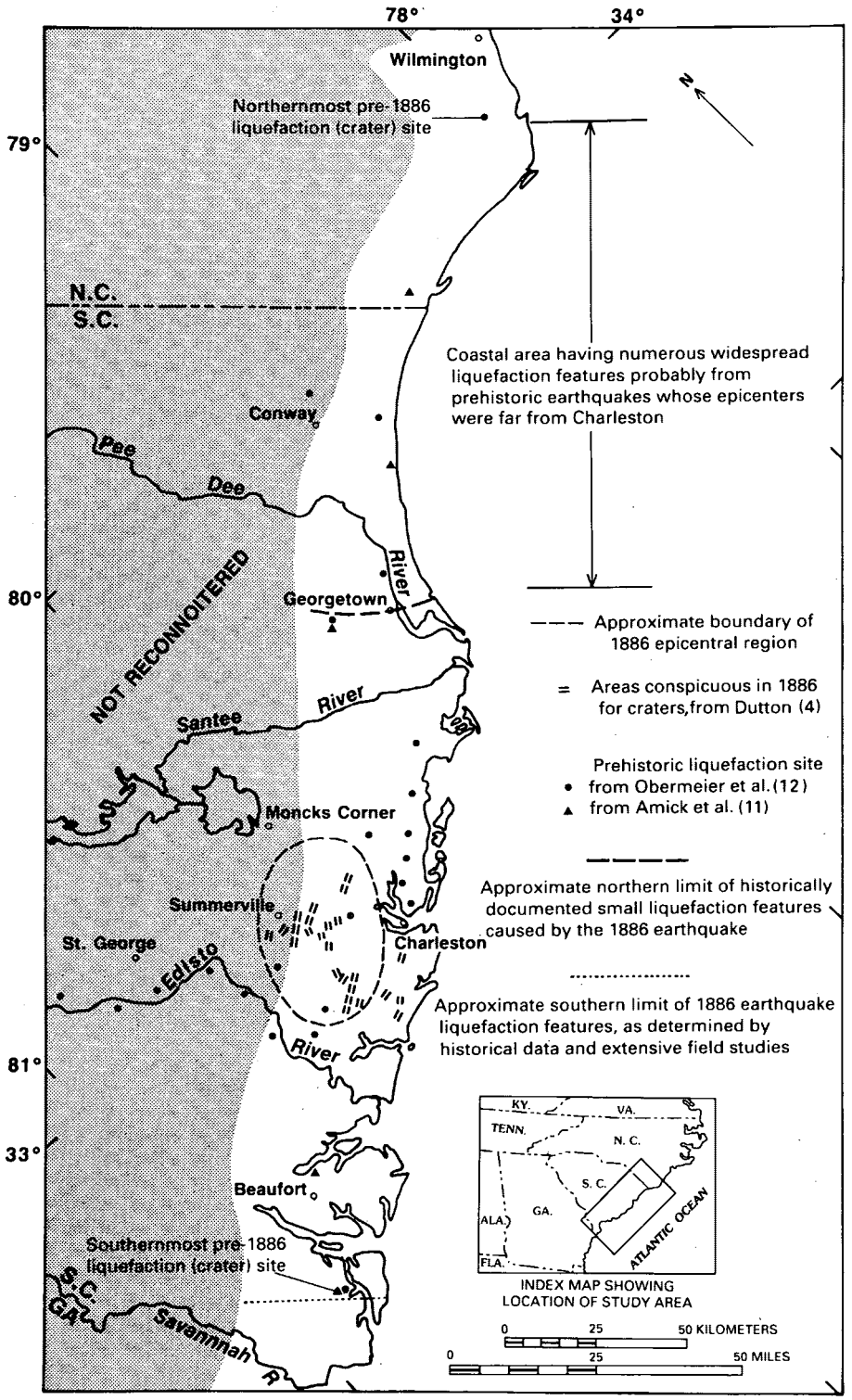

FIGURE 1 Coastal portion of South and North Carolina containing liquefaction sites. Unshaded onshore region, in which numerous ancient beach ridges lie, is predominantly marine deposits younger than about 240,000 years. Shading denotes region of older marine deposits that was not reconnoitered, except locally. Younger fluvial sediments occur locally. All liquefaction sites along the Edisto River are in fluvial sediments. Almost every liquefaction site shown represents an area where numerous liquefaction features are exposed in a network of drainage ditches several kilometers in length. Index map shows coastal region intensively searched for liquefaction features.

FIGURE 2 Approximate boundaries of New Madrid and Wabash Valley seismic zones. New Madrid seismic zone is the source area of 1811–1812 earthquakes and continues to have many small earthquakes and a few slightly damaging earthquakes. Wabash Valley seismic zone is a weakly defined zone of seismicity having infrequent small to slightly damaging earthquakes.

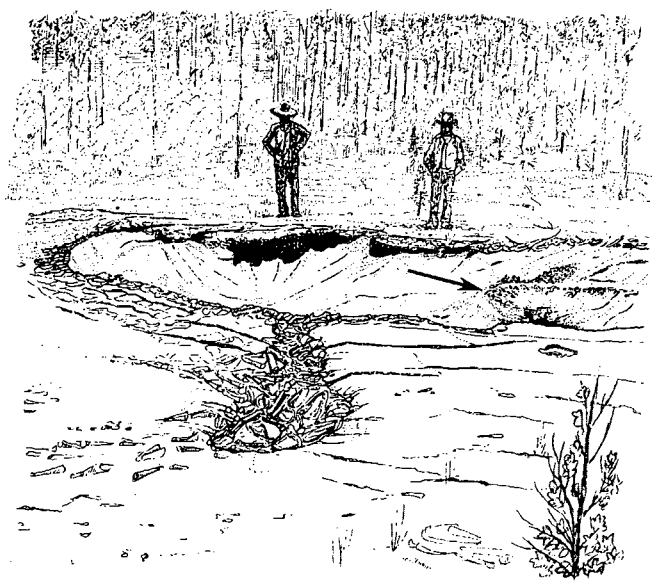

FIGURE 3 Large craterlet produced near the present Charleston airport by the 1886 earthquake. Note that the craterlet contains sand sloughing toward the lowest parts and that there is a constructional sand volcano in the lower right part of the crater (*arrow*). The craterlet is surrounded by a thin blanket of ejected sand partly veneered with cracked mud.

igin, and because nonseismic mechanisms can induce features that resemble features having an earthquake origin, it has been necessary to develop a set of interpretative guidelines for various physical settings. Criteria to interpret an earthquake origin are the following:

1. The features should have sedimentary characteristics that are consistent with an earthquake-induced liquefaction origin, that is, evidence of an upward-directed, strong hydraulic force that was suddenly applied and was of short duration.
2. The features should have sedimentary characteristics consistent with historically documented observations of the earthquake-induced liquefaction processes in the same physical setting.
3. The features should occur in groundwater settings where suddenly applied, strong hydraulic forces of short duration could not be reasonably expected except from earthquake-induced liquefaction. In particular, such settings should be extremely unlikely sites for artesian springs or for landsliding.
4. Similar features should occur at multiple locations, preferably at least within a few kilometers of one another, having similar geologic and groundwater settings. The regional pattern of size and abundance of features should be consistent with a pattern of shaking reasonably associable with an earthquake. Where evidence of age is present, it should support the interpretation that the features formed in one or more discrete, short episodes that individually affected a large area and that the episodes were separated by relatively long time periods during which no such features formed.

Emphasis has been placed on elimination of artesian conditions and landsliding as possible sources of the features. In the following sections, the application of these criteria to specific geographic-geologic settings is discussed.

SOUTHEASTERN U.S. STUDIES

The most thorough studies have been conducted in a strip of South Carolina 30 km wide that parallels the coast for about 300 km. The Charleston area is centrally located in this strip (Figure 1). Studies were concentrated here because of concern about a repetition of the 1886 earthquake (**M**~7.5). The Charleston area is also the only part of coastal South Carolina to have significant recurrences of seismicity (albeit earthquakes of small magnitude) in this century. In addition, there is an abundance of sand layers in ancient beach ridges that are especially susceptible to liquefaction and formation of craterlets. Results of the searches for paleoliquefaction features (*11,12*) show that the Charleston area and other South Carolina areas far from Charleston have been the epicentral regions of repeated strong earthquakes throughout Holocene time (i.e., the past 10,000 years).

Charleston, South Carolina, Epicentral Region

The geologic setting most commonly associated with craters is the crest or flank of Pleistocene beach ridges, where a thin surficial cover of clay-bearing sand or humate-rich sand overlies clean sand. According to first-hand observations of effects of

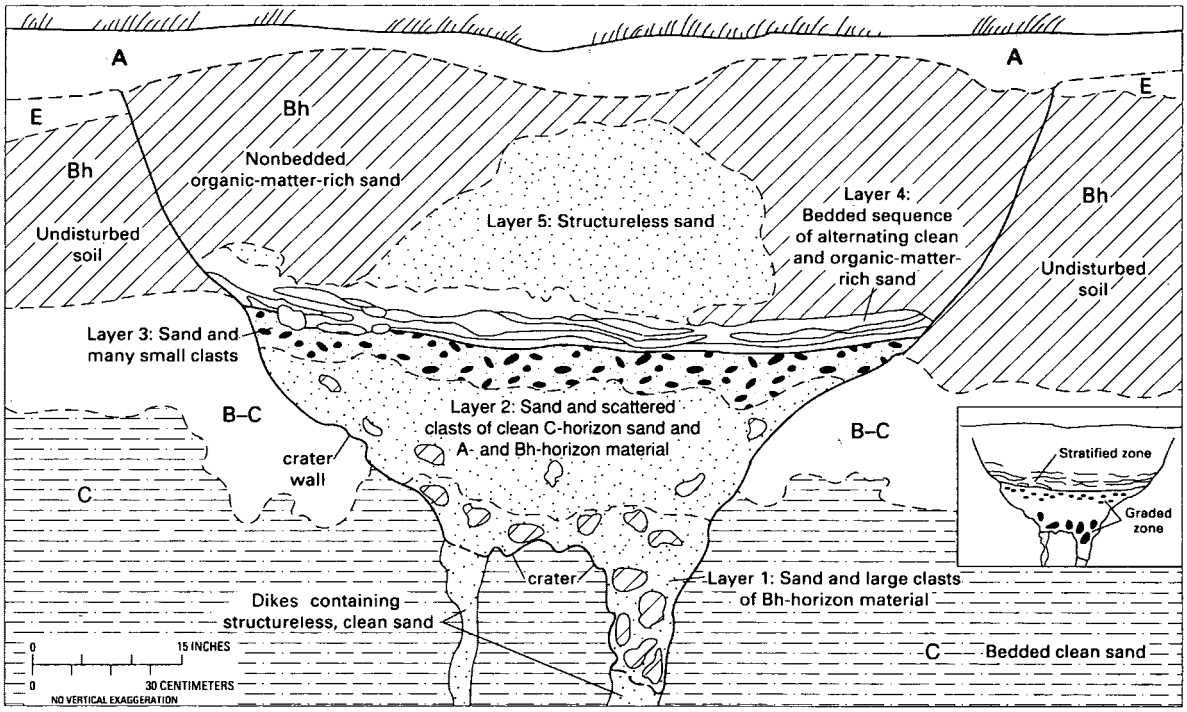

FIGURE 4 Schematic vertical section of filled, liquefaction-induced craterlet. Letters correspond to agronomical soil horizon designations. This filled crater much predates the 1886 earthquake on the basis of the thickness of the Bh horizon.

the 1886 earthquake by Sloan, "these craterlets are found in greatest abundance in belts parallel with (beach) ridges and along their anticlines" (*13*, p. 68). A schematic cross section through a beach ridge of coastal South Carolina, which is typical of the ridges described by Sloan, is presented in Figure 7.

Prehistoric craters are more abundant and tend to be larger in the vicinity of Charleston than elsewhere. Near Charleston, an earthquake origin is thought to be unequivocal for many of the prehistoric craters because (*a*) their size, shape, and sedimentary characteristics are entirely consistent with historic observations of effects of the 1886 earthquake; (*b*) some of the prehistoric craters occur at the same sites where swarms of craters were reported during the 1886 earthquake, and (*c*) alternative possible sources for the prehistoric craters have been eliminated. A complete discussion of the various possible sources for craters has been given by Obermeier et al. (*3*). For example, artesian springs are suspected to be a nonseismic mechanism that might produce features similar to those induced by seismicity. However, the presence of craters on the tops and flanks of beach ridges, where artesian springs are impossible, eliminates that mechanism. The possibility of ground disruption by thrown trees is eliminated in part because the craters contain minerals transported from deeper sources upward into the crater. Dikes that feed into the base of the craters can also be seen in some places. Engineering studies (*14*) also show that the loosest sands at depth are the same sands that were transported up in the dikes and into the craters, which is what would be expected from an earthquake-induced liquefaction origin.

The time of formation of some prehistoric craters can be estimated with high accuracy. Some craters contain bark from trees and small twigs that fell into the open crater soon after its opening. Radiocarbon dating of these materials shows that prehistoric craters in the Charleston area are approximately 600, 1,250, 3,200, 5,150, and more than 5,150 years old (*15*).

An estimate of the magnitude of the prehistoric earthquakes is provided by both historic worldwide and local observations of liquefaction. Data from the 1886 earthquake furnish a basis for comparison of crater distribution along the coast and size and abundance of the craters. Worldwide data have shown that features that have a liquefaction origin can be developed at magnitudes as low as **M**~5, but that a magnitude of about 5.5 is the lower limit at which liquefaction effects are relatively common (*16*). The source sands that produced craters in coastal South Carolina commonly are extremely susceptible to liquefaction and flowage, and this susceptibility might be interpreted to suggest that an exceptionally low magnitude earthquake could have produced the craters. However, the numerous large prehistoric craters (many having diameters as much as 3 m at a depth of 1 m below the ground surface) in the Charleston area clearly did not result from marginal liquefaction; the earthquake that produced them probably was much larger than **M**~5. In addition, the zones containing prehistoric craters with radiocarbon ages of 600 and 1,250 years extend at least as far from Charleston as the zone containing craters produced by the **M**~7.5 earthquake of 1886 (which formed over a distance of about 200 to 250 km up and down the coast, centered about Charleston).

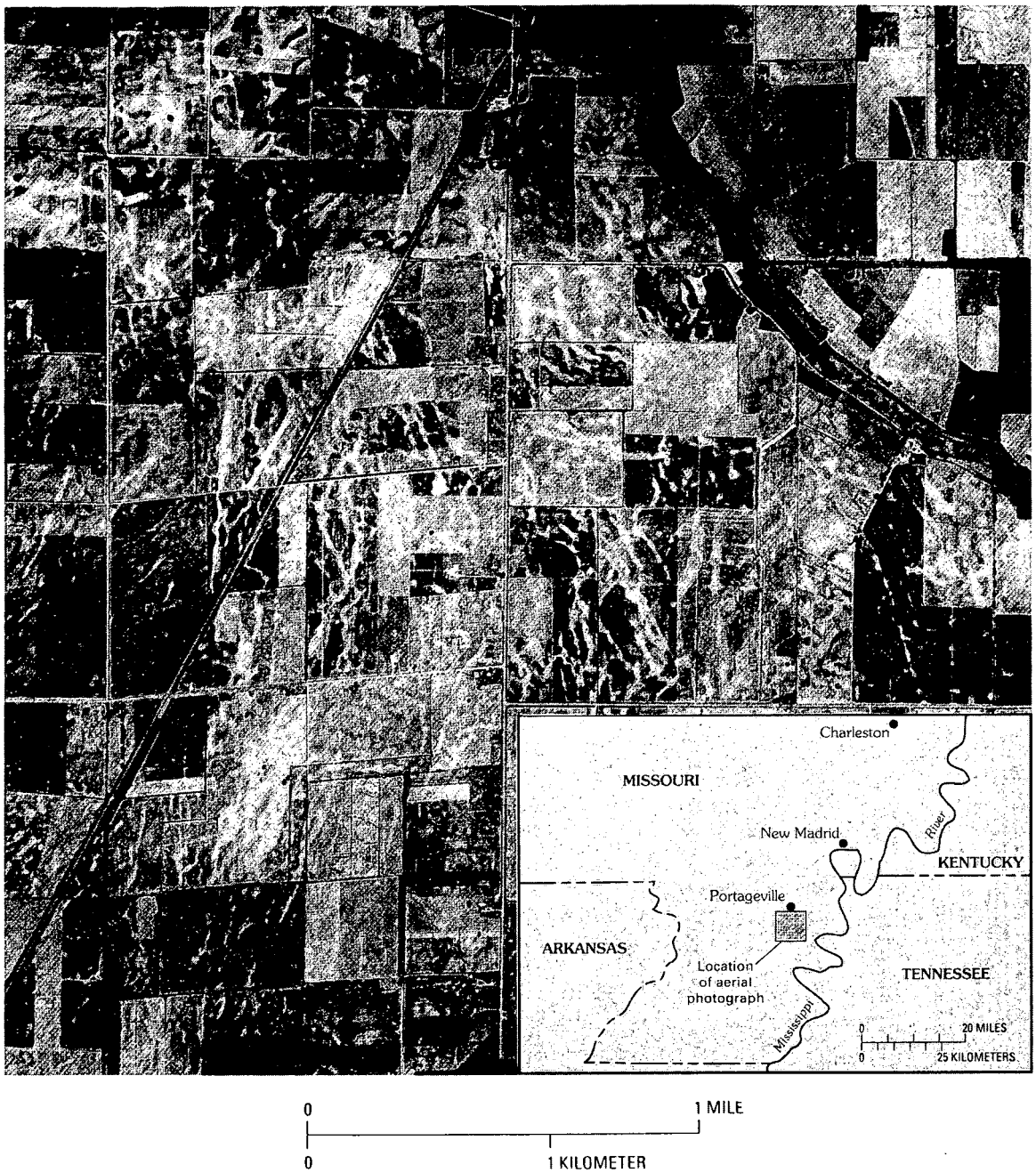

FIGURE 5 Aerial photograph showing vented sand caused by liquefaction and flowage during the 1811–1812 New Madrid earthquakes. Vented sand is light-colored and contrasts with the dark-colored silt and clay overbank (flood) deposits of the Mississippi River. The lineations were caused by ground cracks that were due largely to lateral spreading. Lineations are underlain by steeply dipping, planar, sand-filled fissures (dikes) that cut across the overbank deposits.

Interpretations of prehistoric earthquake magnitudes must account for other local factors, including water-table location and the degree of compactness of the source sands. The water table is presently very shallow (<1 m below ground surface) and probably has been essentially unchanged for the past few thousand years (*15*) at many of the sites where the craters formed. Just prior to the 1886 earthquake, the Charleston area was experiencing an extraordinarily wet period, and so the water-table conditions were optimal for production of liquefaction features (*17*). Standard Penetration Test (STP) data also show that the source sands are so loose as to be optimal for liquefaction; it is not unusual that sand deposits (fine sand and silty sand) in coastal South Carolina have STP blow counts as low as 2 or less (*14*). Thus, these sands are about as loose as possible, and it is difficult to conceive of any mechanism that would have made the sands significantly

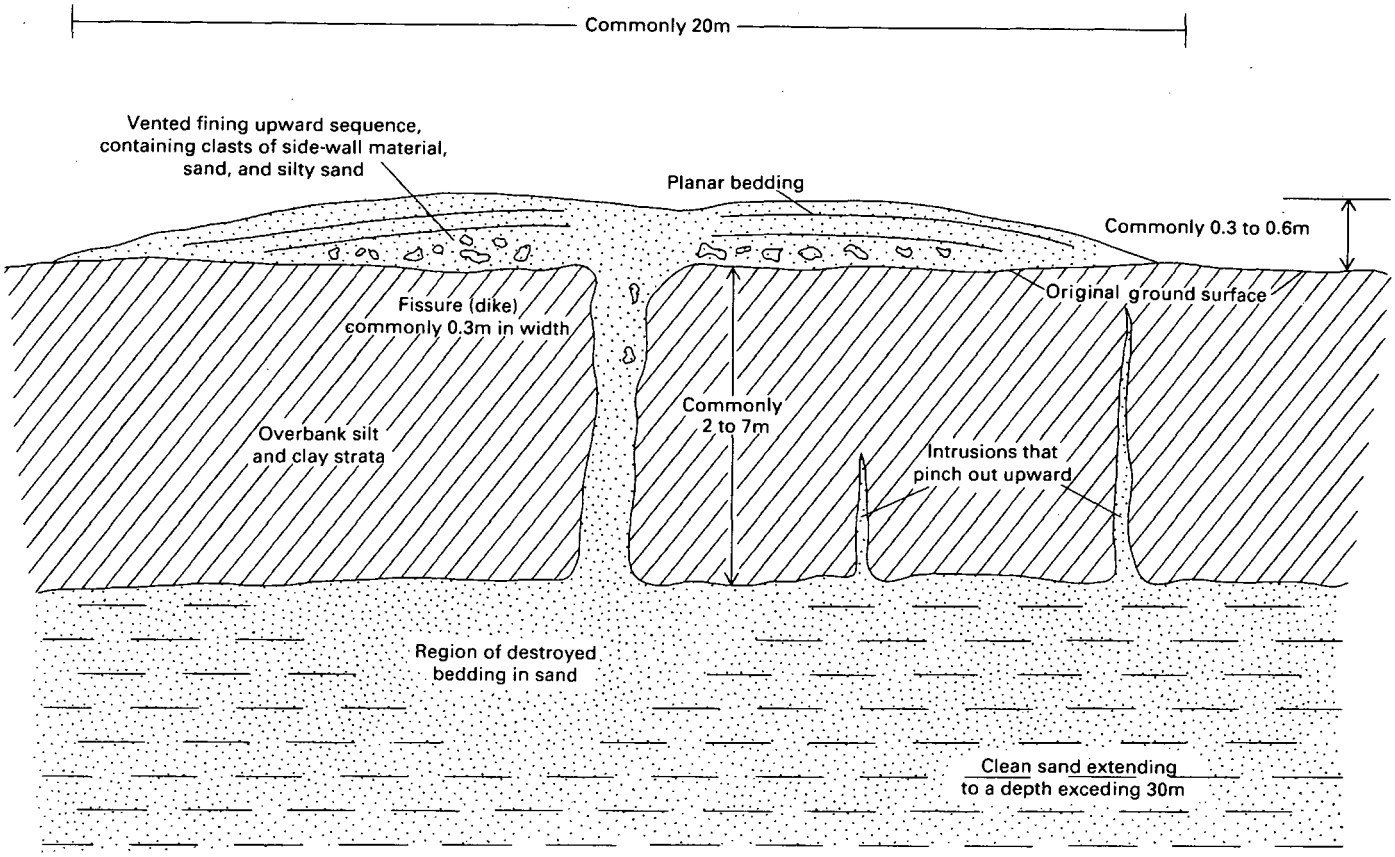

FIGURE 6 Schematic vertical section of sand-filled fissure cutting through overbank silt and clay. Situation shown is encountered at many places in epicentral region of the 1811–1812 New Madrid earthquakes.

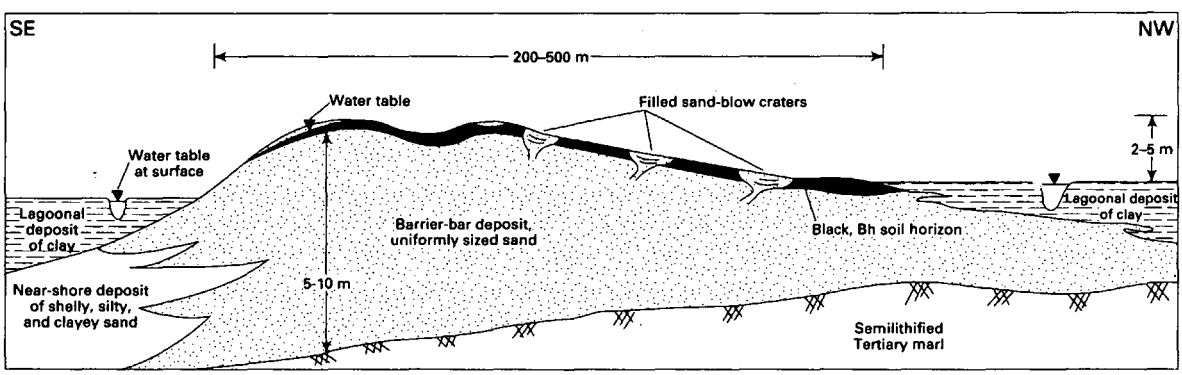

FIGURE 7 Schematic vertical cross section of representative barrier in coastal Carolinas showing sediment types, water-table locations, filled craters, and Bh (humate-rich) soil horizons. Modern shoreline is to the southeast. Lagoonal clay deposit at left is younger and lower in elevation than the barrier-bar (beach) deposit.

more compact some thousands of years ago, when the prehistoric earthquakes occurred. In summary, the geotechnical characteristics relevant to formation of craters were as favorable as possible when the 1886 earthquake struck.

It was noted above that the area along the coast having craters with ages of 600 and 1,250 years is at least equal in size to the area having craters induced by the 1886 earthquake. In addition, a comparison of the size (diameter) of the craters shows that those of the 600-year and 1,250-year events are much larger than the 1886 craters in the vicinity of Charleston and that craters for these prehistoric events in the vicinity of Charleston are larger than craters a distance away. This relation indicates that earthquakes at least as strong as the 1886 event (**M**~7.5) have taken place. (Again, some of the sands that liquefied in 1886 are still extremely loose, so progressive densification from prehistoric earthquakes could not have greatly affected liquefaction potential in 1886.)

Paleoliquefaction evidence for the event that took place 3,200 years ago has been found only in the vicinity of Charleston. Abundant craters for this event are exceptionally large, which might suggest that the earthquake was exceptionally large, but the limited size of the affected area suggests otherwise. The absence of craters far from Charleston might alternatively be explained by a lower water table caused by a lower sea level and a generally drier climate earlier in the Holocene (*15*). Absence of the 3,200-year-old craters far from Charleston might also be explained by an exceptionally shallow earthquake. The event of 5,150 years ago may have affected an area that exceeds that of the 1886 earthquake, but radiometric data are not sufficiently constrained to provide trustworthy evidence of synchronous ages of widespread craters. Craters for the oldest event (>5,150 years) in the Charleston area seem to be restricted to the immediate vicinity of Charleston. For the older events (more than several thousand years old), there is a greatly diminished chance for preservation of organic material that can be dated with accuracy. This makes it difficult to evaluate their regional distribution and causative earthquake magnitudes.

The three most recent crater-producing events have an average recurrence interval of about 600 years. The passage of only 100 years since the 1886 earthquake might suggest a low likelihood for a large earthquake within the next hundred years or so. For example, Amick and Gelinas (*15*) used a statistical procedure based on modern seismicity to determine that the probable occurrence of an event similar to the 1886 earthquake during the next two decades is less than 5 percent. Although this low likelihood seems intuitively appealing, it must be kept in mind that the causative fault (or faults) for the Charleston earthquakes has never been located despite extensive studies using geophysical, seismological, and deep bore-hole data (*18,19*). Possibly the region has a myriad of faults, each with a different potential for earthquakes (*20*), so a definitive assessment of return periods cannot be made. All that can be stated with confidence is that the paleoliquefaction data show that the Charleston area has been seismically active in the recent geologic past, and there is reason to expect that the area will occasionally experience strong earthquakes in the future.

Other Epicentral Regions

Some craters far from Charleston have an age of formation different than the ages of craters caused by the prehistoric earthquakes near Charleston. Numerous craters about 1,700 years old are present in the coastal region that extends from about 75 to 150 km northeast of Charleston toward North Carolina. There are also some very old craters (probably >5,000 years) in North Carolina, as much as 50 km north of the South Carolina state boundary. Current data do not suggest that the areal distribution of craters centered northeast of Charleston approaches the span of craters about Charleston. In addition, these craters are not as large as those in the Charleston area, yet they are found in similar physical settings. It seems likely that smaller-magnitude earthquakes were responsible for their formation. Clearly more work is needed in this area. For example, at numerous crater sites in the 1886 epicentral region near Charleston, various types of engineering tests (*14*) and geologic tests (*21*) have been performed to verify that the prehistoric craters have an origin entirely consistent with an earthquake-induced liquefaction. Outside the 1886 epicentral region, though, no such assemblage of tests has yet been performed, which places an earthquake origin in doubt at some of these sites. Still, an earthquake origin is probable at these sites far from Charleston.

CENTRAL U.S. STUDIES

The great New Madrid earthquakes of 1811–1812 took place in a rift complex (Figure 8), which is suspected to be the source of strong earthquakes in the New Madrid seismic zone (*22*). The presence of the rift, now deeply buried, is interpreted mainly from indirect forms of evidence such as seismic reflection, gravity, and magnetic surveys. The rift is thought to have formed hundreds of millions of years ago as a result of tensile stresses associated with continental breakup. With time, the regional stresses changed from extension to east-west compression. The region around the rift has subsided for the past tens of millions of years, producing a basin (including the Mississippi embayment) in which sediments now have deeply buried the rift. In the New Madrid seismic zone, the correlation of the buried rift with contemporary seismicity (Figure 9) suggests that the earthquakes result from slippage along zones of weakness associated with the ancient rift structures (*22*). Hundreds of small earthquakes, and some damaging events, one as large as M6.8 (*23*), have taken place in the New Madrid seismic zone since the 1811–1812 earthquakes. This zone is one of the most seismically active in the United States.

Whereas association of seismicity with an ancient rift seems generally accepted in the New Madrid seismic zone, there is considerable doubt about the existence of a branch of the rift that projects northwestward from the confluence of the Mississippi and Ohio rivers (Figure 8) and also some doubt about the existence of a branch in the Wabash Valley seismic zone

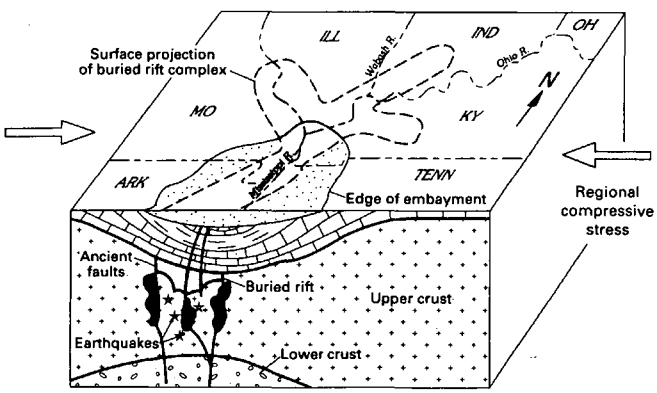

FIGURE 8 Block diagram illustrating configuration of the buried New Madrid rift complex. Branches of the rift extending northwestward along the Mississippi River and northeastward into the Wabash Valley have questionable existence. Dark areas indicate igneous intrusions near the edge of the buried rift. Hypocenters of stronger earthquakes that took place in 1811–1812 and in 1895 are in the ancient rift. Modified from Braile et al. (*22*).

(T. G. Hildenbrand, U.S. Geological Survey, unpublished data, 1992). Still, this model, in conjunction with the mapped distribution of faults and epicenters of modern earthquakes (Figure 9), makes these proposed branches suspect as potential sources of modern strong earthquakes. For example, six damaging earthquakes (M~5) have taken place in this area according to the historical record (*23*).

Concern about a repeat of an earthquake event approaching the strongest of the 1811–1812 New Madrid earthquakes has served as the impetus for several recent paleoliquefaction studies in the central United States, some of which were ongoing in 1992. These studies have concentrated on and very near the New Madrid seismic zone (Figure 2). Studies were also initiated in 1990 in the Wabash Valley of Indiana-Illinois. Although these studies in both seismic zones are ongoing, important preliminary results have been reported.

New Madrid Seismic Zone

Figure 10 shows the area of extensive liquefaction caused by the 1811–1812 earthquakes. The epicentral region for the 1811–1812 earthquakes almost certainly lies in the center of the area of extensive liquefaction. Isolated instances of venting of liquefied sand were reported as far to the northwest as St. Louis, Missouri (Figure 2), on the flood plain of the Mississippi River, and as far to the northeast as the lowermost

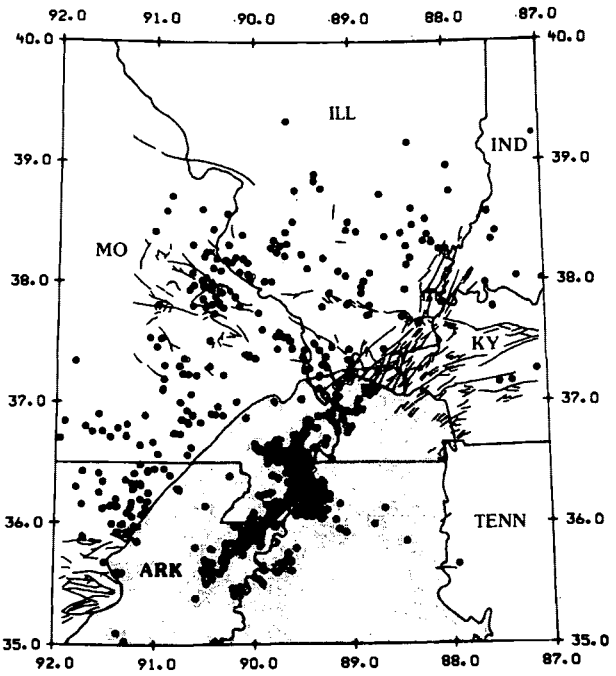

FIGURE 9 Map view of the area shown in the block diagram in Figure 6, showing major faults in bedrock and epicenters of modern earthquakes. Pattern indicates the Mississippi embayment.

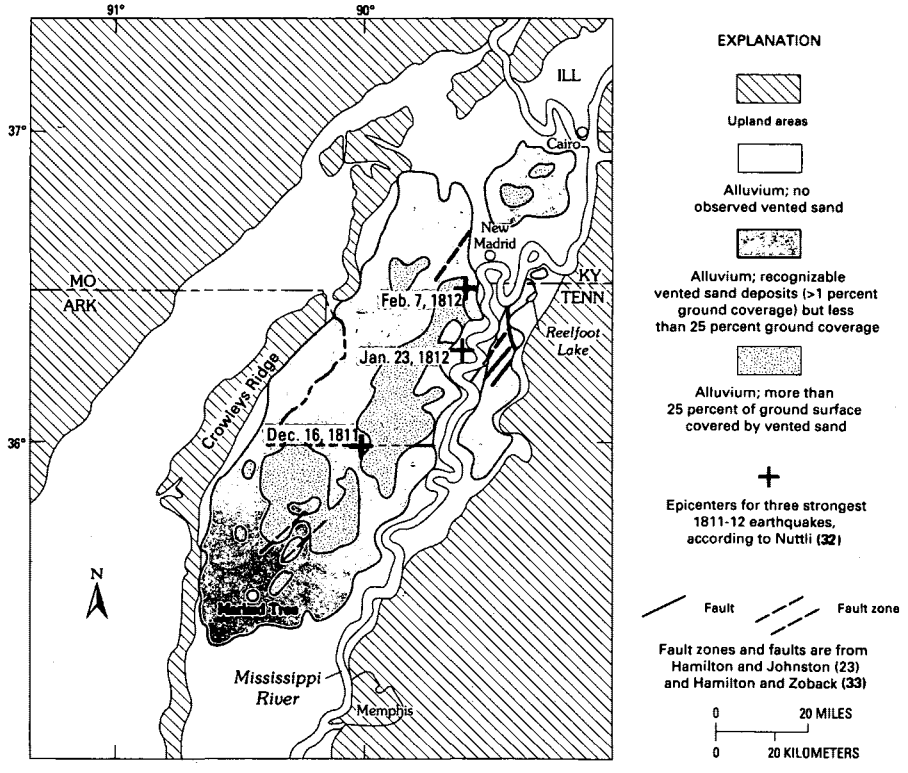

FIGURE 10 Regions having abundant vented sand, excluding modern flood plains, in the New Madrid seismic zone [from Obermeier et al. (*3*)]. Sand was presumably vented in response to 1811–1812 earthquakes. Severe liquefaction occurred locally beyond the areas shown on the map, especially along streams west of Crowleys Ridge, according to Fuller (*2*). Also shown are the approximate epicenters for the three strongest 1811–1812 earthquakes and major faults and fault zones.

Wabash Valley (*24*). These farthest sites are about 250 to 275 km from the presumed epicenter (near the town of New Madrid) for the strongest earthquake of the series, the event of February 7, 1812 (**M**~8.3).

The epicentral region lies in low-relief alluvial lowlands that have thick strata of fine and medium sand at shallow depth and a very high water table. Therefore the lowland area is well suited for production of earthquake-induced liquefaction features. The area is made up largely of braid-bar terraces of late Wisconsinan age, which formed in response to high-discharge streams carrying great quantities of sand in glacial meltwater. Sand beneath the terraces generally is thicker than 30 m. At most places the sand is capped with clay- and silt-rich strata a few meters thick. The water table appears to have been very shallow at many places since the terraces were formed (*25*). Thus, it seems reasonable that if very strong earthquakes occurred during the Holocene, the geologic record should have liquefaction features such as the dikes shown in Figures 5 and 6.

Terraces in the lowlands are exposed in vertical section by a network of hundreds of kilometers of drainage ditches that traverse the area. Wesnousky and Leffler (*25*) recently completed an extensive search of 50 km of ditch banks for pre-1811–1812 liquefaction features, mainly in the vicinity of the Missouri-Arkansas border near where the epicenter for the December 16, 1811, earthquake is shown in Figure 10. In a more limited search, they examined about 15 km of ditches southwest of the town of New Madrid. Ages of sediments that they searched ranged from about 5,000 to 10,000 years. They observed many hundreds of sand-filled fissures (dikes) caused by the 1811–1812 earthquakes but no pre-1811–1812 liquefaction features. About 10 years ago, Obermeier searched about 10 km of ditches near the southern end of the region of extensive liquefaction shown in Figure 10 and found only equivocal evidence for a small liquefaction-producing event in the early Holocene. Rodbell and Schweig (*26*) recently completed excavations in a terrace where 1811–1812 earthquake liquefaction was extensive and found no evidence of activity before 1811–1812. The terrace, about 20 km south of Reelfoot Lake, has an age exceeding 20,000 years. In the epicentral region of the 1811–1812 earthquakes (Figure 2), definitive evidence for pre-1811–1812 liquefaction has been found only near Reelfoot Lake (*27*) and at a site about 30 km northeast of Reelfoot Lake (*28*). Russ (*27*) interpreted the evidence to indicate the occurrence of three earthquakes sufficiently large to induce liquefaction during the past 2,000 years, and on that basis he suggested a recurrence interval of 600 years for liquefaction-producing events. Saucier (*28*) estimated an average recurrence interval of 470 years for liquefaction-producing events in the past 1,300 years.

It is probable that the magnitudes of the earthquakes that produced the prehistoric liquefaction features reported by Russ and Saucier did not approach the strengths of the strongest of the 1811–1812 earthquakes, as indicated by the limited areal distribution of the prehistoric liquefaction features (again, no prehistoric liquefaction features were found by Wesnousky and Leffler to the west and southwest of Reelfoot Lake or by Rodbell and Schweig to the south of Reelfoot Lake). The threshold magnitude for producing liquefaction features in the region is about m_b 6.0 to 6.2 (**M**6.4 to 6.8) on the basis of historical observations of liquefaction-producing events in the New Madrid seismic zone (*29*). Therefore, the prehistoric earthquakes were probably stronger than **M**~6.4, but because of the limited span of liquefaction, they did not approach the strength of any of the four strongest 1811–1812 events (m_b ~7.0 to 7.4; **M**~7.8 to 8.3).

Good evidence for prehistoric liquefaction in the form of sand-filled dikes has also been found about 50 km west of the epicenter for the February 7, 1812, earthquake (Figure 10). The dikes are west of Crowleys Ridge in an alluvial lowland in which the physical setting and liquefaction susceptibility are comparable with those in the lowland region east of Crowleys Ridge where such extensive development of liquefaction features took place in 1811–1812. Large portions of the lowlands west of Crowleys Ridge are a few tens of thousands of years old (*28*).

The features west of Crowleys Ridge are small to medium-sized scattered dikes. Ages of dike formation are not well constrained. However, Vaughn (*30*) suggested that there have been three or four prehistoric liquefaction-producing earthquakes during approximately the past 20,000 years. These prehistoric liquefaction episodes have not yet been recognized east of Crowleys Ridge, suggesting either that the earthquakes that produced the features were local events originating west of Crowleys Ridge or that the features may represent pre-Holocene earthquakes in the epicentral region of the 1811–1812 earthquakes.

Obermeier has made a limited search for liquefaction features in the banks of the lowermost Ohio River downstream from the confluence with the Wabash River (Figure 8) as well as a search of the banks of the Tennessee River downstream from Kentucky Lake. At least 20 km of exposed banks were examined in sediments that are at least as old as 4,000 years in most places. No evidence of pre-1811–1812 liquefaction was found beyond the immediate vicinity of the Wabash Valley (discussed in the next section). There is no reason to suspect that the liquefaction susceptibility has changed greatly through middle to late Holocene time. Thus, it is unlikely that very strong shaking (more than about 0.2 *g*) or a very strong earthquake (much higher than about **M**7) has occurred in the immediate vicinity of the lowermost Ohio Valley in the past 4,000 years.

Wabash Valley Seismic Zone

Good liquefaction evidence shows that at least one very strong prehistoric earthquake has struck the lowermost Wabash Valley (*31*). Sand-filled dikes occur near the confluence of the Wabash with the Ohio River and northward about 200 km in the Wabash Valley. Most of the dikes are exposed in banks of the Wabash River and tributary streams. Present data indicate that almost all the dikes formed in response to an earthquake between about 5,000 and 7,500 years ago.

Because almost all the sand-filled dikes in the Wabash Valley were found in the banks of rivers, and therefore possibly were very near the rivers when they formed, a special effort was required to determine that the dikes were not caused by nonseismic mechanisms such as landsliding or artesian conditions. The criteria discussed above for verifying an earthquake origin were used as the guide.

The sand-filled dikes in the Wabash Valley have formed in a physical setting very similar to the area of extensive liquefaction in the epicentral region of the 1811–1812 New Madrid earthquakes (Figure 10). An earthquake origin for the Wabash Valley dikes is thought to be highly probable because (*a*) the sand dikes have the same characteristics as those in the 1811–1812 epicentral region, (*b*) artesian conditions that could have produced dikes were extremely unlikely at many sites, and (*c*) modern landsliding in the Wabash Valley region (or anywhere else in a similar physical setting) has not been shown to produce dikes similar to those of the Wabash Valley (*31*).

The earthquake magnitude for the largest event has been estimated by comparing the span of liquefaction features (exceeding 200 km) in the Wabash Valley with the span of other historic liquefaction-producing earthquakes in the central and eastern United States (*31*). Calibration was provided by effects of the 1811–1812 New Madrid earthquakes; the 1895 Charleston, Missouri, earthquake; and the 1886 Charleston, South Carolina, earthquake. Such a comparison yields an earthquake having an estimated moment magnitude on the order of 7.5; the epicenter was approximately in the center of the Wabash Valley seismic zone shown in Figure 2.

Intensive ongoing studies are widening the study area much beyond the limits of the Wabash Valley seismic zone and are providing engineering data (such as minimum accelerations) to refine preliminary interpretations of the magnitude of the large prehistoric event. Whatever the magnitude, it appears that the potential exists for very strong earthquakes whose magnitudes are much larger than any in the historic record to strike the Wabash Valley on a rare, infrequent basis.

SUMMARY

Not only have paleoliquefaction studies proven to be valuable for interpreting recent prehistoric earthquake activity, but this method is one of the most important for assessing hazardous zones in intraplate portions of central and eastern North America. Interpretations of an earthquake origin and magnitude for suspected liquefaction features are best made by geologic field studies in combination with geotechnical engineering field studies and calculations.

Earthquake-magnitude prediction models used by seismologists are based on measurements of very recent earthquakes; this record is far too limited in time to be meaningful. A good example of the inherent error in this method is provided by comparison of results of paleoliquefaction studies in the 1811–1812 New Madrid epicentral region with predictions using the seismological approach of statistical mechanics. The discussion by Wesnousky and Leffler (*25*) points out that the seismological approach predicts a recurrence about every 600 years for the great 1811–1812 earthquakes in the New Madrid seismic zone. In contrast, the absence of widespread paleoliquefaction features indicates that no earthquakes as strong as those of 1811–1812 occurred in the last 5,000 to 10,000 years.

Many fundamental issues need to be resolved before seismological statistical measurements on modern earthquakes can be used as the basis for predictions. These issues include determining whether strong earthquake activity in a local area is time dependent or time independent and determining the tectonic causes of earthquakes in the intraplate region of central and eastern North America. Paleoliquefaction studies can serve an important role in resolving these issues.

Paleoliquefaction studies show that very strong earthquakes have struck in some unexpected places but that earthquakes weaker than expected have struck in other places. The studies also show that strong intraplate earthquakes have a tendency to recur at or very near a given region but at widely spaced time intervals.

REFERENCES

1. Johnston, A. C. The Stable-Continental-Region Earthquake Data Base. In *Methods for Assessing Maximum Earthquakes in the Central and Eastern United States* (K. J. Coppersmith and others, eds.), Project RP-2556-12, Electric Power Research Institute, Palo Alto, Calif., in press.
2. Fuller, M. L. *The New Madrid Earthquake.* Bulletin 494. U.S. Geological Survey, 1912, 119 pp.
3. Obermeier, S. F., R. B. Jacobson, J. P. Smoot, R. E. Weems, G. S. Gohn, J. E. Monroe, and D. S. Powars. *Earthquake-Induced Liquefaction Features in the Coastal Setting of South Carolina and in the Fluvial Setting of the New Madrid Zone.* Professional Paper 1504. U.S. Geological Survey, 1990, 44 pp.
4. Dutton, C. E. The Charleston Earthquake of August 31, 1886. In *U.S. Geological Survey Ninth Annual Report 1887–88,* 1889, pp. 203–528.
5. Adams, J. Seismicity and Seismotectonics of Southeastern Canada: Proceedings of Conference on Earthquake Hazards and Design of Constructed Facilities in the Eastern United States. *Annals of the New York Academy of Sciences,* Vol. 558, 1989, pp. 40–53.
6. Tuttle, M., and L. Seeber. Earthquake-Induced Liquefaction in the Northeastern United States: Proceedings of Conference on Earthquake Hazards and Design of Constructed Facilities in the Eastern United States. *Annals of the New York Academy of Sciences,* Vol. 558, 1989, pp. 196–207.
7. National Research Council, Commission on Engineering and Technical Systems, Committee on Earthquake Engineering. *Liquefaction of Soils during Earthquakes.* National Academy Press, Washington, D.C., 1985, 240 pp.
8. Ishihara, K. Stability of Natural Soil Deposits during Earthquakes. In *Proceedings of the Eleventh International Conference on Soil Mechanics and Foundation Engineering,* San Francisco, Vol. 1, 1985, pp. 321–376.
9. Tuttle, M., and L. Seeber. Historic and Prehistoric Earthquake-Induced Liquefaction in Newbury, Massachusetts. *Geology,* Vol. 19, 1991, pp. 594–597.
10. Tuttle, M., P. Cowie, and L. Wolf. Liquefaction Induced by Modern Earthquakes as a Key to Paleoseismicity—A Case Study of the 1988 Saguenay Earthquake. In *Proceedings of the 19th Water Reactor Safety Information Meeting,* U.S. Nuclear Regulatory Commission, Washington, D.C., in press.
11. Amick, D., R. Gelinas, G. Maurath, R. Cannon, D. Moore, E. Billington, and H. Kemppinen. *Paleoliquefaction Features along the Atlantic Seaboard.* Report NUREG/CR-5613. U.S. Nuclear Regulatory Commission, Washington, D.C., 1990, 146 pp.
12. Obermeier, S. F., R. E. Weems, and R. B. Jacobson. *Earthquake-Induced Liquefaction Features in the Coastal South Carolina Region.* Open-File Report 87-504. U.S. Geological Survey, 1987, 13 pp.
13. Peters, K. E., and R. B. Herrmann (compilers and eds.). *First-Hand Observations of the Charleston Earthquakes of August 31, 1886, and other Earthquake Materials.* South Carolina Geological Survey Bulletin 41, 1986, 116 pp.
14. Martin, J. R., and G. W. Clough. *Implications from a Geotechnical Investigation of Liquefaction Phenomena associated with Seismic Events in the Charleston, South Carolina Area.* Virginia Polytechnic Institute and State University, Blacksburg, 1990, 414 pp.

15. Amick, D., and R. Gelinas. The Search for Evidence of Large Prehistoric Earthquakes along the Atlantic Seaboard. *Science,* Vol. 251, 1991, pp. 655–658.
16. Ambraseys, N. N. Engineering Seismology: Earthquake Engineering and Soil Dynamics. *Journal of the International Association for Earthquake Engineering,* Vol. 17, 1988, pp. 1–105.
17. Taber, S. Seismic Activity in the Atlantic Coastal Plain near Charleston, S.C. *Bulletin of the Seismological Society of America,* Vol. 4, 1914, pp. 108–160.
18. Rankin, D. W. (ed). *Studies Related to the Charleston, South Carolina, Earthquake of 1886—A Preliminary Report.* Professional Paper 1028. U.S. Geological Survey, 1977, 204 pp.
19. Gohn, G. S. (ed). *Studies Related to the Charleston, South Carolina, Earthquake of 1886—Tectonics and Seismicity.* Professional Paper 1313. U.S. Geological Survey, 1983 (Chapters A through T separately paged).
20. Weems, R. E., and S. F. Obermeier. The 1886 Charleston Earthquake—An Overview of Geologic Studies. In *Proceedings of the 17th Water Reactor Safety Information Meeting,* Report NUREG/CP-0105, U.S. Nuclear Regulatory Commission, Washington, D.C., 1990, pp. 289–313.
21. Gelinas, R. L. *Mineral Alterations as a Guide to the Age of Sediments Vented by Prehistoric Earthquakes in the Vicinity of Charleston, South Carolina.* M.S. thesis. University of North Carolina, Chapel Hill, 1986, 304 pp.
22. Braile, L. W., W. J. Hinze, J. L. Sexton, J. R. Keller, and E. G. Lidiak. Tectonic Development of the New Madrid Seismic Zone. In *Proceedings of the Symposium on the New Madrid Seismic Zone* (P. L. Gori and W. W. Hays, eds.), Open-File Report 84-770, U.S. Geological Survey, 1984, pp. 204–233.
23. Hamilton, R. M., and A. C. Johnston (eds.). *Tecumseh's Prophecy—Preparing for the Next New Madrid Earthquake.* Circular 1066, U.S. Geological Survey, 1990, 30 pp.
24. Youd, T. L., D. M. Perkins, and W. G. Turner. Liquefaction Severity Index Attenuation for the Eastern United States. In *Proceedings from the Second U.S.-Japan Workshop on Liquefaction, Large Ground Deformation, and Their Effects on Lifelines* (T. D. O'Rourke and M. Hamada, eds.), Technical Report NCEER-89-0032, State University of New York at Buffalo, 1989, pp. 438–452.
25. Wesnousky, S. G., and L. M. Leffler. On the Search for Paleoliquefaction in the New Madrid Seismic Zone. *Seismological Research Letters,* Vol. 82, No. 4, 1992, pp. 1756–1785.
26. Rodbell, D. T., and E. S. Schweig. The Record of Seismically Induced Liquefaction on Late Quaternary Terraces in Northwestern Tennessee. *Bulletin of the Seismological Society of America,* in press.
27. Russ, D. P. Late Holocene Faulting and Earthquake Recurrence in the Reelfoot Lake Area, Northwestern Tennessee. *Geological Society of America Bulletin,* Vol. 90, 1979, pp. 1013–1018.
28. Saucier, R. T. Geoarchaeological Evidence of Strong Prehistoric Earthquakes in the New Madrid (Missouri) Seismic Zone. *Geology,* Vol. 19, 1991, pp. 296–298.
29. Obermeier, S. F. *Liquefaction Potential in the Central Mississippi Valley.* Bulletin 1832. U.S. Geological Survey, 1988, 21 pp.
30. Vaughn, J. D. Evidence for Multiple Generation of Seismically Induced Liquefaction Features in the Western Lowlands, Southeast Missouri (abs.). *Seismological Research Letters,* Vol. 62, 1991, p. 189.
31. Obermeier, S. F., J. R. Martin, A. D. Frankel, T. L. Youd, P. J. Munson, C. A. Munson, and E. C. Pond. *Liquefaction Evidence for Strong Holocene Earthquake(s) in the Wabash Valley of Southern Indiana-Illinois, with a Preliminary Estimate of Magnitude.* Professional Paper 1536. U.S. Geological Survey, 1992, 28 pp.
32. Nuttli, O. W. Seismicity of the Central United States. In *Geology in the Siting of Nuclear Power Plants* (A. W. Hatheway and C. R. McClure, Jr., eds.), Reviews in Engineering Geology, Vol. 4, 1979, pp. 67–93.
33. Hamilton, R. M., and M. D. Zoback. Tectonic Features of the New Madrid Seismic Zone from Seismic Reflection Profiles. In *Investigations of the New Madrid, Missouri, Earthquake Region* (F. A. McKeown and L. C. Pakiser, eds.), Professional Paper 1236-F, U.S. Geological Survey, 1982, pp. F55–F82.

Publication of this paper sponsored by Committee on Engineering Geology.

Seismic Analysis of Relict Liquefaction Features in Regions of Infrequent Seismicity

JAMES R. MARTIN AND ERIC C. POND

In regions of infrequent seismicity where strong-motion data are unavailable, seismic parameters for engineering design are commonly inferred from historical intensity data. However, historical data often prove inadequate, as demonstrated by recent studies of relict liquefaction features. In appropriate environments, seismic analysis of liquefaction features using geological and geotechnical engineering procedures provides an additional means of estimating the shaking severity of past earthquakes, including prehistoric events. The procedure first requires a search for relict liquefaction features in areas where past strong earthquakes are suspected. Geotechnical parameters are then measured at sites where liquefaction features are found, and the magnitude and peak accelerations required to produce the features are estimated. Where a thorough field search of liquefiable sediments reveals no evidence of disturbance, upper limits can still be placed on the maximum possible past ground motions. Studies to estimate past ground motions during the Holocene Epoch (the past 10,000 years) have been undertaken in the eastern and central portions of the United States. In the eastern United States, this analysis suggests that the ground motions of the Charleston, South Carolina, earthquake of 1886 were lower than those suggested by interpretation of Modified Mercalli intensity data. In the central United States, preliminary analysis of liquefaction features in southern Indiana and Illinois shows that a very strong prehistoric earthquake or earthquakes occurred in the Wabash Valley seismic zone, far from the epicentral region of the 1811–1812 New Madrid earthquakes.

The shaking levels of earthquakes have traditionally been estimated on the basis of seismic instrumentation data, historical intensity data, or measurement of fault movements. Earthquake intensity data are limited by the short historical record and are generally inadequate in regions of infrequent seismicity. Intensity data are influenced by varying factors such as soil conditions, quality of building construction, and human interpretation, so estimates of ground motions based on earthquake intensities can be misleading. A more direct means for estimating past ground motions involves measurement of fault displacement, but this method cannot be used where the locations of the causative faults are unknown or where the faults are unexposed. In addition, fault studies cannot always determine whether the movements were associated with earthquakes.

Now, though, an additional approach for estimating past ground motions has been developed by the authors' combination of geological and geotechnical engineering methodologies. Liquefaction leaves in the geologic record features such as steeply dipping sand-filled fissures (dikes), gently dipping sand-filled fissures (sills), and vented sand (sand boils or blows). Geotechnical analysis of the source sediments for these features provides a means for estimating the severity of seismic shaking. Methods that relate geotechnical parameters [Standard Penetration Test (SPT) blowcounts, shear wave velocities, etc.] to liquefaction development can be used to estimate the magnitude and peak accelerations of earthquakes required to cause liquefaction of deposits of known density. In addition, where there are different generations of liquefaction features, dating provides a means for estimating the recurrence of earthquakes large enough to cause liquefaction. This information can extend the knowledge of the seismicity of a region into prehistoric times.

Such analysis of previous seismicity is most applicable where liquefaction susceptibility has been moderate to high through time and where the susceptibility is fairly constant over broad areas. Having low susceptibility can result in limitation of liquefaction effects to such a few sites over a restricted geographic area as to make the field search extremely difficult. The settings most susceptible to liquefaction contain loose, sandy sediments at shallow depth and are saturated with a high water table (*1*). In ideal situations, this analysis has the following results: (*a*) it determines the epicentral area of previous strong (i.e., liquefaction-producing) earthquakes, (*b*) it estimates the magnitude and peak acceleration levels consistent with observed liquefaction evidence, and (*c*) it estimates the attenuation pattern of the accelerations.

METHODOLOGY

The basic approach of the seismic analysis procedure involves the following:

1. Determining the areal extent of liquefaction and the age of the liquefaction features,
2. Determining the severity of liquefaction at specific sites,
3. Determining the liquefaction susceptibility of the soils at specific sites in terms of geologic factors and geotechnical engineering parameters, and
4. Using liquefaction prediction methods to place limits on the ground motions that would be consistent with the liquefaction evidence at each site.

Department of Civil Engineering, Virginia Polytechnic Institute and State University, Blacksburg, Va. 24061.

Previous Liquefaction

Field searches for liquefaction relicts are conducted along drainage ditches, river banks, and other exposures having potentially liquefiable sediments. Deep (>3 m) soil exposures often allow observation of the source strata in situ and provide the opportunity to observe small liquefaction features that did not penetrate far into overlying soils. Observations at depth are important because the absence of surficial liquefaction evidence does not necessarily mean that liquefaction did not occur at depth.

The severity of past liquefaction at specific sites is determined from factors such as the size and abundance of sand blows and the widths of sand-filled dikes in a localized area (*2*). Dating of organic material buried by vented sediment, combined with archaeological and pedological data, generally allows bracketing the ages of the liquefaction features. The distribution of liquefaction effects and the ages of many individual sites are then used to develop a picture of regional earthquake activity. Sites are next selected for detailed geotechnical studies.

The absence of liquefaction features, or "negative evidence," also plays an important role in estimating past earthquake motions. An absence of features within liquefaction-prone environments suggests that the maximum past shaking levels did not exceed threshold levels. Where the location of the water table can be bounded through time and there is no evidence of cementation or lithification of potential source deposits, negative evidence can be used to place reasonably well-defined limits on the maximum levels of past ground shaking.

There is no well-defined procedure for determining the amount of outcrop that must be searched in order to conclude that liquefaction and strong shaking has not occurred previously. Uncertainty arises because of the many varying factors that affect the development of liquefaction (soil conditions, dynamic site response, stochastic attenuation of energy from the source zone, etc.). In this study, the policy used was that at least several kilometers of outcrop must be searched, even in an area suspected to be in the near field, before any statement could be made about previous severity of shaking.

Field Site Assessment and Testing of Soils

The liquefaction susceptibility of soils is usually evaluated using in situ penetration tests. The most commonly used methods involve subsurface tests, such as the SPT or cone penetration test (CPT). Other in situ data from sand cone or shear wave velocity measurements can provide supplemental information.

Because the liquefaction susceptibility of soil is estimated using present-day penetration data, it is important to consider whether soil conditions were significantly changed as a result of past ground motions. At sites of severe liquefaction, it is likely that the ground motions greatly exceeded the threshold for liquefaction, and densification occurred almost entirely throughout the source strata [see, for example, SPT data in the epicentral region of the 1811–1812 New Madrid earthquakes reported by Obermeier (*3*)]. At sites where only marginal or no liquefaction occurred, it is likely that soil conditions underwent only minor changes. To estimate the attenuation pattern of the earthquake motions, it is necessary to perform tests at sites of increasing distance from the suspected zone of energy release, preferably at sites that experienced marginal liquefaction.

Evaluation of Previous Ground Shaking

Existing liquefaction prediction methods are used to estimate the ground shaking at each site. Two well-established methods are the simplified procedure of Seed et al. (*4*) and the Ishihara (*1*) method [Figure 1 (*left* and *right*, respectively)]. Both methods predict the threshold shaking levels required to cause venting of sand at the ground surface. The Seed method relates occurrence of sand blows to peak acceleration and earthquake magnitude on the basis of SPT blowcounts. Many case

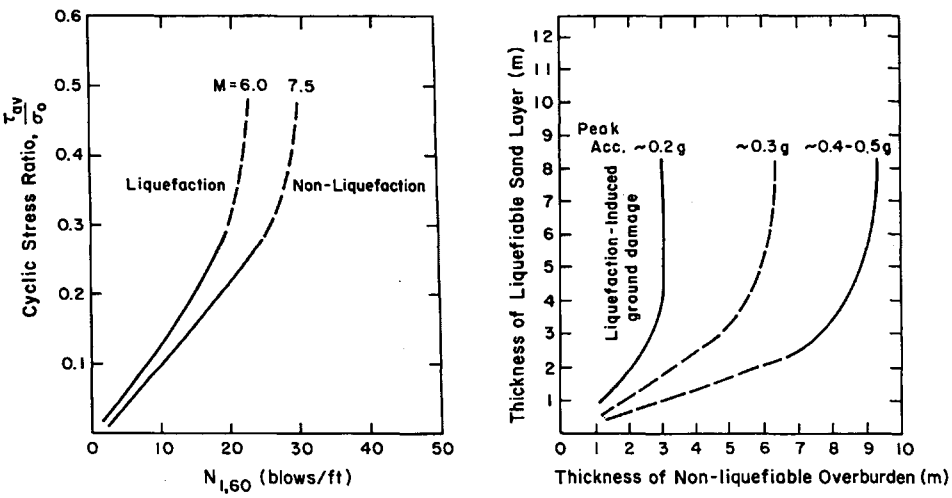

FIGURE 1 *Left:* **SPT-based liquefaction prediction curves (*4*);** *right:* **boundary curves to predict surface disruption [modified from Ishihara (*1*)].**

studies show this method to be reliable in matching field liquefaction behavior to earthquake ground motions [i.e., those by Holzer et al. (*5*) and Seed et al. (*6*)]. The Ishihara method relates the occurrence of sand blows to peak acceleration on the basis of the relative thicknesses of the liquefiable and nonliquefiable portions of the soil profile. This method accounts for the possibility that there is no liquefaction evidence at the ground surface because a nonliquefiable cap was too thick to be penetrated to the surface.

It is important to consider that the Seed and Ishihara methods were developed using liquefaction data collected largely in the western United States and other tectonic plate-margin areas, so application of the methods to intraplate regions such as the central and eastern United States can be questioned. However, a recent liquefaction case history from the 1988 Saguenay, Quebec, earthquake in eastern North America (*7*) suggests that the methods are applicable to intraplate regions. Also, it was noted previously that the Seed and Ishihara methods predict the threshold accelerations for sites of marginal liquefaction. At sites of severe liquefaction, where sediments mainly have densified, the Seed and Ishihara methods still can be used to determine the lower-bound level of past shaking. At sites of no liquefaction, upper-bound accelerations can be obtained.

Next, dynamic site response studies are performed [using a program such as SHAKE (*8*)] to determine motions in bedrock beneath the field liquefaction site. These studies assess whether the accelerations at each field site were likely the result of localized amplification (or deamplification) of the bedrock motions. The bedrock motions can then be compared with predictions of strength of shaking for various earthquake magnitudes, using models developed by seismologists.

Because liquefaction is sensitive to duration of strong shaking, the methods of Seed and Ishihara provide insight into possible combinations of the magnitude and duration of strong shaking of past earthquakes. Greater earthquake magnitudes (and longer durations of strong shaking) require smaller sustained accelerations to cause liquefaction. Earthquake magnitude can be estimated in some situations by using worldwide liquefaction data presented by Youd (*9*) or Ambraseys (*10*). Their data show relations between the epicentral distance to the farthest liquefaction effects for various earthquake magnitudes. To use the technique, though, their curves must be calibrated to the local seismotectonic setting because bedrock motion is the fundamental parameter. [An example of the use of this technique is discussed for the Wabash Valley by Obermeier et al. (*11*).]

The threshold shaking level at which an earthquake will produce liquefaction is a moment magnitude (**M**) 5.0 or higher (*10*). This magnitude of 5 gives an estimate of a minimum value for past ground motions in areas where liquefaction features are present and a maximum where no liquefaction is evident.

One way to assess the accuracy of the backcalculation techniques used for this study is to examine case histories in which soil conditions, field performances, and seismic loading levels are known. For instance, these techniques worked well when applied to effects of the 1989 Loma Prieta earthquake near San Francisco, California. The method successfully predicted peak accelerations at several liquefaction sites along San Francisco's waterfront during that earthquake. Details of this and other cases are given by Martin and Clough (*12*; unpublished data).

The following sections describe the application of the authors' seismic analysis technique to two areas of infrequent large earthquakes. The studies are in different stages and somewhat different approaches are being taken for each, but both are sufficiently advanced to discuss the preliminary results.

EASTERN UNITED STATES: CHARLESTON, SOUTH CAROLINA

One of the most prominent areas of seismic activity along the eastern seaboard of the United States is near Charleston, South Carolina (Figure 2). The 1886 Charleston earthquake is the largest during some 300 years of record. Recurring small earthquakes continue in the vicinity. The 1886 earthquake is estimated to have a Modified Mercalli intensity (MMI) of X within the epicentral region. Moment magnitude estimates are 7.5 to 7.7, with peak ground accelerations of 0.5 to 0.6 *g* (*13–15*). These estimates are based primarily on the long propagation distance of MMI V-VI effects and the severity of damage in the near field. The authors' estimates of possible combinations of earthquake magnitude and accelerations differ substantially from those made by seismologists, whose estimates are based on MMI values.

The source of seismicity near Charleston possibly originates from one or more deeply buried and probably intersecting fault zones, although definitive evidence strongly supporting a specific model has not yet been presented. Although the cause of the 1886 event is still speculative, recent studies have led to an improved understanding of the possible source mechanisms and ground motion patterns (*16*; P. Talwani, unpublished data).

Geologic-Geotechnical Setting

The low-lying Charleston region has a high water table and many areas of loose, fine sands, causing there to be high susceptibility to liquefaction. Of primary interest is a series of beach ridges, ranging in age from modern to as old as 200,000 to 240,000 years, that parallel the present coastline from North Carolina to Georgia (Figure 2). Deposits of fine and silty sands in these ridges have the highest liquefaction susceptibility relative to other geologic settings in the area. Liquefaction susceptibility of the ridges is not only high at many places but also relatively constant regionally (*17*). Typical soil conditions are shown in Figure 3, which shows the upper portion of the soil profile along Hollywood Ditch, a 2.8 km long drainage ditch excavated along the crest of a 130,000- to 230,000-year-old beach deposit.

Liquefaction Findings

Liquefaction effects of the 1886 earthquake were observed to be especially abundant in the sandy soils of the beach deposits. Eyewitness accounts presented by Dutton (*18*) describe a multitude of sand blows or "craterlets" up to 6 m in diameter. The features decreased in size and abundance with increasing

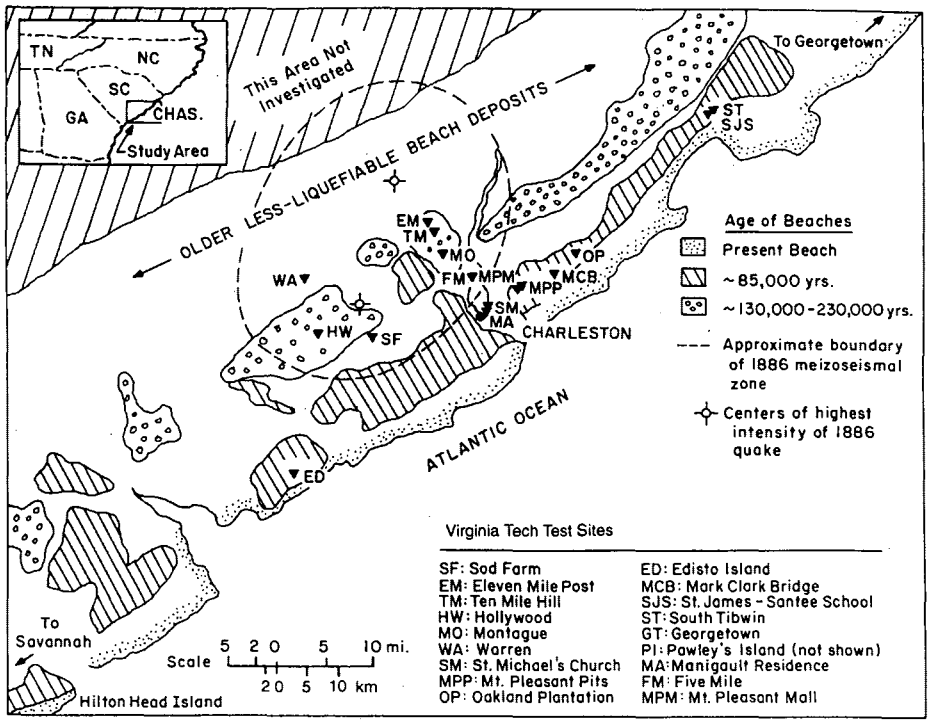

FIGURE 2 Map of coastal South Carolina showing beach deposits and test sites.

distance from the central area of strongest destruction, presumed to be the epicenter. Scattered smaller features were reported as far as 100 km from the epicentral region.

Recent field studies have led to the discovery of relict craterlets and sand dikes throughout the Charleston area (*19–21*). Many craterlets were found in the walls of drainage ditches and sand pits located within the ancient beach deposits. Dating of the craterlets showed that although many were produced by the 1886 earthquake, others were caused by prehistoric earthquakes. The evidence indicates that at least four prehistoric episodes of significant ground shaking occurred near Charleston during the last 5,000 to 6,000 years (*21*). Although this has led to an improved understanding of the seismicity near Charleston, the question remains as to the levels of ground motion that produced the liquefaction features, especially those caused by the 1886 event.

Paleoseismic Study

A paleoseismic study by Martin and Clough (*12*) has led to an estimation of the magnitude and peak accelerations of the 1886 earthquake. The study involved field reconnaissance, historical research, SPT and CPT, laboratory testing, compiling of boring logs from consulting firms, and analyses. The work focused on the properties of sediments that liquefied in the beach deposits. The locations of the test sites are shown in Figure 2.

Liquefaction analyses were carried out at each test site, and the peak ground-surface accelerations required to produce the observed liquefaction evidence were estimated. Because the sites were located at various distances from the source zone, the attenuation pattern of the earthquake motions could be estimated. Dynamic site response analyses by Martin and

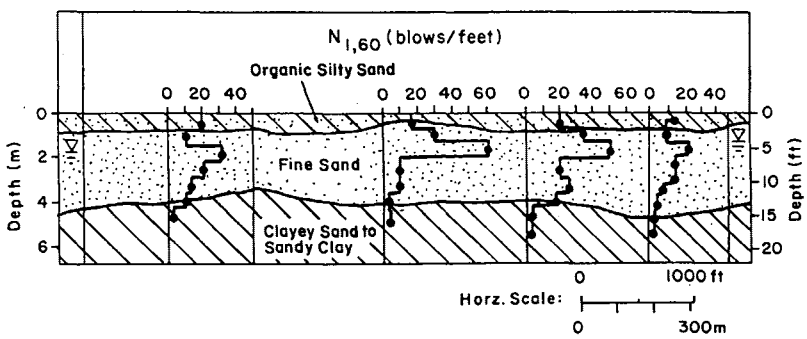

FIGURE 3 Portion of soil profile showing SPT data from Hollywood site near Charleston, South Carolina.

Clough (*12*) found that significant amplification or deamplification of the 1886 ground motions probably did not occur within the unconsolidated, near-surface (20 to 30 m depth) sediments of the beach ridges. Thus, the attenuation curve (Figure 4) developed in this study is thought to approximate the motions that occurred at the top of bedrock or semilithified material (with shear wave velocities exceeding 600 m/sec) underlying the test sites.

Estimates of peak ground acceleration are plotted versus distance from the 1886 source zone in Figure 4. The curve in Figure 4 (*top*) was developed assuming that the 1886 earthquake had a moment magnitude of 7.5. As indicated in Figure 4, the accelerations were estimated with various levels of confidence. The solid data points indicate marginal liquefaction sites at which the 1886 accelerations could be closely estimated. The solid arrows correspond to sites at which the accelerations could only be bounded. The open data points represent sites at which the accelerations could not be closely estimated. In developing the attenuation curve in Figure 4 (*top*), judgment was used in assigning different weights to the data, depending on their quality. The curve shown provides the most consistency between the estimated accelerations and the liquefaction evidence.

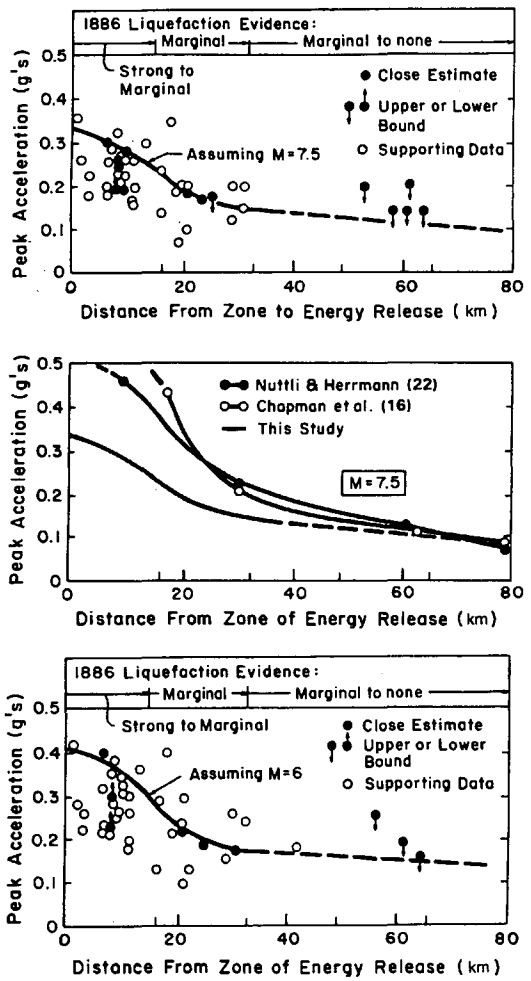

FIGURE 4 ***Top:*** **Estimated attenuation of peak accelerations assuming 1886 event of M7.5;** ***middle:*** **comparison of attenuation curve from this study with curves proposed for eastern United States for M7.5 events;** ***bottom:*** **estimated attenuation of peak accelerations assuming 1886 event of M6.**

In Figure 4 (*middle*), the attenuation curve developed in this study is compared with those proposed for the eastern United States by seismologists (*16,7*). Because some seismologists (e.g., M. Chapman, unpublished data) have suggested that the 1886 earthquake was significantly less than M7.5, a backcalculation analysis was also performed assuming that the 1886 event was M6. These results are shown in Figure 4 (*bottom*). Details of the Charleston study are available in a report by Martin and Clough (*12*).

Principal findings are summarized below:

1. If the 1886 Charleston earthquake was M7.5 and the duration of strong shaking was normal for this earthquake magnitude, the peak ground-surface accelerations are estimated to have been 0.35 to 0.4 *g* for the epicentral region and 0.1 *g* at distances of about 80 km beyond the epicentral region. The estimated attenuation pattern of the 1886 ground motions is similar in form, but values of acceleration are lower (especially in the near field) than those currently proposed by seismologists for M7.5 earthquakes in the eastern United States.
2. If the 1886 earthquake was M6, the methods used in this study yield peak accelerations approximately 20 percent higher than those associated with the M7.5 scenario.
3. The overall liquefaction evidence suggests that either the magnitude or the strongest accelerations of the 1886 Charleston earthquake were less than what have been conventionally suggested for this event (M7.7 and a_{max} = 0.5 to 0.6 *g*). Possibly the magnitude and shaking levels were initially overestimated by the seismological community because of the damage to buildings resulting from widespread liquefaction.
4. The authors' best estimates are that the 1886 earthquake had peak accelerations in the range of 0.35 to 0.4 *g*, with a moment magnitude no larger than 7.5 and possibly as low as 7.0.

CENTRAL UNITED STATES: WABASH VALLEY SEISMIC ZONE

The seismicity of the central United States has been largely defined by the great 1811–1812 earthquakes that occurred near New Madrid, Missouri. These earthquakes, as large as M8.3 and body wave magnitude m_b = 7.4 (*23*), represent the strongest historical ground shaking within the region. Liquefaction features from these earthquakes extended as far as 250 to 275 km from the epicenter (*24*). The only other historical account of strong shaking in this region was the 1895 Charleston, Missouri, earthquake, estimated as M6.8 and m_b = 5.6 (*23*). (Charleston, Missouri, is near the confluence of the Ohio and Mississippi rivers.)

The Wabash Valley Seismic Zone (WVSZ) is located along the lower Wabash River, where it forms the border between Indiana and Illinois (Figure 5). The southern end of the WVSZ is approximately 100 km northeast of the northern limit of the source of the 1811–1812 earthquakes, the New Madrid Seismic Zone. Records extending back approximately 200 years show that five slightly damaging earthquakes, having

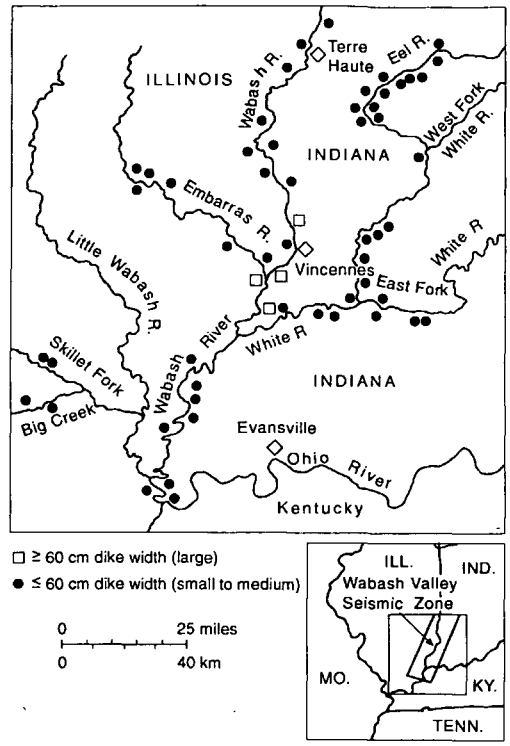

FIGURE 5 Map of lower Wabash Valley showing liquefaction sites.

estimated m_b's of 5.0 to 5.8 (M5.0 to 5.5), have occurred in and near the lower Wabash River valley (*23*). The area has long been thought capable of producing stronger than historic earthquakes. Support for the suspicion is provided by continuing seismicity and the presence of numerous faults in the Wabash region and by the proximity and suspected similar seismotectonic setting to that of the New Madrid Seismic Zone (*25*). In addition, numerous prehistoric liquefaction features have recently been discovered in the WVSZ, indicating strong prehistoric ground shaking within the region far from the 1811–1812 epicenters. Preliminary findings indicate a seismic source within or very near the Wabash Valley (*11*).

Geologic-Geotechnical Setting

Broad terraces bordering river valleys of the Wabash region are underlain by sand and gravel sediments laid down first by glacial outwash systems (about 14,000 years old) and later by the Wabash River and its tributaries. These sediments are overlain by much finer-grained flood plain and channel fill deposits of clayey silt and silty clay. The water table at most locations along the river valleys is within approximately 0.6 to 3 m of the ground surface and fluctuates with the level of nearby rivers. The setting most frequently associated with the liquefaction features is a relatively thin (1 to 4.5 m) low-permeability cap of silt- and clay-rich soil overlying a source stratum of silty-to-clean sand, gravelly sand, or in some cases, sandy gravel. Soil conditions typical of the sites investigated to date in the WVSZ are shown in Figure 6.

Liquefaction Findings

Prehistoric liquefaction features (mostly dikes and sand blows) that formed largely in source beds of sand or gravelly sand have recently been discovered throughout the WVSZ in both glacial outwash deposits and younger river deposits (*11,26*). Almost all the features appear to have been produced by a single earthquake that occurred in the region between 2,500 and 7,500 years ago, with the regional span of features apparently controlled by a single, very large earthquake. More than 200 dikes have been identified over a widespread area, including gravelly sand-filled dikes up to 2.5 m in width. The largest features have been found over an approximately 35-km-wide zone, north to south, with smaller dikes being found over a reach of at least 225 km. The largest dikes are centered near Vincennes, Indiana (see Figure 5).

Many of the soils that liquefied and flowed were either clean gravelly sands or sandy gravels. Some of the vented materials contain gravels as large as 7.5 cm in diameter. With the exception of sites investigated by Andrus et al. (*27*) following the 1983 M7.3 Borah Peak, Idaho, earthquake, the liquefaction of soils as coarse and clean as some of those in the Wabash region appears to be unprecedented. Because gravels generally have much lower liquefaction susceptibility than sands

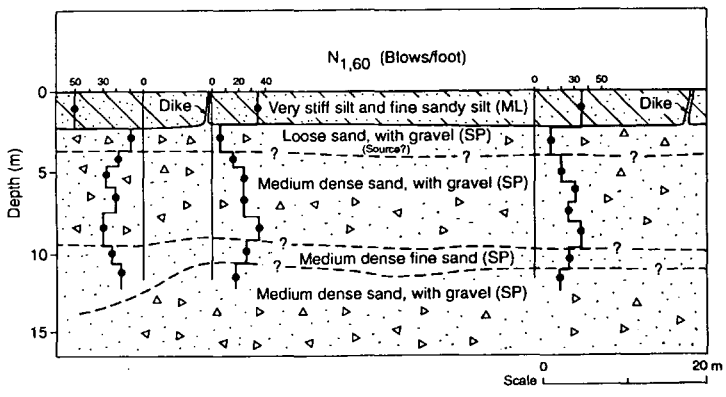

FIGURE 6 Typical soil conditions at sites where large gravelly sand dikes have been discovered in WVSZ.

(*1*), the liquefaction of the gravelly Wabash soils suggests very strong ground motions.

Paleoseismic Study

An ongoing study by the authors is designed to estimate the magnitude and peak accelerations necessary to produce the liquefaction features observed in the Wabash Valley. To date, most of the geotechnical work has been conducted at sites where the largest liquefaction effects (dikes) have been found. Preliminary estimates of the magnitude and accelerations that produced these liquefaction features have been made, and a regional site response study has been performed. On the basis of the size of the liquefaction features (widths of dikes) and the span over which dikes have been found, the authors' first estimate of the earthquake that produced the features is M7.5 (*12*). This estimate is based mainly on comparisons of the areal distribution and size of the dikes observed in the Wabash Valley with those of historic liquefaction-producing earthquakes in the central and eastern United States, using the Youd-Ambraseys curves discussed in a previous section. This magnitude of 7.5 far exceeds any earthquake occurrence in the WVSZ region during historical times.

Assuming M7.5, preliminary SPT data mainly obtained at the sites of largest dikes indicate a minimum peak ground acceleration of 0.3 *g* within a 25-km radius of the epicentral area (assuming that the epicenter is at the center of the region of largest dikes). The 0.3 *g* value represents the threshold acceleration for liquefaction at these sites, although the large size of the dikes shows that liquefaction much exceeded incipient development. At a distance of approximately 100 km from the apparent epicentral area, a lower-bound peak acceleration of 0.1 *g* is indicated. It is suspected that the upper-bound accelerations far exceed these values, although upper-bound estimates will not be possible until testing is performed at sites having either marginal or no evidence of liquefaction.

CONCLUSIONS

The shaking levels of earthquakes have been traditionally estimated on the basis of fault studies, seismic instrumentation, or historical intensity data. However, in regions where the rate of seismic activity is low, traditional methods are often of limited use. An alternative approach is to do geotechnical analysis at sites of past liquefaction. Geotechnical correlations developed between modern earthquakes and occurrence of liquefaction can be used to bracket the likely magnitude and acceleration levels of past earthquakes. Sites of past liquefaction thus can have an important role in the identification of seismic hazards and in the assessment of seismic risk. An overview of seismic analysis of liquefaction features is described for two studies in the eastern and central United States.

The principal conclusions are as follows:

1. Liquefaction relicts can be used with geotechnical procedures to estimate the magnitude and acceleration levels of past earthquakes and the attenuation of accelerations. In liquefaction-prone areas where no liquefaction evidence is found, the past peak accelerations can be estimated.

2. Seismic analysis of liquefaction features can be used in all regions in which liquefiable sediments are present. The method is best applied to regions in which soil conditions and liquefaction susceptibilities have been moderate to high at many places over a widespread area.

3. Seismic analysis of liquefaction features is of particular importance in regions of infrequent seismicity where the seismic sources are poorly defined. This approach provides estimates of past ground motions that are independent of those proposed by seismologists.

4. Seismic analysis of liquefaction features has been used to estimate the magnitude and peak accelerations of the 1886 Charleston, South Carolina, earthquake. The findings suggest that the accelerations were significantly lower than those conventionally accepted for this event (M7.5 to 7.7; 0.5 to 0.6 *g* a_{max}). Attenuation relationships for the accelerations of the 1886 event were also estimated from the study of liquefaction effects.

5. Ongoing seismic analyses indicate that very strong prehistoric ground shaking has occurred in the Wabash Valley, an area having no historical earthquakes exceeding M5.5. The authors' preliminary estimate of the earthquake magnitude that produced these feature is M7.5, with accelerations at least as high as 0.3 *g*.

ACKNOWLEDGMENTS

Funding for this research was provided by the National Earthquakes Hazards Reduction Program, administered by the U.S. Geological Survey. Gratitude for assistance is due S. F. Obermeier of the U.S. Geological Survey for his field work, field assistance, and review of this manuscript. A major debt of gratitude is also due P. J. and C. A. Munson of Indiana University for their invaluable assistance in the identification of potential study sites.

REFERENCES

1. Ishihara, K. Stability of Natural Soil Deposits During Earthquakes. In *Proceedings of the Eleventh International Conference on Soil Mechanics and Foundation Engineering*, San Francisco, Vol. 1, 1985, pp. 321–376.
2. Youd, T. L., and D. M. Perkins. Mapping of Liquefaction Severity Index. *Journal of the Geotechnical Engineering Division*, Vol. 113, No. 11, 1987, pp. 1374–1392.
3. Obermeier, S. F. *The New Madrid Earthquakes: An Engineering-Geologic Interpretation of Relict Liquefaction Features.* Professional Paper 1336-B. U.S. Geological Survey,1989, 114 pp.
4. Seed, H. B., K. Tokimatsu, L. F. Harder, and R. M. Chung. *The Influence of SPT Procedures in Soil Liquefaction Resistance Evaluations.* Report UBC/EERC-84/15. Earthquake Engineering Research Center, University of California, Berkeley, 1984.
5. Holzer, T. L., T. D. Youd, and T. C. Hanks. Dynamics of Liquefaction During the 1897 Superstition Hills, California Earthquake. *Science*, Vol. 244, April, 1989, pp. 56–59.
6. Seed, R. B., S. E. Dickenson, and I. M. Idriss. Principal Geotechnical Aspects of the 1989 Loma Prieta Earthquake. *Soils and Foundations, Japanese Society of Soil Mechanics and Foundation Engineering*, Vol. 31, No. 1, March 1991, pp. 1–26.
7. Tuttle, M., and K. T. Law. Liquefaction and Ground Failure Induced by the 1988 Saguenay, Quebec, Earthquake. *Canadian Geotechnical Journal*, Vol. 27, No. 5, 1990, pp. 580–589.

8. Schnabel, P. B., J. Lysmer, and H. B. Seed. *SHAKE, A Computer Program for Earthquake Response Analysis of Horizontally Layered Site.* Report EERC 72-12. Earthquake Engineering Research Center, University of California, Berkeley, Dec. 1972.
9. Youd, T. L. Mapping of Earthquake-Induced Liquefaction for Seismic Zonation. In *Proceedings of the Fourth International Conference on Seismic Zonation*, Earthquake Engineering Research Institute, El Cerrito, Calif., Vol. 1, 1991, pp. 111–147.
10. Ambraseys, N. N. Engineering Seismology: Earthquake Engineering and Soil Dynamics. *Journal of the International Association for Earthquake Engineering*, Vol. 17, 1988, pp. 1–105.
11. Obermeier, S. F., J. R. Martin, A. D. Frankel, T. L. Youd, P. J. Munson, C. A. Munson, and E. C. Pond. *Liquefaction Evidence for Strong Holocene Earthquake(s) in the Wabash Valley of Southern Indiana-Illinois, With a Preliminary Estimate of Magnitude.* Professional Paper 1536. U.S. Geological Survey, 1992, 279 pp.
12. Martin, J. R., and G. W. Clough. *Implications from a Geotechnical Investigation of Liquefaction Phenomena Associated with Seismic Events in the Charleston, SC Area.* Department of Civil Engineering, Virginia Polytechnic Institute and State University, Blacksburg, 1990, 414 pp.
13. Bollinger, G. A. Reinterpretation of the Intensity Data for the 1886 Charleston, South Carolina, Earthquake. In *Studies Related to the Charleston, South Carolina, Earthquake of 1886, A Preliminary Report.* Professional Paper 1028. U.S. Geological Survey, 1977, pp. 17–32.
14. Nuttli, O. W., G. A. Bollinger, and R. B. Herrmann. *The 1886 Charleston Earthquake—A 1986 Perspective.* Circular 985. U.S. Geological Survey, 1986, 116 pp.
15. Johnston, A. C. The Stable-Continental Region Earthquake Data Base. In *Methods for Assessing Maximum Earthquakes in the Central and Eastern United States* (Coppersmith et al., eds.), Project RP-2556-12, Electric Power Research Institute, Palo Alto, Calif., in press, 1992.
16. Chapman, M. C., M. S. Sibol, and G. A. Bollinger. *Investigation of Anomalous Earthquake Intensity Levels Along the Coastal Plain-Piedmont Boundary in South Carolina and Georgia.* Seismological Observatory Report. Virginia Polytechnic Institute and State University, Blacksburg, 1989, 70 pp.
17. Clough, G. W., and J. R. Martin. Geotechnical Setting for Liquefaction Events in the Charleston, South Carolina Vicinity. In *Proceedings of the H.B. Seed Memorial Symposium*, May 1990, pp. 313–334.
18. Dutton, C. E. The Charleston Earthquake of August 31, 1886. In *U.S. Geological Survey Annual Report, 1887–1888*, 1889, pp. 203–528.
19. Obermeier, S. F., F. E. Weems, and R. B. Jacobson. *Earthquake-Induced Liquefaction Features in the Coastal South Carolina Region.* Open-File Report 87-504. U.S. Geological Survey, 1987, 13 pp.
20. Obermeier, S. F., R. B. Jacobson, J. P. Smoot, R. E. Weems, G. S. Gohn, J. E. Monroe, and D. S. Powars. *Earthquake-Induced Liquefaction Features in the Coastal Setting of South Carolina and in the Fluvial Setting of the New Madrid Seismic Zone.* Professional Paper 1504. U.S. Geological Survey, 1990, 44 pp.
21. Amick, D., R. Gelinas, G. Maurath, R. Cannon, D. Moore, E. Billington, and H. Kemppinen. *Paleoliquefaction Features Along the Atlantic Seaboard.* Report NUREG/CR-5613. U.S. Nuclear Regulatory Commission, Washington, D.C., 146 pp., 1990.
22. Nuttli, O. W., and R. B. Herrmann. Consequences of Earthquakes in the Mississippi Valley. American Society of Civil Engineers Preprint 81-519, ASCE National Convention, St. Louis, Oct. 1981.
23. Hamilton, R. M., and A. C. Johnston (eds.) *Tecumseh's Prophecy—Preparing for the Next New Madrid Earthquakes.* Circular 1066. U.S. Geological Survey, 1990, 30 pp.
24. Youd, T. L., D. M. Perkins, and W. G. Turner. Liquefaction Severity Index Attenuation for the Eastern United States. In *Proceedings from the Second U.S.-Japan Workshop on Liquefaction, Large Ground Deformation, and Their Effects on Lifelines* (T. D. O'Rourke and M. Hamada, eds.), Technical Report NCEER-89-0032, State University of New York at Buffalo, 1989, pp. 438–452.
25. Braile, L. W., W. J. Hinze, J. L. Sexton, J. R. Keller, and E. G. Lidiak. Tectonic Development of the New Madrid Seismic Zone. In *Proceedings of the Symposium on the New Madrid Seismic Zone* (P. L. Gori and W. W. Hays, eds.), Open-File Report 84-770, U.S. Geological Survey, 1984, pp. 204–233.
26. Munson, P. J., C. A. Munson, N. K. Bleuer, and M. D. Labitzke. Distribution and Dating of Prehistoric Earthquake Liquefaction in the Wabash Valley of the Central U.S. *Seismological Research Letters*, Vol. 63, No. 2, 1992, pp. 337–342.
27. Andrus, R. D., K. H. Stokoe, and J. M. Roesset. Liquefaction of Gravelly Soil at Pence Ranch During the 1983 Borah Peak, Idaho Earthquake. In *Proceedings of the Fifth International Conference on Soil Dynamics and Earthquake Engineering*, Karlsruhe, Germany, 1991, pp. 251–262.

Publication of this paper sponsored by Committee on Engineering Geology.

Soil and Foundation Conditions and Ground Motion at Cypress Street Viaduct

G. NORRIS, R. SIDDHARTHAN, Z. ZAFIR, AND P. GOWDA

The Cypress Street viaduct, located some 100 km (60 mi) from the epicenter of the Loma Prieta, California, earthquake, suffered catastrophic structural damage during the 5 to 10 sec of strong shaking on October 17, 1989. Although much has been written about the structural details that ultimately led to the viaduct's failure, less has been presented relative to the possible contributing effect of the soil and foundations. The results of this study show the difference in the soils and foundations (spread footings and short end bearing piles in Merritt sand, abruptly changing to long friction piles in Bay mud) along the length of the viaduct and the possible difference in ground surface motions over the northern (Bay mud) versus the southern (Merritt sand) sections. Given the soil borings at Bents 61 and 97, the nonlinear variations in both the rotational and lateral pile group stiffnesses are assessed and presented for consideration. The lateral response is compared with the measured response from California Department of Transportation lateral pile group load tests. There is such a difference in the lateral and rotational stiffnesses of pile groups in the Merritt sand versus the Bay mud that, given the abrupt change in soil and foundation conditions between Bents 71 and 72, a dynamic analysis intending to show the progress and arrest of collapse along the length of the viaduct would need to take this into consideration. In regard to the stiffness evaluations, the authors considered the effect of developing porewater pressure in the Merritt sand and the choice of free-field versus near-field (or inertial interaction) strain for the evaluation of soil modulus values for stiffness calculations. The discussion in this paper covers subsurface conditions, site ground motions, the associated collapse, foundation types, soil properties, and porewater pressure buildup in the Merritt sand during the Loma Prieta earthquake.

The collapse of roughly a 1.25-km (¾-mi) length of the northern portion of the Cypress Street viaduct of the Nimitz Freeway (Interstate 880) during the Loma Prieta earthquake of October 17, 1989, claimed 40 lives. This double-decker structure, shown in Figure 1 (*1*), was designed in the early 1950s and built in the late 1950s; it was located some 100 km (60 mi) north of the earthquake epicenter. Figure 2 shows the location of the structure in relation to various areas that experienced liquefaction of the loose hydraulic sand fill employed in their construction (e.g., the Oakland harbor complex, the Alameda Naval Air Station, the approach to the east end of the Bay Bridge, and Treasure Island). Such nearby liquefaction suggests the possibility of developing porewater pressures due to unrealized liquefaction in the natural (Merritt) sand at the Cypress viaduct and its associated effect on the foundation stiffnesses (in the Merritt sand) during the earthquake.

Collapse of the structure started from Bent 112 in the north and progressed southward to Bent 63. It should be noted that up to Bent 70 the near-surface soil is Merritt sand, but it then switches to Bay mud over the northern portion of the site. Likewise, there was an abrupt switch in foundation type from spread footings and short end bearing piles in the Merritt sand to long friction piles through the Bay mud occurring between Bents 71 and 72. This suggests that the possible differences in the lateral and vertical-rotational foundation stiffnesses between successive bents may have affected the progressive collapse mechanism (i.e., the collapse was arrested between Bents 70 and 63 after a transition from one soil and foundation type to another). Further complicating such consideration is the possible difference in the ground surface motion over the northern (Bay mud) versus the southern (Merritt sand) portions of the site.

Questions related to the nature of soil and foundation behavior at the Cypress Street viaduct are addressed in this and an accompanying paper by Norris et al. in this Record. In this paper subsurface conditions, site ground motions, the associated collapse, foundation types, soil properties, and porewater pressure buildup in the Merritt sand during the Loma Prieta earthquake are discussed. An earlier paper by Norris (*2*) provides an overview of foundation stiffness evaluation that is the basis for the assessment of the lateral and vertical-rotational stiffnesses at the Cypress Street viaduct presented in the following paper.

SUBSURFACE CONDITIONS, SITE GROUND MOTIONS, AND FOUNDATION TYPE

Figure 2 [after Seed et al. (*3*)] provides a plan view of the viaduct in relation to Oakland Outer Harbor to the west, Lake Merritt to the east, the approach to the Bay Bridge to the north, and the Alameda Naval Air Station to the south. In 1860 the Oakland shoreline was the edge of the Merritt sand deposit (*Qal*, Figure 3). Most of that part of modern-day Oakland to the west of this old shoreline is loose dumped or hydraulic sand fill placed in the late 1800s and early 1900s on top of the Bay mud (*Qm*, Figure 3). Therefore, the northern portion of the Cypress viaduct passed over what was once mud flats.

G. Norris, R. Siddharthan, and Z. Zafir, Department of Civil Engineering/258, University of Nevada, Reno, Nev. 89557. P. Gowda, 25 Poncetta Drive #118, Daly City, Calif. 94015.

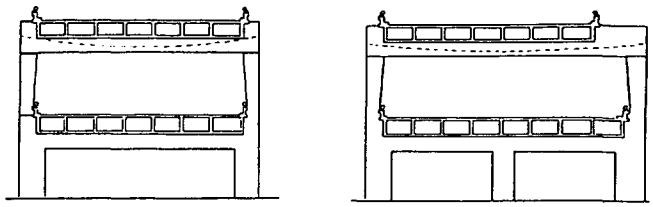

FIGURE 1 Typical two- and three-column bents at Cypress Street viaduct (*1*).

The importance of this difference in the near-surface soils in terms of possible differences in ground surface motions was amply demonstrated by the Lamont-Doherty seismological team [see, e.g., Earthquake Engineering Research Institute Report 89-03 (*4*)], who recorded aftershock motions on the Bay mud, the Merritt sand, and rock outcrop (representing bedrock motion beneath the length of the viaduct). Figure 3 compares the motion from this magnitude M4 aftershock as recorded at Stations S1, S3, and S4 and the location of these stations in relation to the viaduct and the transition from one soil type to another. Of course, the difference in amplification in going from rock (S4) to the top of Bay mud (S1) versus rock (S4) to the top of Merritt sand (S3) will not be the same (necessarily) at the higher magnitude of the Loma Prieta earthquake (M7) because of the soil's nonlinear effects.

Figure 4 shows that portion of the viaduct where the upper deck collapsed onto the lower deck. Such action progressed from Bent 112 on the northern end to Bent 63 in the Merritt sand. (Between Bents 96 and 97 the upper deck did not collapse because of the skew angle of the deck passing over 26th Street between these supports.) The collapse started at Bent 112, where the lower deck came down to the ground, and was arrested at the expansion joint between Bents 62 and 63, possibly in part because of additional lateral support to the southern section from ramps joining the upper and lower decks (and a third lower deck column and foundation) between Bents 56 and 62. However, the contribution of any change in the ground surface motion (mentioned above) and differences in the lateral and rotational stiffnesses due to an abrupt change in the soil and foundation type (on crossing over from Bay mud to Merritt sand) is probably of equal or greater importance.

Figure 5 is a profile of the near-surface soil in the vicinity of the transition from Merritt sand to Bay mud; the dots indicate pile tip elevations. It should be noted that up to Bent 35, shallow foundations were used in the Merritt sand. As shown, the Merritt sand thins out entirely between Bents 69 and 80, and pile foundations abruptly change from short end bearing piles in the Merritt sand at Bent 71 to long friction piles in Bay mud at Bent 72. This is more dramatically shown in Figure 6. [The piles are pipe piles 0.32 m (12¾ in.) outside diameter, 1 cm (⅜ in.) thick, backfilled with concrete.]

SOIL PROPERTIES AND SEISMIC POREWATER PRESSURE IN SAND

After the earthquake, the California Department of Transportation (Caltrans) undertook exploratory borings at select locations along the length of the viaduct that included two

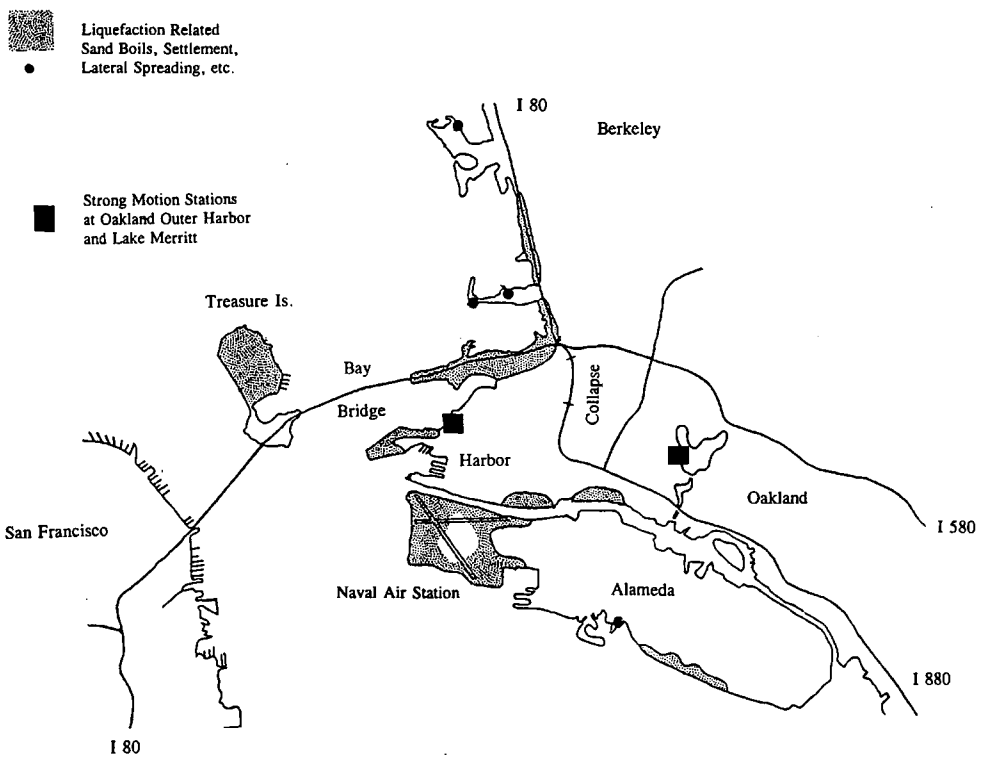

FIGURE 2 Cypress Street viaduct in relation to nearby areas of liquefaction (*3*).

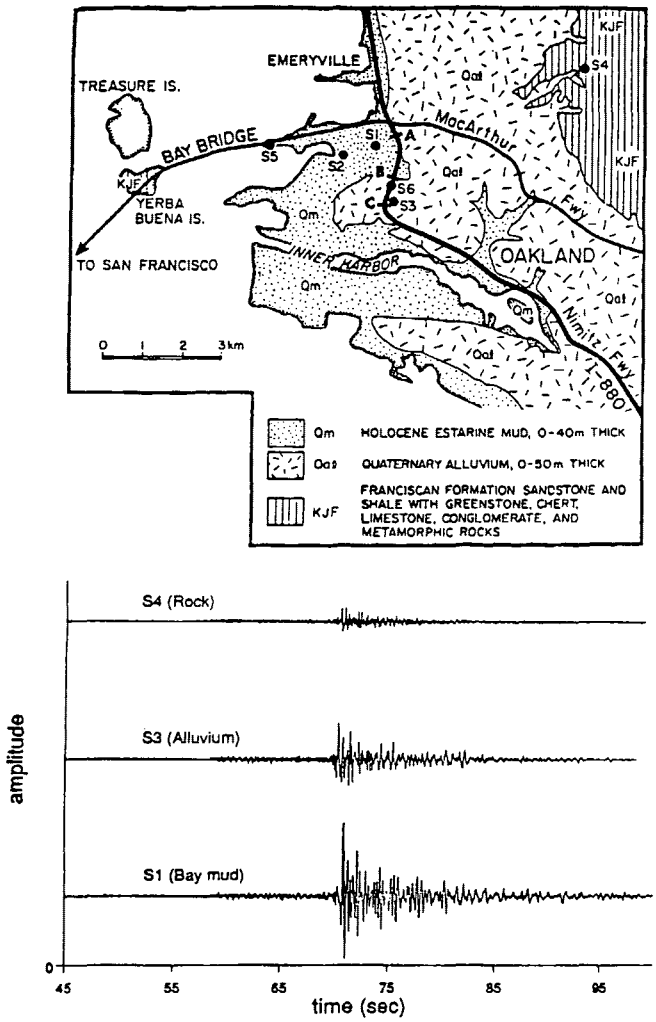

FIGURE 3 Lamont-Doherty aftershock accelerometer stations and records on Merritt sand, Bay mud, and rock (*4*).

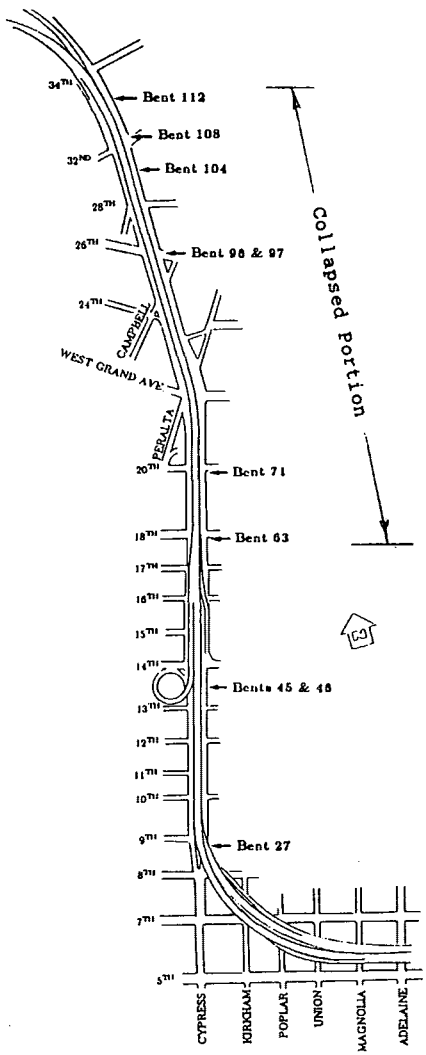

FIGURE 4 Plan view of Cypress Street viaduct showing collapsed portion (*1*).

deep holes to Franciscan greywacke at 150 m (500+ ft) depth. Figures 7 and 8 are the shallow depth logs at Bents 61 (in Merritt sand) and 97 (Bay mud) corresponding to the location of the Caltrans lateral pile group load tests undertaken subsequent to the demolition of the superstructure. The Merritt sand is a Wisconsin-age aeolian sand, and the Bay mud referred to here at the Cypress Street viaduct is actually a shallow estuarine deposit composed of intertongues of Young Bay mud, Temescal formation alluvium, and Yerba Buena mud (*5*).

Figure 9 is a characterization of the variation in vertical effective stress σ'_{vo} with depth at Bent 61, along with an estimated relative density D_r profile as established from the given Standard Penetration Test blowcounts (N) and an available correlation (*6*). A pile cap and a short end bearing pile are shown to the side for reference. Figure 10, on the other hand, is the estimated undrained shear strength variation for the Bay mud at Bent 97 established using Terzaghi's suggested correlation with blowcount, S_u (kPa) = 100 N (blows per 0.3 m)/15; that is, S_u (kips/ft^2) = N (blows per ft)/7.5. Such undrained strength values are in reasonable agreement with the few undrained strengths given on the log established from pocket penetrometer readings.

Although there were possible differences in ground surface acceleration at the top of the Merritt sand versus the Bay mud at the Cypress Street viaduct (as demonstrated in Figure 3 from aftershock response), there were no records at the site during the Loma Prieta earthquake. The nearest permanent strong-motion recording stations yielding records during the earthquake were in a two-story structure at Lake Merritt and at Oakland Outer Harbor (see Figure 2). Free-field surface records at these locations are shown in Figure 11. Although the Lake Merritt station is in Merritt sand and the Oakland Outer Harbor is in loose sand fill over Bay mud, these records are quite similar; they are slightly out of phase because of the (wave) travel time between them. The Oakland Outer Harbor peak acceleration was 0.29 g, whereas that of the Lake Merritt record was 0.26 g. Applying weighting techniques after Seed et al. (*7*), these motions yield approximately four equivalent cycles N_{eq} of a uniform amplitude of basically 0.2 g acceleration (0.65 of the peak acceleration). Since it is not clear that

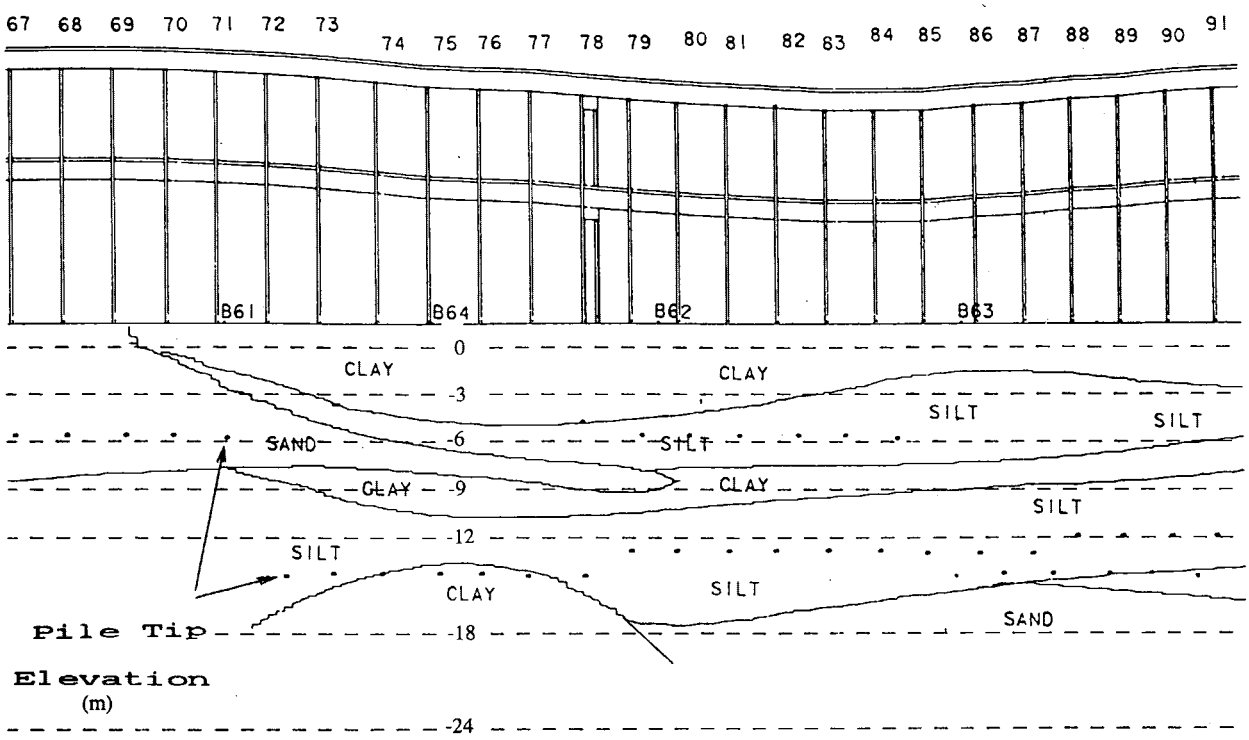

FIGURE 5 Soil conditions in transition region (*courtesy of D. Rogers*).

such motion would be representative of motions at the ground surface on the Merritt sand or the Bay mud at the Cypress Street viaduct (or if there would in fact be a difference at this higher-magnitude event), it was decided to use the given uniform equivalent motion as representative of the top of the Merritt sand to assess the possible buildup of porewater pressure causing a reduced effective stress as compared with the initial σ'_{vo} variation shown in Figure 9.

Figure 9 shows the bulb of excess porewater pressure (u_{xs}) and the reduced vertical effective stress that develops by the end of strong shaking (N_{eq} = four cycles) within the depth of the short end bearing piles at Bent 61, which would in turn affect the vertical load-carrying capacity of the piles and hence their axial stiffness. (The shaft capacity of a pile is a function of the area under the vertical effective stress diagram, whereas point capacity is related to the vertical effective stress at the pile tip.)

The means by which such u_{xs} is assessed is shown schematically in Figure 12. If at a given depth one compares the stress ratio induced by the earthquake (*8*) to the curve for the given material representing the stress ratio to cause liq-

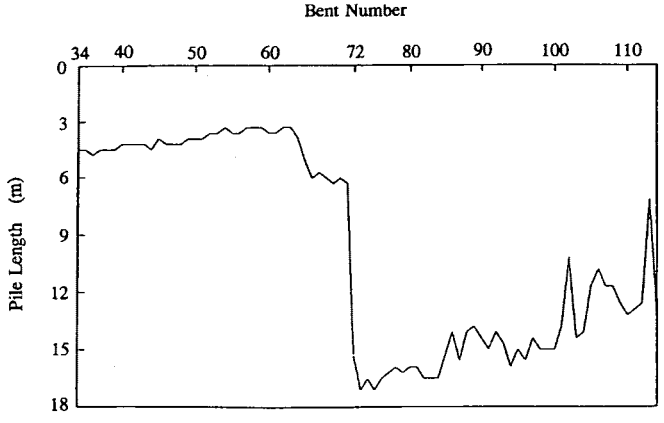

FIGURE 6 Pile length by bent location (*1*).

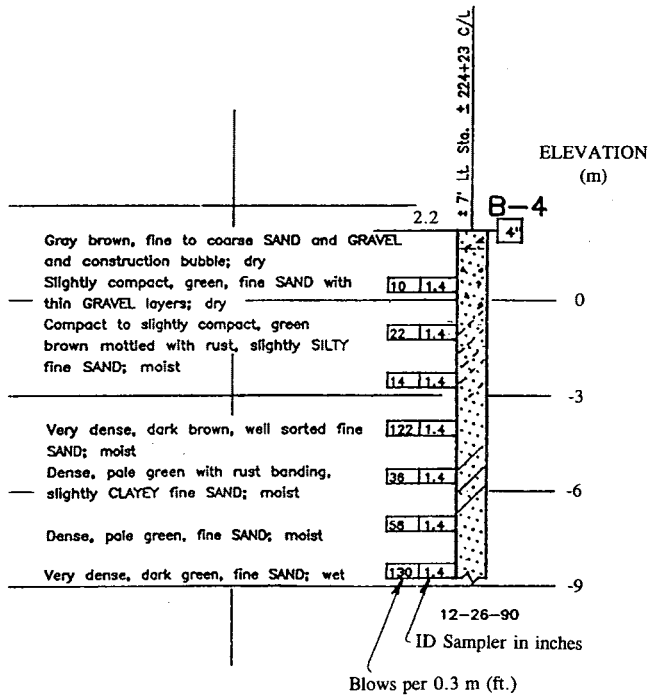

FIGURE 7 Boring log at Bent 61 in Merritt sand (*courtesy of Caltrans*).

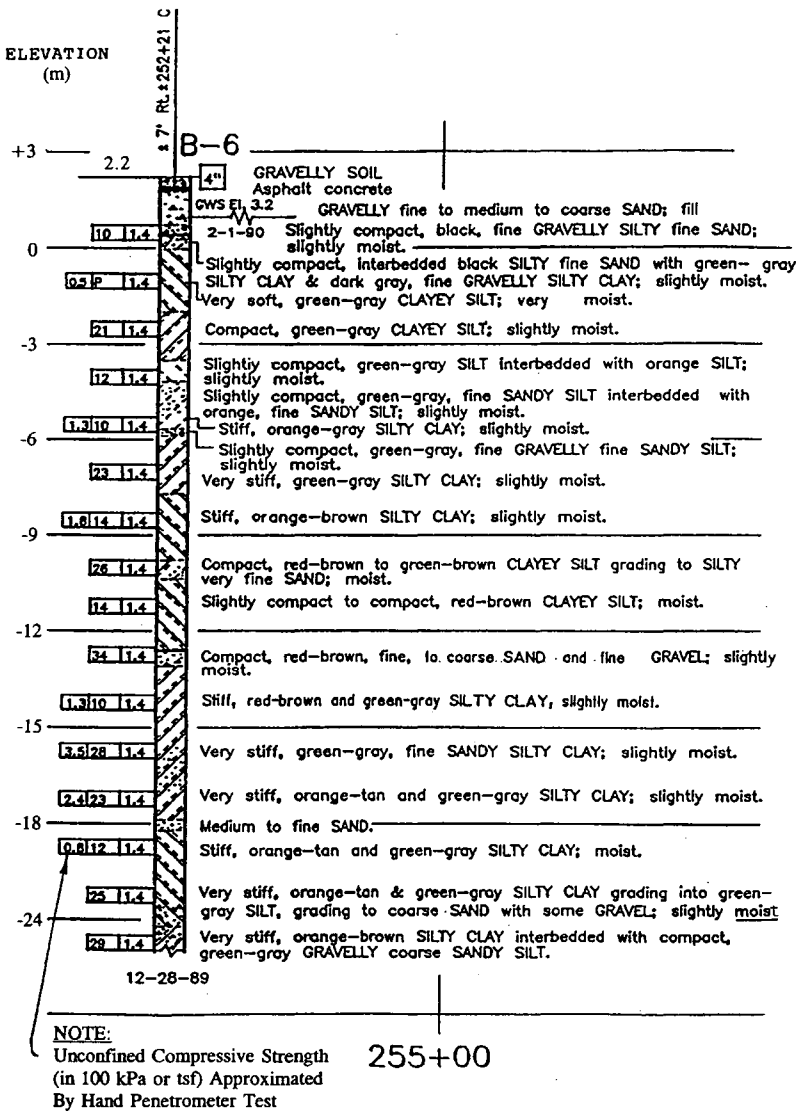

FIGURE 8 Boring log at Bent 97 in Bay mud (*courtesy of Caltrans*).

uefaction R_{liq}, and R_{eq} at its (uniform) equivalent number of cycles ($N_{eq} = 4$) is less (vertically) than R_{liq}, then there will be no liquefaction (see Figure 12a):

$$R_{eq} = 0.65(\sigma_{vo}/\sigma'_{vo})(a_{max}/g)r_d \quad (1)$$

where

σ_{vo}, σ'_{vo} = total and (original) effective stresses at the depth of interest,
$0.65a_{max}/g$ = uniform equivalent acceleration as a fraction of gravity, and
r_d = correction factor for deformable (soil) versus rigid body behavior.

However, there will still be porewater pressure buildup equal to

$$u_{xs} = r_u\sigma'_{vo} \quad (2)$$

and a reduced vertical effective stress

$$\sigma'_v = \sigma'_{vo} - u_{xs}$$

or

$$\sigma'_v = \sigma'_{vo}(1 - r_u) \quad (3)$$

where the pore pressure ratio r_u is given in Figure 12b [after Seed et al. (*8*)] as a function of the ratio N_{eq}/N_{liq}. N_{liq} is the number of equivalent uniform cycles to cause liquefaction at the stress ratio of the earthquake ($R_{liq} = R_{eq}$) as shown by the horizontal line in Figure 12a. The liquefaction curve of Figure 12a should represent the corrected blowcount N_1 and percentage fines of the sand at the depth in question. Figure 13 gives curves for different blowcounts N_1 and percentage fines as obtained from cross-plotting the Seed et al. (*8*) curves (converting magnitude M into equivalent number of cycles)

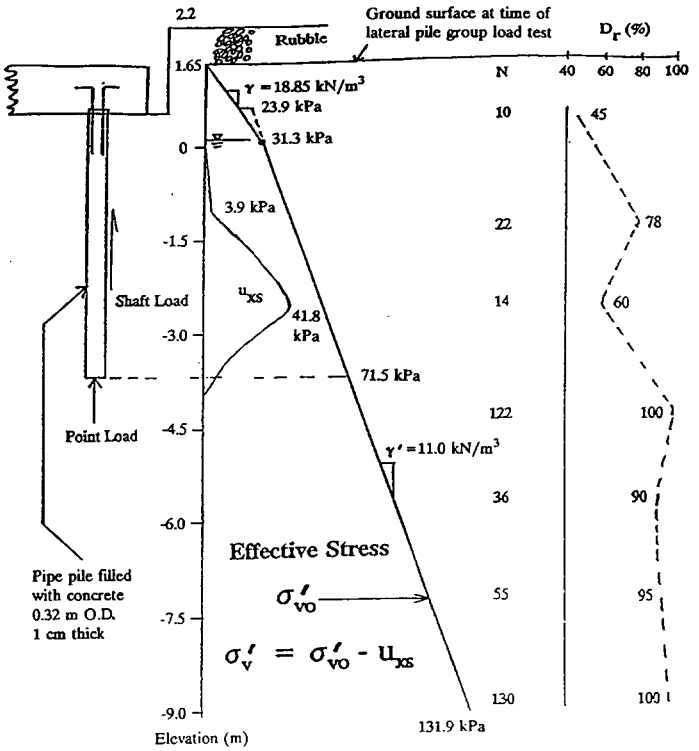

FIGURE 9 Vertical effective stress and relative density profiles at Bent 61 with the short end bearing pile shown for reference. Note: For purposes of later comparison, the ground surface, the water table, and hence σ'_{vo} shown here reflect conditions at the time of Caltrans lateral pile group tests, and u_{xs} and σ'_v reflect Loma Prieta motions (N_{eq} = 4) relative to these conditions. At the time of the earthquake, there was an added 2 to 3 ft of cover over the pile cap and the water table location may have been different.

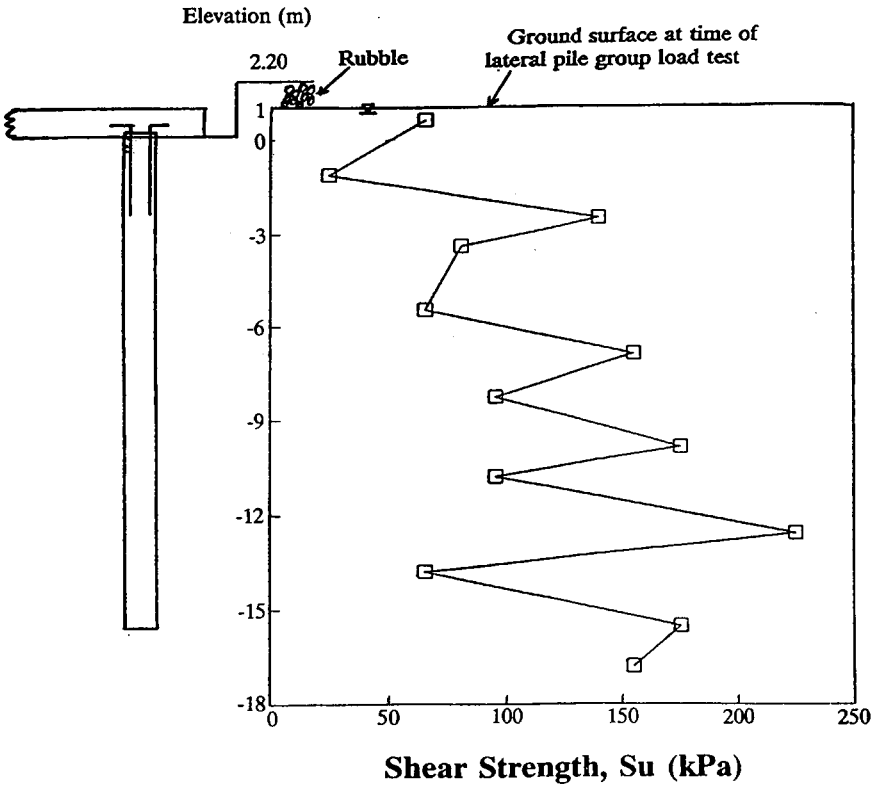

FIGURE 10 Undrained shear strength S_u profile at Bent 97.

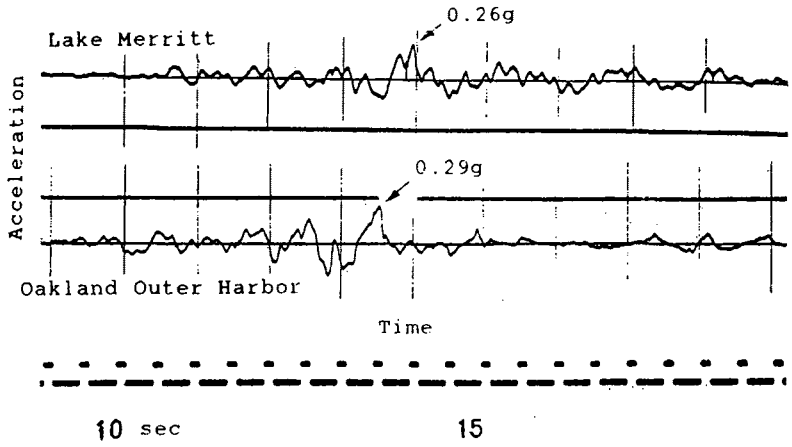

FIGURE 11 Strong shaking portion of California Strong Motion Instrumentation Program (CSMIP) free-field records at Oakland Outer Harbor and Lake Merritt.

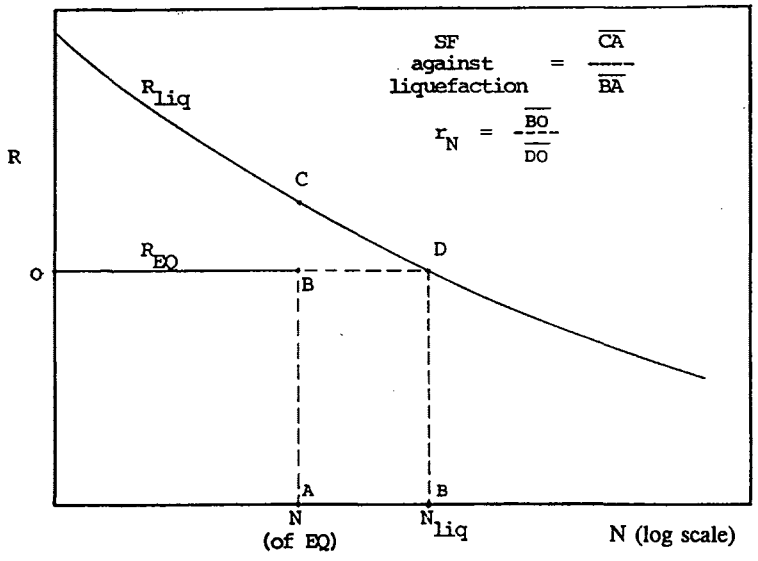

a)

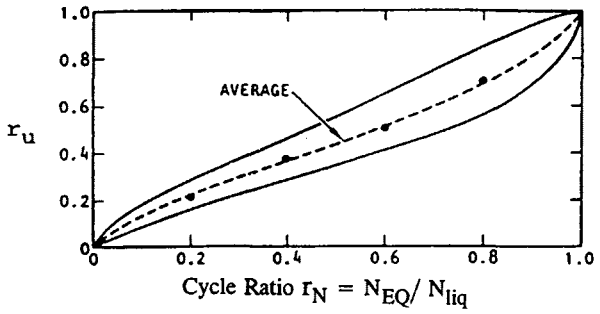

b)

FIGURE 12 Liquefaction curve (*a*) showing earthquake-induced stress ratio versus stress ratio to cause liquefaction and number of cycles to liquefaction at the earthquake-induced stress ratio and (*b*) pore pressure coefficient versus cycle ratio.

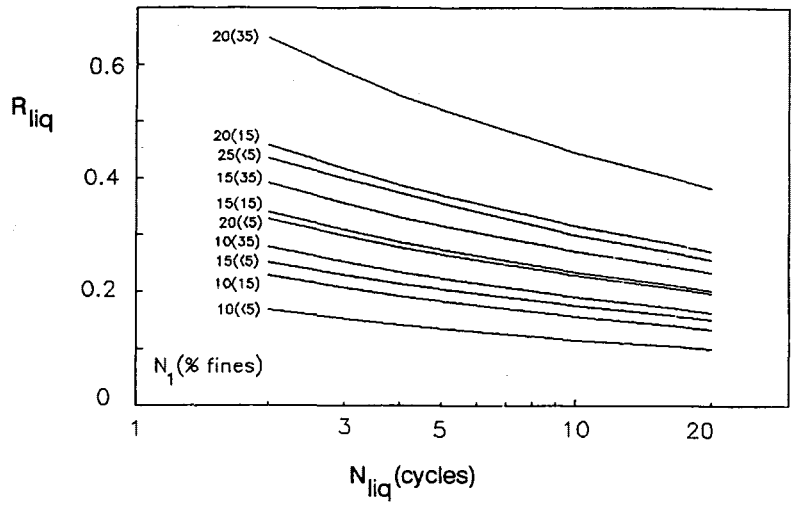

FIGURE 13 Liquefaction curves for different corrected blowcount and percent fines.

and applying a correction factor for the percentage fines (15 and >35 percent) as derived from the work of Seed et al. (*9*). The u_{xs} bulb shown in Figure 11 is the variation with depth taking the sand to be clean (<5 percent fines).

As should be noted, even though there was no liquefaction at the site, there was porewater pressure buildup in the zones of lower relative density below the water table, which by the end of strong shaking would have caused a reduced pile capacity as reflected by the reduced area of the vertical effective stress diagram. Such reduced capacity, as well as the corresponding reduced vertical pile stiffness, will be evaluated in the following paper in this Record. Although the pore pressure bulb shown in Figure 9 is for four cycles corresponding to the end of strong shaking, similar bulbs might be assessed at fewer cycles corresponding to earlier times in the record. Such time-dependent development of excess porewater pressure and the associated time-affected pile capacity and reduced pile stiffness have been demonstrated for the Meloland Overcrossing in the 1979 Imperial Valley earthquake (*10*, *11*), where (assessed) liquefaction occurred in up to three different layers at different times in the record. Here, where liquefaction did not occur, it will suffice for purposes of discussion to consider only the response at the end of strong shaking.

It should be noted that developing porewater pressures might also affect the lateral stiffness of the piles. However, laterally loaded piles develop resistance from the soil near the pile top, and from Figure 9 it would appear that the u_{xs} pressure bulb (or the majority of it) falls just below this zone of soil support. Therefore, the evaluation of lateral stiffness at Bent 61 in the following paper will be made corresponding to the effective stress profile reflected by the σ'_{vo} variation of Figure 9. Likewise, there would have been no effect on the axial and lateral stiffness of the piles in the Bay mud for these few equivalent cycles of shaking. Luckily, the duration of the Loma Prieta earthquake was much shorter than the normal M7 earthquake where an N_{eq} = 12 cycles is more typical.

SUMMARY

Subsurface conditions, site ground motions and the associated superstructure collapse, foundation types, soil properties, and porewater pressure buildup in the Merritt sand (during the Loma Prieta earthquake) at the Cypress Street viaduct have been discussed. In the following paper, methods for assessing the lateral and vertical-rotational stiffnesses [methods reviewed by Norris (*2*)] are applied to assess stiffnesses of the pile foundations at Bents 61 and 97.

ACKNOWLEDGMENT

The funding for this study was provided by the U.S. Department of Energy as part of a larger study on pile foundation stiffnesses for the seismic modeling of railroad and highway bridges. Such support is gratefully acknowledged.

REFERENCES

1. Nims, D. K., E. I. Miranda, I. D. Aiken, A. S. Whitaker, and V. V. Bertero. *Collapse of the Cypress Street Viaduct as a Result of the Loma Prieta Earthquake.* Report UCB/EERC 89-16. Earthquake Engineering Research Center, University of California, Berkeley, 1989.
2. Norris, G. M. Overview of Evaluation of Pile Foundation Stiffnesses for Seismic Analysis of Highway Bridges. In *Transportation Research Record 1336*, TRB, National Research Council, Washington, D.C., 1992, pp. 31–42.
3. Seed, R. B., S. E. Dickerson, M. E. Riemer, J. D. Bray, N. Sitar, J. K. Mitchell, I. M. Idriss, R. E. Kayen, A. Kropp, L. F. Harder, and M. S. Power. *Preliminary Report on the Geotechnical Aspects of the October 17, 1989 Loma Prieta Earthquake.* Report UCB/EERC 90-15. Earthquake Engineering Research Center, University of California, Berkeley, 1990.
4. *Loma Prieta Earthquake, October 17, 1989: Preliminary Reconnaissance Report.* EERI Report 89-03. Earthquake Engineering Research Institute, El Cerrito, Calif., 1989.

5. Rogers, J. D. Site Stratigraphy and Its Effects on Soil Amplification in the Greater Oakland Area During the October 17, 1989 Loma Prieta Earthquake. In *Proceedings of the Second International Conference on Recent Advances in Geotechnical Engineering and Soil Dynamics,* St. Louis, 1991.
6. *Design Manual: Soil Mechanics*. NAVFAC DM-7.1. U.S. Government Printing Office, Washington, D.C., 1982, pp. 14, 88, 149.
7. Seed, H. B., I. M. Idriss, F. Makdisi, and N. Banerjee. *Representation of Irregular Stress Time Histories by Equivalent Uniform Stress Series in Liquefaction Analyses*. Report EERC 75-29. Earthquake Engineering Research Center, University of California, Berkeley, 1975.
8. Seed, H. B., I. M. Idriss, and I. Arango. Evaluation of Liquefaction Potential Using Field Performance Data. *Journal of the Geotechnical Division*, ASCE, Vol. 109, No. 3, March, 1983, pp. 458–482.
9. Seed, H. B., K. Tokimatsu, L. F. Harder, and R. M. Chung. *The Influence of SPT Procedures in Soil Liquefaction Resistance Evaluations*. Report UCB/EERC-84/15. Earthquake Engineering Research Center, University of California, Berkeley, 1984.
10. Norris, G. M. Nonstable Rotational Stiffness of a Pile Group. In *Proceedings of the Third U.S. National Conference on Earthquake Engineering*, Earthquake Engineering Research Institute, Vol. 1, 1986, pp. 635–646.
11. Norris, G. M. A Seismic Analysis: Meloland Overcrossing During the 1979 Earthquake. In *Geotechnical Special Publication 17: Centrifugal Models and Field Performance*, ASCE, 1988, pp. 88–117.

Publication of this paper sponsored by Committee on Foundations of Bridges and Other Structures.

Seismic Pile Foundation Stiffnesses at Cypress Street Viaduct

G. NORRIS, R. SIDDHARTHAN, Z. ZAFIR, AND P. GOWDA

Given the soil borings, the estimated soil properties, the free-field ground surface motions (at strong-motion stations on either side of the Cypress Street viaduct in Oakland, California), and the assessed buildup in porewater pressure in the Merritt sand discussed in the preceding paper in this Record, the nonlinear variation in the lateral and vertical-rotational pile foundation stiffnesses at Bents 61 (in Merritt sand) and 97 (in Bay mud) is established on the basis of the methodology outlined in 1992 by Norris. Assessed lateral behavior is compared with observed response from the California Department of Transportation (Caltrans) lateral pile group load tests at these bents. Differences between stiffnesses corresponding to conditions reflecting the Caltrans tests and those applicable during the Loma Prieta earthquake are discussed. Likewise, differences between the methodology used here and that reflected by FHWA and the Applied Technology Council are pointed out.

Structural dynamic modeling of a highway bridge requires knowledge of the lateral and vertical-rotational stiffnesses of its foundations, which are typically pile foundations. Uncoupled lateral and vertical-rotational pile group stiffnesses are in turn a function, respectively, of the lateral and vertical responses of the individual piles, which can be evaluated via so-called *p-y* and *t-z* analyses. [See the paper by Norris (*1*) for a general overview of such analysis, with reference to case studies, for both nonliquefying and liquefying soil conditions.] It is such lateral and vertical-rotational pile foundation stiffnesses in Merritt sand (at Bent 61) and in Bay mud (at Bent 97) at the Cypress Street viaduct that are sought here.

Unfortunately for the bridge engineer, these stiffnesses are nonlinear—that is, they are displacement or rotation dependent—and a linear dynamic analysis of a bridge will require the choice of boundary element spring stiffnesses that are compatible with the resulting relative displacements or rotations. This means that given the nonlinear variation in the stiffnesses (e.g., at Bents 61 and 97), the bridge engineer must assume a set of stiffness values for a linear model and repeat the dynamic analysis, supplying a new set of stiffness values each time, until the resulting relative displacements yield stiffness values that match the assumed set of values. It is only in this fashion that one would be able to assess the progressive failure of the Cypress Street viaduct, which occurred over just the northern portion of its length.

Although such analysis will require several iterations, unless it is undertaken, correct determination of the distribution of (seismic) load to the structure, the acceleration on the structure, or the forces in the piles (i.e., the shears at the pile tops and from that the maximum moments in the piles) cannot be made. This is clearly demonstrated in a parallel analysis of the nearby Oakland Outer Harbor Wharf (*2*).

G. Norris, R. Siddharthan, and Z. Zafir, Department of Civil Engineering/258, University of Nevada, Reno, Nev. 89557. P. Gowda, 25 Poncetta Drive #118, Daly City, Calif. 94015.

LESSONS LEARNED FROM ASSESSED VERSUS OBSERVED RESPONSE OF OAKLAND OUTER HARBOR WHARF

The California Strong Motion Instrumentation Program (CSMIP) records for the instrumented Oakland Outer Harbor Wharf, located 1.6 km (1 mi) west of the Cypress Street viaduct, provide very important data for the purpose of understanding pile foundation response during an earthquake.

Although the piles at the Oakland Outer Harbor Wharf are different [0.46 m (18 in.) square free-standing precast concrete piles at large spacing] from those at the Cypress Street viaduct, they derive their lateral resistance from a surface layer of Bay mud (as do piles at Bent 97 of the Cypress Street viaduct) and their vertical resistance from point bearing in an underlying dense sand (similar to the piles at Bent 61 in Merritt sand). Therefore, there is something to be gained in the present consideration of foundation response at the Cypress Street viaduct from this more detailed study of the Oakland Outer Harbor Wharf.

In work undertaken by the authors relative to the Oakland Outer Harbor Wharf (*2*), it was found that using free-field motion input and (assessed) compatible lateral and vertical pile stiffnesses, a linear structural dynamic model is capable of providing computed motions on the deck of the wharf that nearly perfectly match the recorded accelerations on the structure. On the other hand, using stiffnesses that are too high (e.g., assuming fixed foundations) causes an assessed peak acceleration (0.58 *g*) twice the recorded acceleration and shear and tensile forces at the head of the critical pile almost three times that of the compatible stiffness solution. Similar combinations of lateral and vertical stiffnesses that are too high or low (as compared with displacement-compatible values) cause poor predicted responses.

An important point in the evaluation of the compatible stiffnesses is that the soil modulus values (Young's *E* or shear modulus *G*) employed in such assessment should be chosen in relation to the governing strain condition in the soil. At present, FHWA (*3*) and Applied Technology Council (ATC) (*4*) recommendations in regard to this matter are at odds. FHWA would have the engineer assess stiffnesses on the basis of traditional *p-y* and *t-z* approaches, where pile responses are a function of the relative displacements, as if the soil immediately surrounding the foundation (the near-field soil),

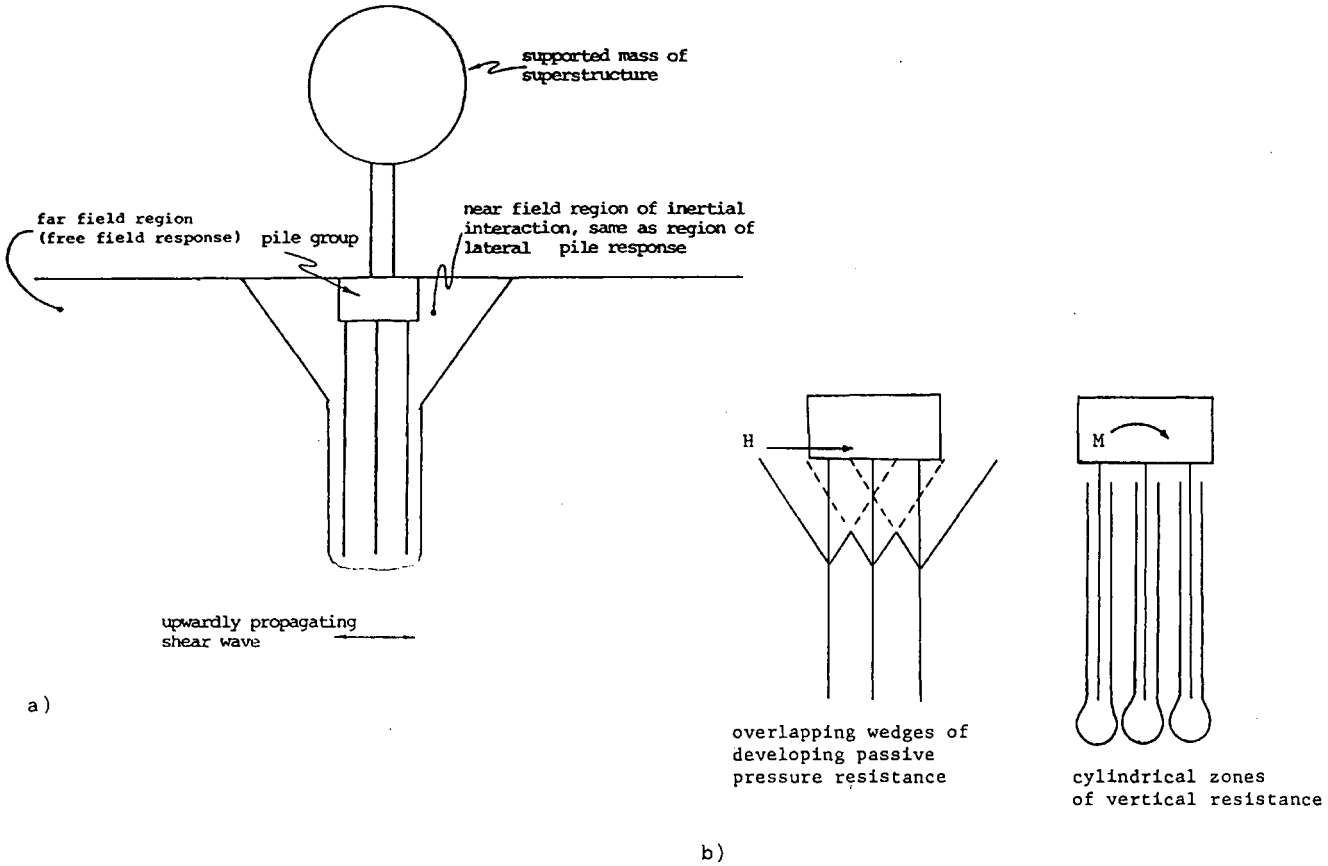

FIGURE 1 (*a*) **Near- versus far- (i.e., free-) field soil regions and** (*b*) **differing near-field (or inertial interaction) soil regions for lateral and vertical pile response.**

as shown in Figure 1a, were moving and the free-field soil (also called the far-field soil) were not. During seismic excitation, this would not be the case. ATC, on the other hand, would have the engineer use soil modulus values based on the level of the free-field strain, as if there were no relative motion in the near-field soil (i.e., the near-field soil moves in an identical manner to the free-field soil).

Of course, the appropriate procedure would be to take the modulus values in the associated near-field soil region, as shown in Figure 1b, as a function of the total strain (free-field plus relative, with due regard to phase differences). However, an expedient that would be more reasonable than either the FHWA or ATC approaches would be to use the larger of the two strains (free-field or relative) in the near-field soil region, that is, assume that either one or the other dominates. However, since the governing relative strain is a function of the level of the inertial interaction response of the superstructure, the engineer does not automatically know which is the larger. Nevertheless, this approach can be accommodated by showing the stiffness, determined as a function of the relative displacement or strain, with a superposed cutoff where the relative displacement or strain would be less than the free-field value.

Figure 2 is such a plot of the nonlinear variation in the vertical pile stiffness at the Oakland Outer Harbor Wharf showing a cutoff at 350 kN/mm (2,000 kips/in.) at a relative vertical pile head movement of 0.75 mm (0.03 in.), corresponding to the equivalent free-field shear strain of 3×10^{-2} percent in the dense sand and 2×10^{-1} percent in the overlying Bay mud. The computer program SHAKE (*5*) was used to obtain these shear strains given the free-field ground surface acceleration record shown in Figure 11 of the preceding paper in this Record. The shear moduli, G, of the soils in the *t-z* program were then limited to the corresponding values from the SHAKE program, resulting in a constant vertical pile head stiffness (350 kN/mm) for relative pile head displacements less than 0.75 mm (i.e., the free-field strain dominates) and a diminishing stiffness at successively greater displacements (i.e., the near-field or inertial interaction strain dominates). By contrast, the FHWA approach would have the stiffness increase at lower displacements (<0.75 mm), whereas the ATC approach would have the stiffness remain constant at 350 kN/mm (i.e., a horizontal line) across all levels of relative displacement. It should be pointed out that in the case of the Oakland Outer Harbor Wharf, the compatible solution resulted in the vertical pile stiffnesses falling (as different points for differently loaded piles) on this horizontal cutoff of 350 kN/mm, whereas the compatible horizontal stiffnesses for all piles fell on their appropriate curve, to the right of the free-field cutoff. In other words, it was the free-field

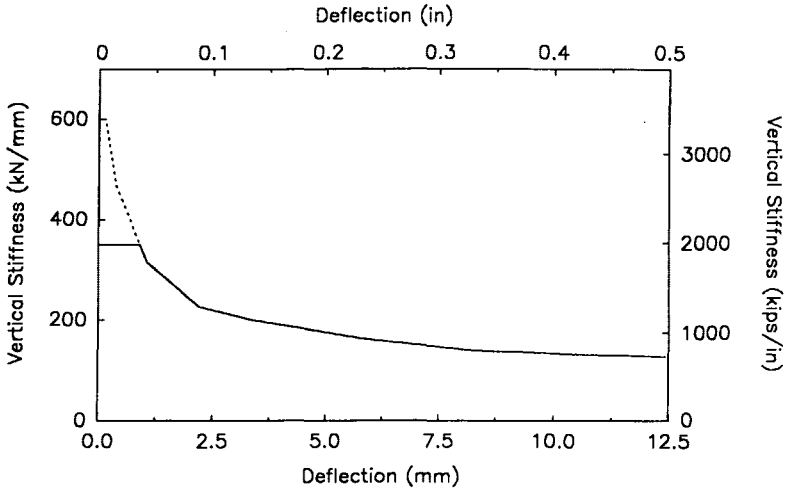

FIGURE 2 Vertical pile stiffness variation for 0.46-m (18-in.) square prestressed concrete piles at Oakland Outer Harbor Wharf during the Loma Prieta earthquake.

strain that governed in the case of the vertical response of the piles and the relative (near-field) strain that governed in the case of the lateral response of the piles.

In the following sections, the vertical-rotational and the lateral response of pile foundations at Bents 61 and 97 of the Cypress Street viaduct are established and compared.

VERTICAL-ROTATIONAL STIFFNESS

Figure 3a and b gives the backbone load-settlement curves assessed for the short end bearing pile in Merritt sand and the long friction pile in the Bay mud at Bents 61 and 97, respectively, on the basis of the soil conditions characterized in Figure 9 (both with and without porewater pressure buildup in the Merritt sand) and Figure 10 of the preceding paper.

The alpha method (*6*), using Tomlinson's average curve for all piles, was used to assess the capacity of the pile [623 kN (140 kips)] in Bay mud. Ramberg-Osgood fitting parameters for the t-z curves and the point load-displacement Q_p-z_p curve were employed relative to the different segments used to assess the undrained capacity of the pile in Bay mud. Given the Ramberg-Osgood fitting parameters for the backbone t-z and Q_p-z_p responses, the unload-reload fitting parameters are automatically known. Such parameters and a very simple t-z analysis program are presented elsewhere (*7*) for the reader's reference relative to such treatment of the pile in the Bay mud.

The Nordlund and Thurman method (*8*) was used to assess the ultimate capacity of the pile in sand [512 kN (115 kips)] based on an estimated drained friction angle of 37 degrees at pile point (and other values varying by pile segment along the pile length). The correlation appearing in NAVFAC DM-7.1 (*9*) was used to establish ϕ from D_r. (The variation in D_r is shown in Figure 9 of the preceding paper.) The t-z analysis used to assess the backbone and unload-reload responses of a pile in the Merritt sand is explained in detail in an associated report (*10*).

The reader should note the difference in the backbone curves of Figure 3b. The curve for the pile under developing porewater pressure conditions (N_{eq} = 4 cycles, corresponding to the end of strong shaking) in clean sand was assessed in the same way as the original curve except that the reduced level of vertical effective stress ($\sigma_{v'} = \sigma_{v'o} - u_{xs}$) was used in place of the original value $\sigma_{v'o}$ (see Figure 9 of the preceding paper). The reduction in effective stress affects the shaft resistance of only a few pile segments. Since point resistance contributes 423 kN (95 kips) of the total 512-kN (115-kip) capacity, such reduction in the shaft resistance [89 kN (20 kips) reduced to 45 kN (10 kips)] does not appear to be significant. However, the fact that the shaft resistance is fully mobilized well before point resistance can build up means that even this small loss in capacity has a noticeable effect in terms of the vertical unload-reload stiffness variation, as discussed below.

Figure 4 shows the unload-reload vertical pile stiffness variations for Bents 97 and 61. The stiffness k_v is simply the ratio of pile head load change ΔQ to the pile head displacement Δz, as discussed by Norris (*1*). The difference in stiffness of piles at Bent 61 with (Figure 4c) and without (Figure 4b) porewater pressure buildup is due to the loss in shaft capacity, which is felt at low levels of deflection because of the early mobilization of the shaft as compared with point resistance. Such difference in response diminishes at higher levels of deflection because of the greater mobilization of the very large point resistance, which was not affected by porewater pressure buildup.

It is important to point out that no cutoffs have been shown on these curves corresponding to the level of free-field strain (see Figure 2) because no free-field response analysis has been undertaken for the Cypress Street viaduct. (Recall from earlier discussion of the Oakland Outer Harbor Wharf that equivalent free-field strains in the dense sand and the overlying layer of Bay mud were almost an order of magnitude different for the same ground surface acceleration.) Therefore, the cutoffs would most likely occur at different values of axial pile displacement for curves in Figure 4a versus those in Figure 4b and c.

Figure 5 shows the transverse stabilized rotational stiffnesses of two similar groups at Bents 61 and 97 established

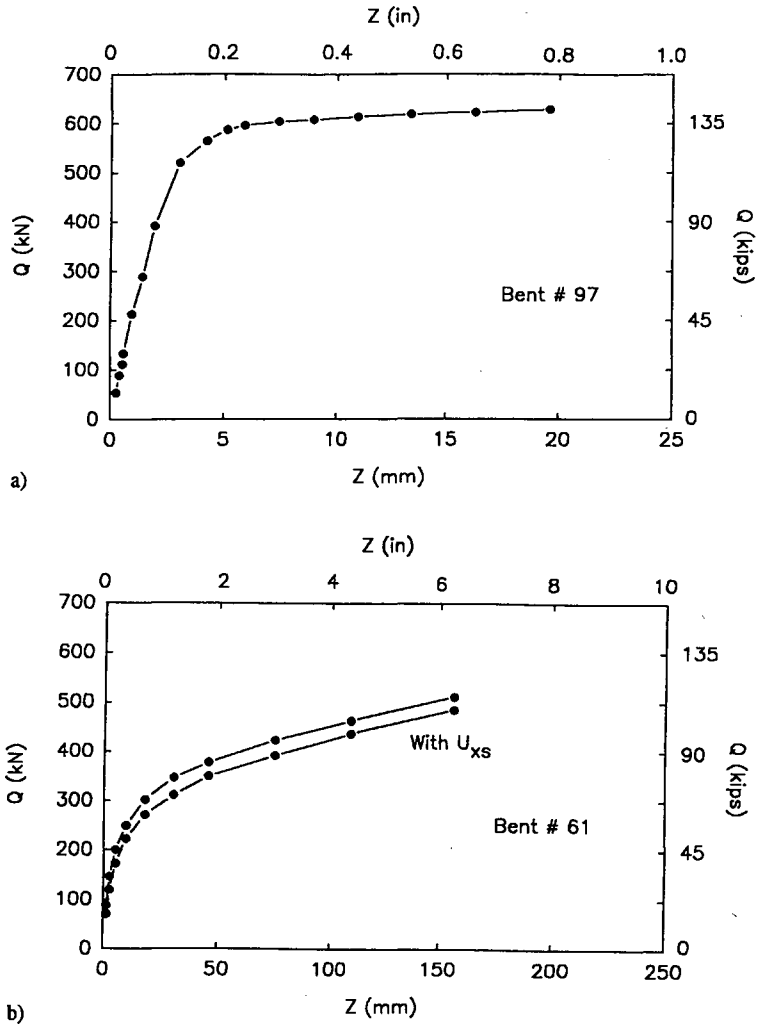

FIGURE 3 Backbone load-settlement curves for piles of (*a*) Bent 97 (long friction piles in Bay mud) and (*b*) Bent 61 (short end bearing piles in Merritt sand).

from the curves of Figure 4 based on the formulation given by Norris (*1*). (Again, note that no free-field cutoff is shown.) These are the center groups of the layout shown in Figure 6 from the paper by Abcarius (*11*). Even though the group at Bent 97 has one more pile, this extra pile falls on the stabilized axis of rotation and would offer little moment resistance. However, it should be pointed out that a shear key was used at the base of the column connection to the foundations, thereby affecting such moment transfer. Therefore, for purposes of comparison, one should really compare the transverse moment resistance of the whole bent in such soils (Bent 61 versus Bent 97), that is, the vertical stiffnesses of the piles of a group multiplied by their vertical pile head displacement multiplied by the distance between pile groups on opposite sides of the bent. (See Figure 1 of the preceding paper.) Of course, in a structural dynamic model, lateral and vertical stiffnesses rather than lateral and rotational stiffnesses would be supplied for each foundation.

Regardless of which it is that one compares—the vertical stiffness of the individual pile, the rotational stiffness of the group, or the rotational stiffness of the bent as a whole—it is clear from Figures 4 and 5 that the long friction piles in Bay mud are stiffer (for the same deflection and rotation) than the short end bearing piles in the Merritt sand.

LATERAL STIFFNESS

The lateral stiffness of a pile group derives from the lateral stiffness of the average pile in the group multiplied by the number of piles, to which one adds the lateral stiffness of the pile cap.

Although no group interference effect is employed relative to the vertical-rotational response of the piles, such an effect needs to be considered relative to laterally loaded pile response. As can be judged from Figure 1b, there is considerable overlap in the developing passive wedges of neighboring piles under lateral load as compared with no overlap of cylindrical zones of soil under vertical-rotational excitation. In addition, although rotational response is assessed for an

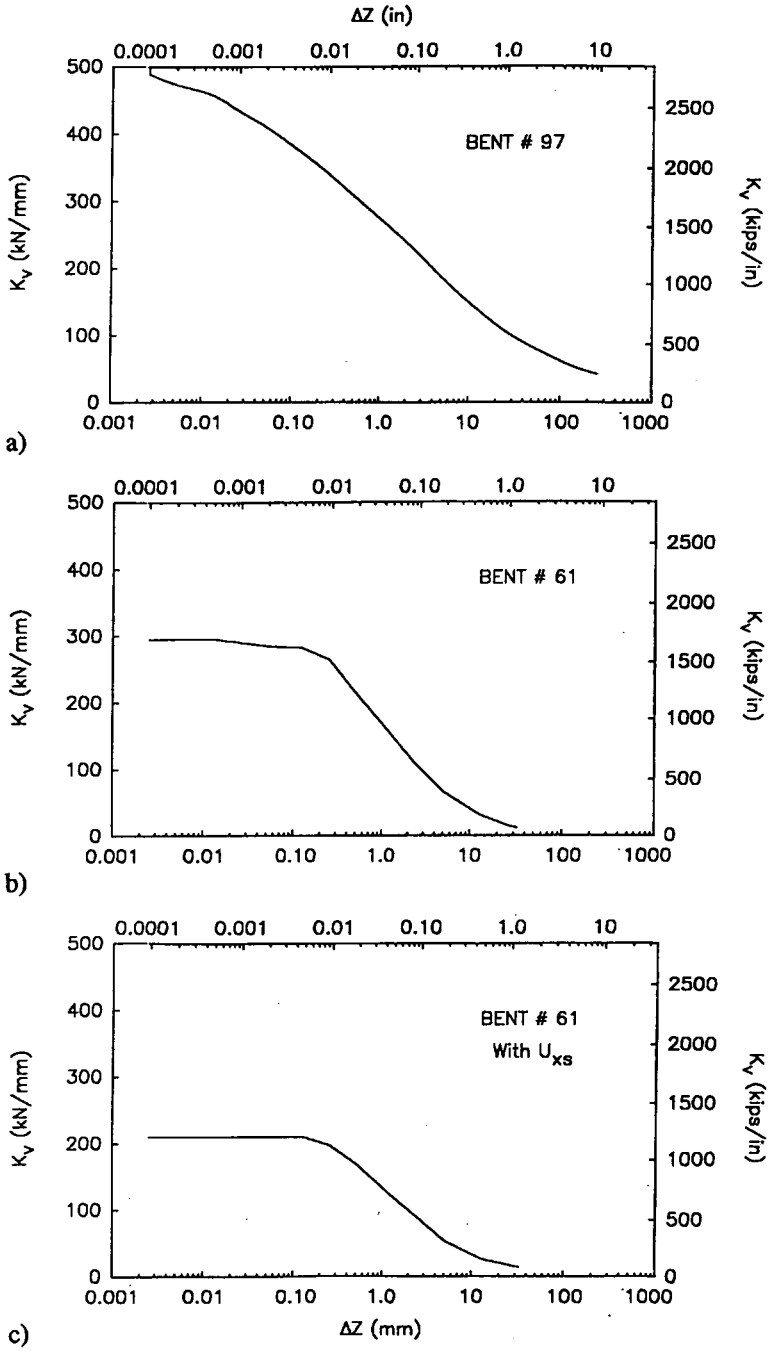

FIGURE 4 Nonlinear variation in the stabilized vertical pile stiffness (*a*) at Bent 97, (*b*) for no porewater pressure buildup (or at the start of strong shaking) at Bent 61, and (*c*) for porewater pressure buildup at the end of strong shaking at Bent 61. (Note that no free-field cutoff is shown.)

implied free (i.e., pinned) head condition, the lateral stiffness will vary depending on the appropriate head fixity condition. Therefore, a number of issues (pile cap contribution, group effect, and head fixity) are part of the lateral stiffness evaluation that are not part of the vertical-rotational stiffness evaluation.

The authors have calculated the lateral response of the individual pile on the basis of the so-called strain wedge model (*12,13*), which relates (*a*) the lateral strain (ε) in the developing passive wedge in front of the pile to the resulting pile deflection pattern (y versus x or deflection δ), (*b*) the horizontal stress change ($\Delta\sigma_h$) to the beam-on-elastic-foundation (BEF) soil-pile reaction (p), and (*c*) the Young's modulus of the soil ($E = \Delta\sigma_h/\varepsilon$) to the BEF subgrade modulus ($E_s = p/y$). Thus, the strain wedge model is a means for relating the one-dimensional BEF model parameters to the (envi-

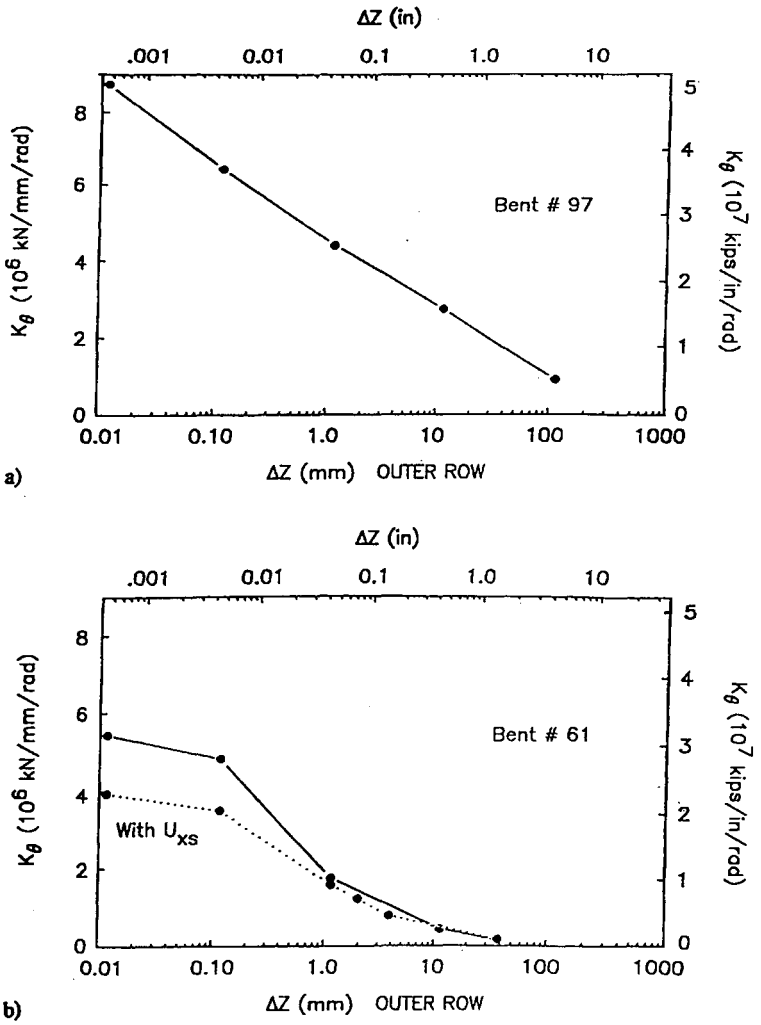

FIGURE 5 Nonlinear variation in the stabilized rotational stiffness of (*a*) 11-pile group at Bent 97 and (*b*) 10-pile group at Bent 61. (No free-field cutoff is shown on either curve.)

sioned) three-dimensional soil-pile response. These relationships ($\delta = \chi\varepsilon$, $E_s = NE$, and $P/B = A\Delta\sigma_h$, where χ, N, and A are the correlation parameters and B is the pile diameter) are shown schematically in Figure 7 at two levels of soil strain (ε) and therefore at two different pile head loads.

An interesting feature of such an approach is that the BEF *p-y* curves can be derived theoretically and have been shown to be in reasonable agreement (for common 1- and 2-ft diameter piles) with the empirical curves that are a part of such programs as COM624 (*14*). However, strain wedge model formulation clearly shows that such *p-y* curves are a function of pile properties as well as soil properties. The pile properties that affect the *p-y* curves are pile size, its bending stiffness *EI*, and the pile head fixity condition. It should be pointed out that the *p-y* curves are merely a by-product of the approach that solves for the Young's modulus profile of the soil for the specified value of horizontal strain. Knowing the pile and soil properties, the BEF subgrade modulus profile is obtained and traditional BEF analysis is invoked. In other words, an equivalent linear subgrade modulus profile results for the horizontal strain assumed.

In three dimensions, it is assumed that the developing passive wedge opens up at a fan angle ϕ_m equal to the mobilized effective stress friction angle of the soil. This is shown in Figure 8. With increasing lateral load, the base of the developing wedge moves down, as does the depth of the first zero crossing of the pile (i.e., the first depth where lateral deflection *y* equals zero). As the wedge moves down, it also opens up as strain and stress change and the mobilized friction angle increases. Given this approach, it is easily understood that a stiff pile (high *EI*) will have a different zero crossing than a flexible pile under the same lateral pile head load and therefore will invoke a different depth of soil to provide the needed (mobilized) lateral passive pressure resistance (or horizontal stress change) required for equilibrium. This horizontal stress change (equivalent to the deviator stress in a triaxial test at a confining pressure equal to the effective overburden pressure, $\sigma_{v'o}$) multiplied by the width of the front of the wedge at that depth is the corresponding BEF line load force *p* at that depth. (In clay, the geometry of the wedge is a function of the mobilized effective stress friction angle, but the stress change and strain are the deviator stress and axial strain from

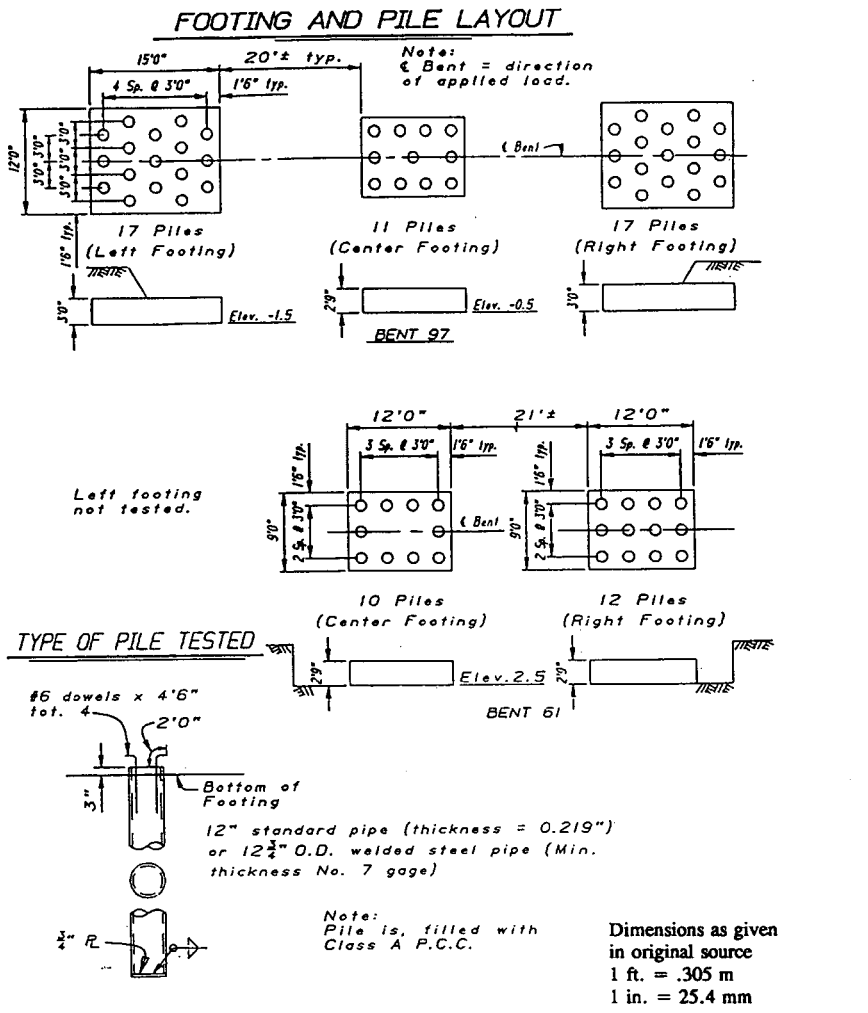

FIGURE 6 Layout of Caltrans pile group load tests [from Abcarius (*11*)]. Groups compared in Figure 5 are the center groups.

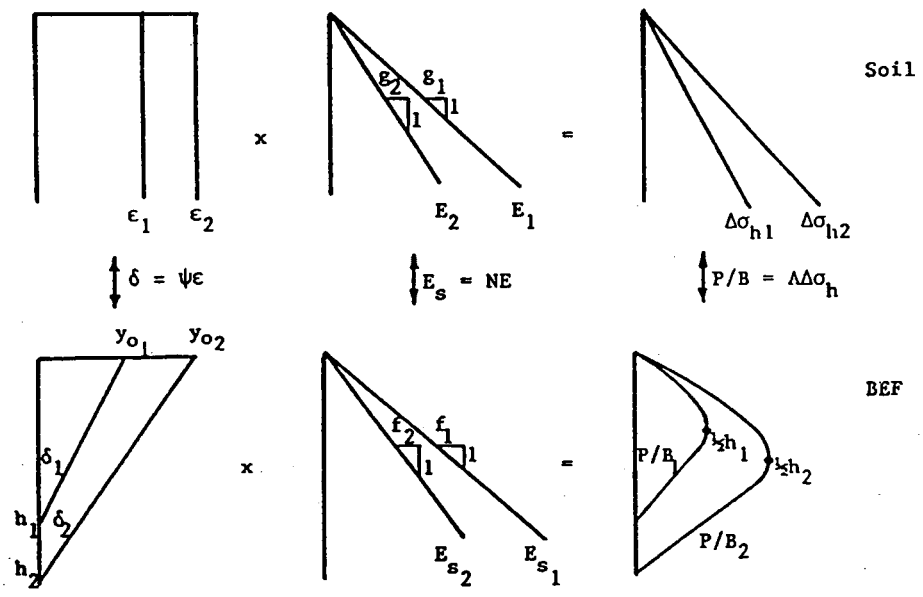

FIGURE 7 Relationship between beam-on-elastic-foundation (BEF) and soil parameters.

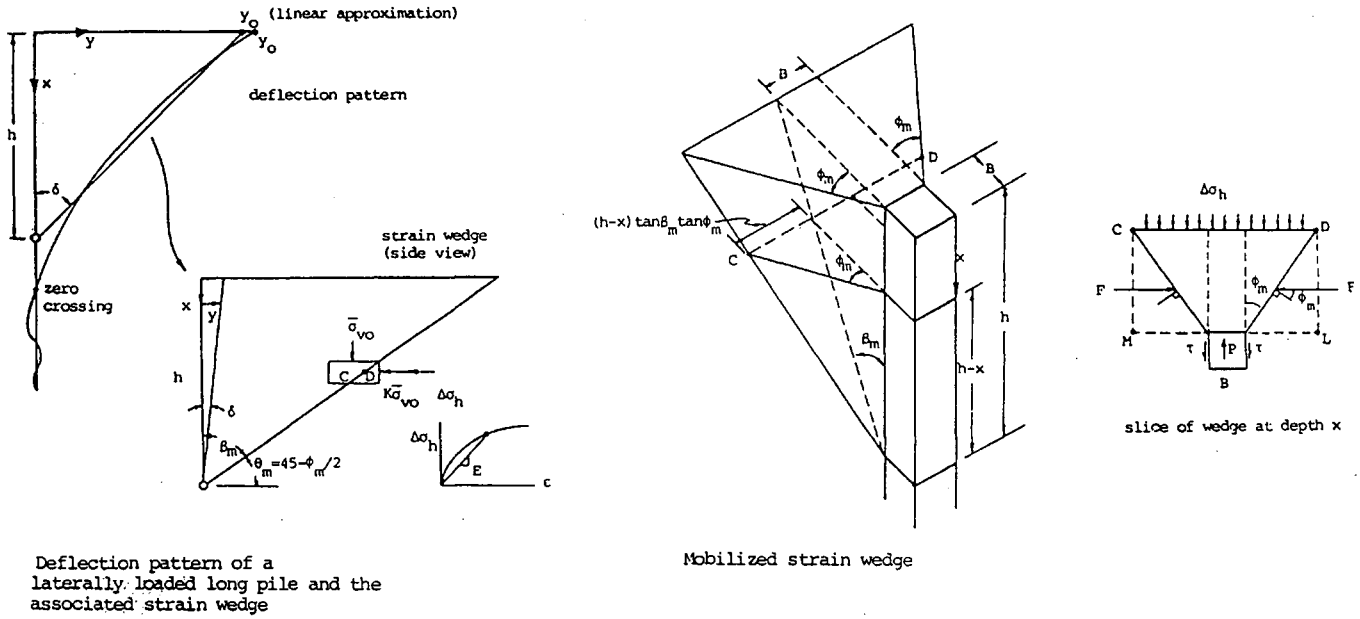

FIGURE 8 Strain wedge model.

a consolidated undrained triaxial test.) Therefore p (as well as deflection y and thereby $E_s = p/y$) at any depth x will be a function of the pile bending stiffness EI (and the pile head fixity condition). Likewise, the p-y curve at a given depth will vary depending upon the soil immediately above and below that in question.

The features that make the strain wedge model particularly useful in the present application are these: (*a*) one knows the value of relative strain in the near-field soil region (i.e., within the wedge) and (*b*) the fact that one determines the equivalent linear subgrade modulus (E_s) profile means that it is a simple matter to reduce it to account for pile group interference effects. [To do the latter, the reduction factor R, given as a function of the center-to-center spacing of the piles, from NAVFAC DM-7.2 (*6*) is employed.] The fact that one knows the value of the (relative) strain allows for a comparison with the level of free-field strain and therefore the establishment of a free-field cutoff. Neither of these features is readily available in programs such as COM624 (*14*). One last feature is that the model is good over the full range in soil strain, from 1×10^{-4} percent up to and beyond soil failure.

Figure 9 shows a comparison of the lateral load response for the same pile groups considered earlier (Figure 6) assessed from lateral pile group load tests conducted by Caltrans at Bents 61 and 97. The details of the tests and the results obtained for the opposing groups (from jacking apart pairs of groups) at these bents are given by Abcarius (*11*). Such tests are unique in that they were carried to structural failure of

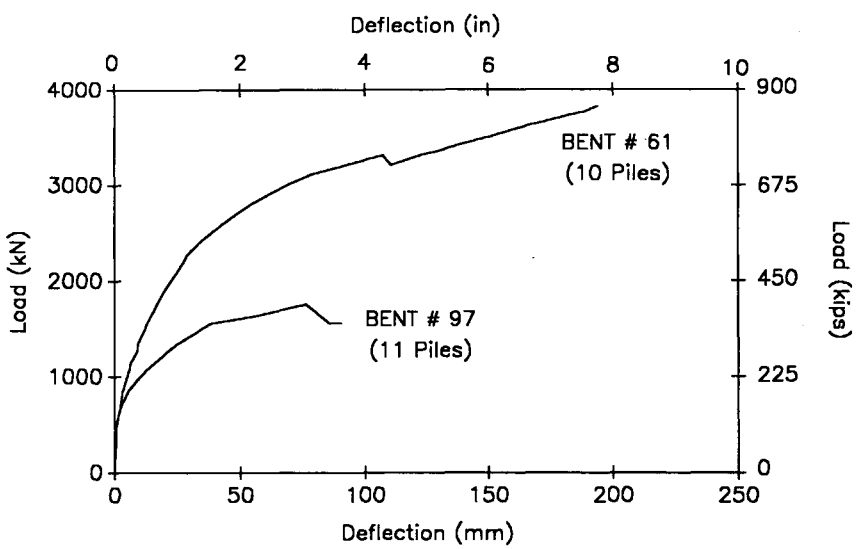

FIGURE 9 Lateral load versus deflection response of 10- and 11-pile groups at Bents 61 and 97 from Caltrans tests.

the piles or cap at very high lateral deflections. It is interesting that the lateral resistance of the pile group in Merritt sand is much greater than that of the pile group in the Bay mud (even with one more pile in the latter group). Recall that the opposite was true relative to the vertical-rotational resistance; that is, the long friction pile group in Bay mud was stiffer in vertical-rotational resistance than the short end bearing group in the Merritt sand. The reason for this reversal is that the soil providing the resistance to the lateral load is different from that offering resistance to the vertical load, as shown schematically in Figure 1b.

Although the load-deflection curves of Figure 9 may be used to construct the variation in lateral stiffness K_{lat} (load divided by deflection) of the group, it is important to see if the same response can be assessed. Accordingly, a strain wedge model program was used to develop the load-versus-deflection response for two pile head fixity conditions, a free (pinned) head condition and a fully fixed condition (deflection with zero rotation at pile top). However, the program STIFF1 (*15*) was used to establish the reduced bending stiffness *EI* that would result from cracking at higher lateral loads, and hence moments, in the pile. From such results, it was determined that the ultimate moment in the pile at pile top would be 470 kN-m (347 kip-ft), whereas at a depth below the upper level of reinforcing steel (see Figure 6) it would be 247 kN-m (182 kip-ft). For the free head pile where the moment is a maximum at the lower level, the bending stiffness *EI* was taken to vary with the value of maximum moment at this lower level M_l. Once a plastic hinge formed (the maximum moment equaled the ultimate moment of 247 kN-m [182 kip-ft] at the lower level), the depth of the developing strain wedge was taken to remain fixed as the soil in the wedge built up to failure. The free head response curves for the two pile groups are shown in Figure 10. Values of *EI* for the corresponding lower-level moments are noted on these curves.

By contrast, the *EI* for the fixed head response was taken to vary with the maximum moment at pile top M_t. However, letting *EI* decrease with the increase in pile head load, and hence maximum moment, eventually led to development of a plastic hinge at pile top. Thereafter, the so-called fixed head condition was solved assuming a constant moment at the pile head [470 kN-m (47 kip-ft)]. Interest then shifted to the maximum moment at the lower level M_l and the eventual development of a second hinge at this location. During this time, the *EI* was taken on the basis of the moment at the lower level. The fixed head curves for such an analysis are also shown in Figure 10.

One can consider each point on the calculated curve or curves at the higher level of load as one point from a line reflecting a load-deflection curve for a pile with a constant

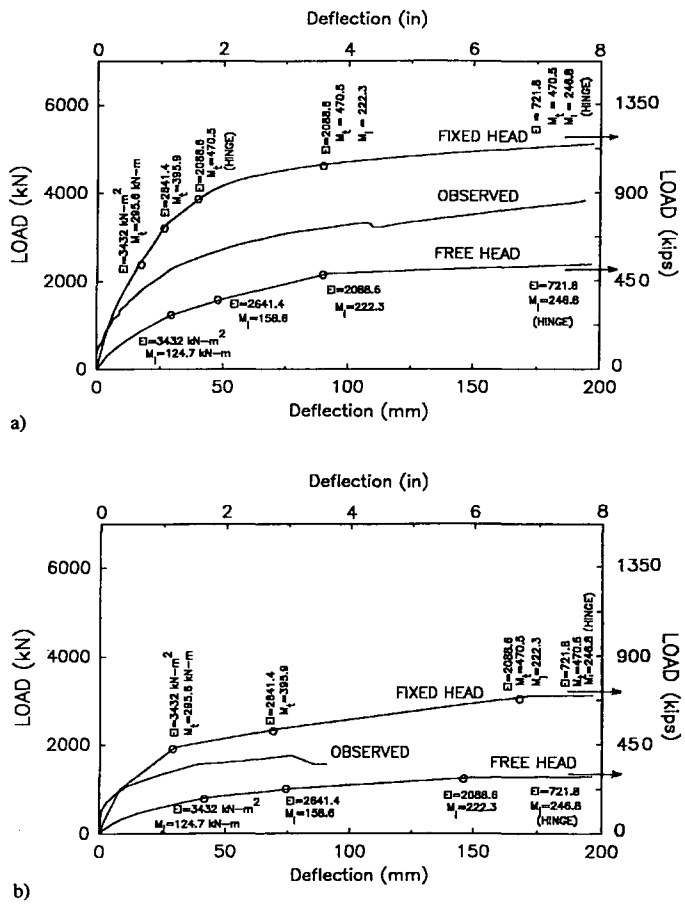

FIGURE 10 Predicted versus observed response of (*a*) 10-member pile group at Bent 61 and (*b*) 11-member pile group at Bent 97.

EI passing through that curve and only that (compatible) point used to establish the final curve. Of course, at lower levels of load a constant *EI* was used.

The observed responses from Figure 9 are plotted in Figure 10 for comparison. It is interesting to note that at low loads the recorded response is stiffer than, but generally follows, the computed fixed head response and then starts to deviate as if the piles were unable to maintain more than a limited pile head moment. The levels of pile head moment at which the observed response deviates from the computed fixed head response are 134 and 138 kN-m (99 and 102 kip-ft) for the pile groups at Bents 61 and 97, respectively. This then represents the yielding of the pile-to-cap connection rather than the failure of the piles. Not shown are the predicted responses in which the pile head moments are limited to these values, curves that virtually overlie their respective observed response.

It should be pointed out that the predicted responses were assessed on the basis of different pile group interference effects. Although the spacing of the piles in the group is not constant (because of missing piles in the arrangement), a weighted value was assessed and an *R*-value chosen accordingly. The *R*-values employed were 0.55 for the 10-pile group of Bent 61 and 0.335 for the 11-pile group of Bent 97.

Although the strain wedge model response was calculated for the large loads to which the tests were carried, it was also used to assess response at very small deflections. At such a level of response, it is clear from Figure 10 that a fixed head condition should be assumed. Likewise, given the growth in both the depth and the breadth of the pile's strain wedge with increasing load (as can be imagined from reference to Figure 8), it is likely that the *R*-value should be higher (for less interference between neighboring wedges) at lower load levels. (However, such additional correction was not attempted here.) Figure 11 shows the variation in the calculated fixed head pile group stiffnesses over the small deflection range. Of course, the free-field cutoff (see Figure 2) has not been superimposed on these plots. However, if one were to employ the free-field strain values for the dense sand and Bay mud at the Oakland Outer Harbor (which are not necessarily the correct values to use at the Cypress Street viaduct because the values at the Oakland Outer Harbor correspond to a common ground surface acceleration), the solid point appearing on each curve would mark the level at which the horizontal line would occur. Note the significant difference in deflections associated with these points.

The reader will note that the soil surrounding the pile caps of the center test groups was removed, and therefore no cap resistance was added in the strain wedge model analysis. By contrast, during the Loma Prieta earthquake, there would have been this additional resistance as well as 0.6 to 0.9 m (2

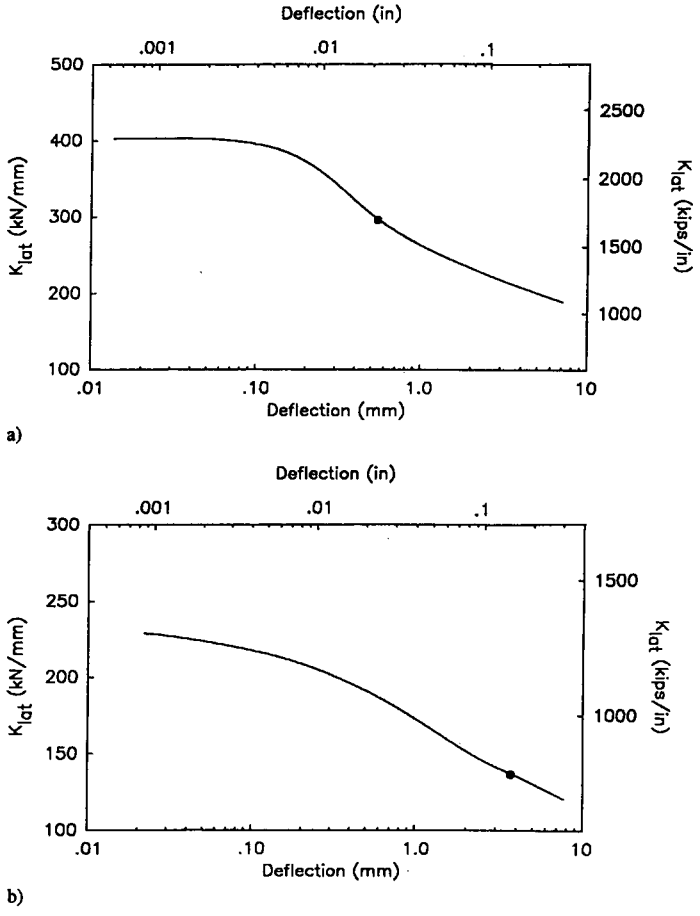

FIGURE 11 Computed lateral stiffness variations in the small deflection range for (*a*) 10-member pile group at Bent 61 and (*b*) 11-member pile group at Bent 97.

to 3 ft) more overburden as compared with that shown in Figures 9 and 10 of the preceding paper.

DISCUSSION OF RESULTS

In this paper, the Cypress Street viaduct failure has been used as a vehicle to highlight present capabilities and shortcomings relative to the evaluation of seismic pile foundation stiffness. A significant point that the authors have tried to make is the need for highway departments to carry through on such "geotechnical" analysis. It is important that in undertaking structural dynamic modeling of a highway bridge, deflection- and rotation-compatible foundation stiffnesses be used in order to assess the motion of the structure appropriately, obtain the correct distribution of seismic loads to the structure, and evaluate foundation (pile head) forces appropriately. It has been shown in parallel soil-foundation-structure analysis relative to the nearby Oakland Outer Harbor Wharf that employing unrealistic stiffnesses can lead to serious errors in the structure's computed motions and the computed foundation forces. This is extremely important with regard to future investments in the seismic retrofit of the nation's bridges.

ACKNOWLEDGMENT

The funding for this study was provided by the U.S. Department of Energy as part of a larger study on pile foundation stiffnesses for the seismic modeling of railroad and highway bridges. Such support is gratefully acknowledged.

REFERENCES

1. Norris, G. M. Overview of Evaluation of Pile Foundation Stiffnesses for Seismic Analysis of Highway Bridges. In *Transportation Research Record 1336*, TRB, National Research Council, Washington, D.C., 1992, pp. 31–42.
2. Norris, G., R. Siddharthan, Z. Zafir, S. Abdel-Ghaffar, and P. Gowda. *Soil-Foundation-Structure Behavior at the Oakland Outer Harbor Wharf.* Report CCEER-91-2. Center for Civil Engineering Earthquake Research, University of Nevada, Reno, 1991.
3. Lam, I. (Po), and G. R. Martin. *Seismic Design of Highway Bridge Foundations.* Reports FHWA/RD-86/101, FHWA/RD-86/102, and FHWA/RD-86/103. FHWA, U.S. Department of Transportation, 1986.
4. *ATC 3-06 Tentative Provisions for the Development of Seismic Regulations for Buildings.* Applied Technology Council, 1978.
5. Schnabel, P. B., J. Lysmer, and H. B. Seed. *SHAKE: A Computer Program for Earthquake Response Analysis of Horizontally Layered Sites.* Report EERC 72-12. Earthquake Engineering Research Center, University of California, Berkeley, 1972.
6. *Design Manual: Foundations and Earth Structures.* NAVFAC DM-7.2. U.S. Government Printing Office, Washington, D.C., 1982, pp. 196 and 241.
7. Norris, G. M. Evaluation of the Nonlinear Stabilized Rotational Stiffness of Pile Groups. In *Proceedings of the 37th Highway Geology Symposium*, Helena, Montana, 1986, pp. 331–386.
8. Vanikar, S. N. *Manual on Design and Construction of Driven Pile Foundations.* Report DP-66-1. FHWA, U.S. Department of Transportation, 1985.
9. *Design Manual: Soil Mechanics.* NAVFAC DM-7.1. U.S. Government Printing Office, Washington, D.C., 1982, p. 149.
10. Norris, G. M., R. Siddharthan, Z. Zafir, and P. Gowda. *Seismic Lateral and Rotational Pile Foundation Stiffnesses at Cypress.* Report CCEER-91-3. Center for Civil Engineering Earthquake Research, University of Nevada, Reno, 1991.
11. Abcarius, J. L. Lateral Load Test on Driven Pile Footings. In *Transportation Research Record 1290*, TRB, National Research Council, Washington, D.C., 1991, Vol. 2, pp. 139–143.
12. Norris, G., and P. Abdollaholiaee. BEF Studies with the Strain Wedge Model. In *Proceedings, 26th Symposium in Engineering Geology and Geotechnical Engineering*, Paper 13, 1990.
13. Norris, G. M., and P. K. Gowda. *Laterally Loaded Pile Analysis for Layered Soil Based on the Strain Wedge Model.* Report 91-3. Center for Civil Engineering Earthquake Research, University of Nevada, Reno, 1991.
14. Reese, L. C., and W. R. Sullivan. *Documentation of the Program COM624.* Geotechnical Engineering Center, Bureau of Engineering Research, University of Texas, Austin, 1980.
15. Wang, S. T., and L. C. Reese. *Documentation of the Program STIFF1: Computation of Nonlinear Stiffnesses and Ultimate Bending Moment of Reinforced-Concrete and Pipe Sections.* Ensoft, Inc., Austin, Texas, 1987.

Publication of this paper sponsored by Committee on Foundations of Bridges and Other Structures.